Relative relocation of earthquakes along the northern North Atlantic Ridge using Rayleigh waves

Christian Grude Kolstad

Master Thesis in Geosciences
Discipline: Geophysics
60 credits

Department of Geosciences
Faculty of Mathematics and Natural Sciences
University of Oslo

June, 2017

Printed: Reprosentralen, University of Oslo.

Abstract

Earthquake activity around the world is associated with tectonic processes that occur from the movement of the lithospheric plates. At many oceanic plate boundaries location of earthquakes is routinely done using data from seismic stations far from the epicenters. The lack of nearby stations limits precise location and accurate description of earthquakes that can contribute greatly to further understand the fundamental physics of tectonic processes as well as mapping Earth's deformation. Surface waves and in particular Rayleigh waves, are usually a major and well-recorded seismic phase for mid-oceanic ridge earthquakes. They can therefore be used to improve the location of the earthquakes. From earthquake-pairs, Rayleigh wave time shifts are measured by cross-correlation of waveforms and then applied to a double-difference based inversion method, effectively giving relative epicentroids that are shown to improve earthquake locations. Relative origin time shifts are also estimated. In total 153 shallow and moderate-sized earthquakes are relocated around the North Atlantic Mid-Oceanic Ridge from Iceland to Svalbard. This region has been divided into three parts; Kolbeinsey Ridge along with Jan Mayen Fracture Zone, Mohns Ridge and lastly Knipovich Ridge together with Spitsbergen Fracture Zone. The North Atlantic Mid-Oceanic Ridge is a system of tectonically active fracture zones, ridge-segments and well as minor compressional zones that generate strike-slip earthquakes, normal fault earthquakes and some obliquely thrust fault earthquakes. At Kolbeinsey Ridge and Jan Mayen Fracture Zone the mean distance shift is calculated to about 8 km. At Mohns Ridge the events are relocated with a mean of about 11 km. Around Knipovich Ridge the result show a mean of approximately 5 km whereas events at Spitsbergen Fracture Zone result in a mean of about 7 km. It is found that the relocated earthquakes produce more tectonically consistent locations, particularly at Kolbeinsey Ridge, Jan Mayen Fracture Zone and Mohns Ridge. This is done without any consideration to tectonic structures in the region but rather by defining relevant parameters such as requesting a minimum number/azimuthal coverage of observations with each event-pair, a maximum distance between events and also a minimum cross-correlation value. As such Rayleigh waves have the potential to solidly constrain event locations assuming a continuous clustering of earthquakes is present.

Acknowledgement

First I would like to give many thanks to my supervisor Prof. Valerie Maupin at the Department of Geoscience, UiO for support and guidance throughout this master thesis. It was with her invaluable help and understanding of my position that made this work possible. I also want to thank my co-supervisor Dr. Tormod Kværna at NORSAR for pushing me as well as introducing me to Michael K. Cleveland & Charles J. Ammon who have provided the surface wave relocation method.

This leads me to giving a special thanks to Michael Cleveland who have with almost countless emails-exchanges answered any questions I have had during my work. There is no doubt that his knowledge in the field of double-difference relocation greatly improved this thesis.

I want to express gratitude to Anne Claire Fouilloux for giving of her time and expertise with programming issues, in particular for the *Generic Mapping Tool*. Also deserving of appreciation is Grace Elizabeth Shephard at CEED who took time of her busy schedule to show me the the many possibilities of GMT. The plots would not be so visual pleasing had it not been for her detailed solutions.
Lastly I would like to thank other teachers and administration staffs at the Department of Geoscience who have always kindly assisted in making my work at UiO achievable.

June, 2017

List of Figures

List of Tables

Contents

Chapter 1

Introduction

1.1 Earthquakes

According to Shearer [40] there are roughly 50 earthquakes around the world that can be felt by humans every day, and every other day there is an earthquake that is large enough it can damage structures. Seismic waves traveling through the interior and at the surface of the earth are today registered with digital instruments that are placed all around the globe. Studying earthquakes, both their location and size have been done through routine processing over 100 years now [3]. This have lead to indispensable contributions for understanding global as well as regional tectonic processes. The point of origin of an earthquake are commonly termed the *focus* or *hypocenter* which can be determined by using the arrival time of the seismic waves. However, when large earthquakes are presented in the news, often the origin or location is given in terms of the *epicenter*, being the point on the earths surface straight vertical from the hypocenter. There are several types of earthquake magnitude scales where the "Richter scale" is considered as the most famous. A second magnitude scale, the *body wave magnitude*, is defined as $m_b = log(A/T) + Q(h, \Delta)$, where Q here represents an empirical function. Stein & Wysession [42] points out that both equations are empirical, not related to the physics of earthquakes and for large earthquakes the effect of *magnitude saturation* also plays in, not being able to differentiate earthquakes with different energy.
A solution is found with *moment magnitude* M_w, based upon the scalar *seismic moment* M_0 being defined as $M_0 = \mu \overline{D} A$ [40, 42]. The moment magnitude can be expressed as

$$M_w = \frac{log M_0}{1.5} - 10.73. \tag{1.1}$$

To determine M_w is not as directly available as m_b, but thanks to *The Global CMT Project* [6, 17], it is now possible to compute and plot earthquakes with moment magnitude easily. An example plot in the area around Iceland and Svalbard can be seen in figure 1.1. This also shows the focal mechanisms described in section 2.3.

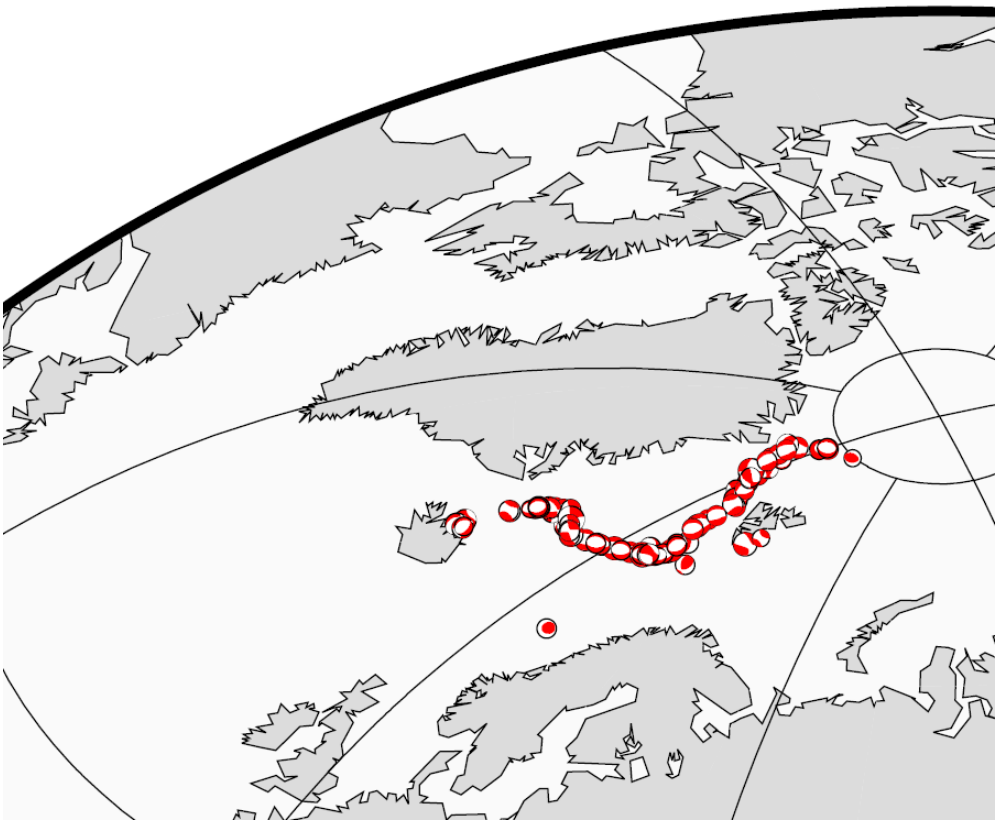

Figure 1.1: Plot of a GCMT catalog search roughly from Iceland to Svalbard starting from the year 2000 and going until the start of 2017. The search is made with moment magnitude limited to between 5.0 and 7.0, no depth limit, tension plunge from 0-90 degrees and null axis plunge from 0-90 degrees.

In total there are 103 earthquakes plotted with focal mechanisms starting from $66°N$ and stopping at $85°N$. There are some outliers but in general the earthquake seismicity are much related to the plate boundaries. Majority of the earthquakes here are defined with a depth of 10.0 km, though the shallowest are registered at 6.0 km down and the deepest at 23.6 km. All are registered with either a m_b scale or M_w scale, likewise as the earthquake data collected (see appendices).

1.2 Purpose of study

This master thesis is a cooperation between the University of Oslo and NORSAR (Norwegian Seismic Array). Precise location of earthquakes in oceanic areas are not done readily due to the sparsity of seismic stations surrounding. This can be improved by using a method that takes advantage of the time shift between Rayleigh waves from neighboring earthquakes, if certain assumptions and requirements are met. In the work done by Cleveland & Ammon [14], the relocation method has given satisfying results where they focused on the Panama Fracture Zone. Their findings and expertise in the field are used as a support for this thesis. In particular they have provided the python modules or scripts named *pySACio_2.py* and *surfaceWaveRelocation_v2.6.py* as well as theoretical and practical insight necessary for going through with the study. The goal is to apply their method to earthquakes along the North-Atlantic Mid-Oceanic Ridge between Iceland and Svalbard, with measurements from stations from different parts of the world.

1.3 Tectonic overview and Outline of thesis

At the present day the Northern Mid-Atlantic Ridge is a tectonically complex region with plate boundaries of different types and directional pattern. Since the late Triassic the spreading rate and drift

direction between the Eurasian and North American plates have varied. Before roughly 53 m.y. in early Eocene the spreading rate changed between 5.0 cm/year and 4.0 cm/year and since after that has slowed down [31,37]. It is considered to cover the region from about $60°N$ to $85°N$. It is made up of structures like ridges, transform faults and small compressional zones. The Northern Mid-Atlantic Ridge from Reykjanes Ridge goes through Iceland, continues with the Kolbeinsey Ridge further north where it is abruptly shifted by Jan Mayen Fracture Zone (WJMFZ in figure 1.2). It is then going on with Mohns Ridge in a northeastern direction before it curves slightly and advances as the Knipovich Ridge along Svalbard beyond the 80° latitude -line.

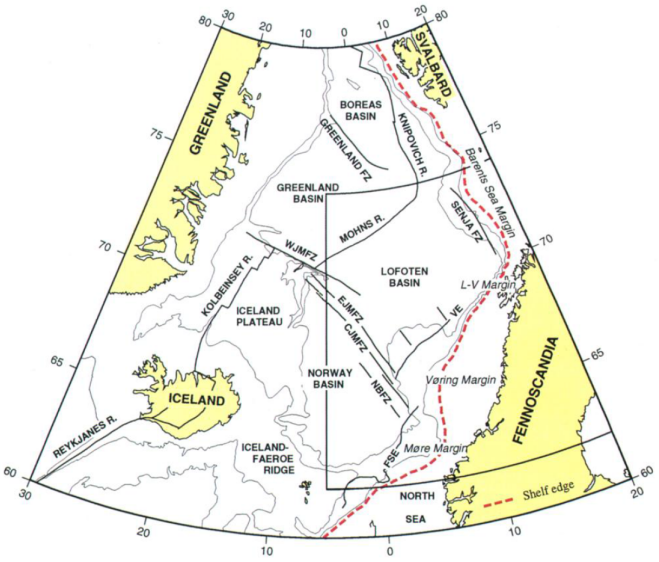

Figure 1.2: Overview of the North Atlantic Mid-Oceanic Ridge just south of Iceland with Reykjanes Ridge and up to Svalbard. Reprinted from Byrkjeland et. al. [9].

In the area of Jan Mayen, seismicity with tectonic activity in addition to volcanic activity are occuring [41]. At the northern end of volcanic island Jan Mayen the Jan Mayen Fracture Zone is found, offsetting the Mid-Oceanic Ridge. The fracture zone divides Kolbeinsey Ridge to the south and Mohns Ridge just north of Jan Mayen, currently with spreading rates of approximately 15-17 mm/year. Even though Kolbeinsey Ridge displayed a rather linear ridge -structure in earlier geological times, it has now been cut off by three non-transform segments [47]. It has also been argued for the possibility of viewing the Jan Mayen island as part of a microcontinent developed by the plate tectonic system. As Sørensen et. al. [41] further mentions, the high amount of seismicity with different magnitudes larger than 3.0 show a general scattered pattern of events contributed partly to difficulties of precisely and accurately locating the events. The highest activity does yet seem to occur in center of the fracture zone with decreasing events southwest and just north of the island (figure 1.3). They go on to assess studies that determines the Jan Mayen Fracture Zone as a left lateral transform fault in a northwest to southeastern direction and that extension into Mohns Ridge have structures of normal faulting. Jan Mayen Fracture Zone can be separated into more detailed segments, but Havskov & Atakan [22] found that strike-slip faults associated with the structural trends of oceanic transform faults are dominating this area for larger earthquakes. Simultaneously there is a gradual change when progressing north of the fracture zone. Earthquakes displaying more dip-slip mechanisms of normal fault orientation are associated with the North American and Eurasian divergent plate boundaries [22].
With a direction orthogonal to the spreading direction, Mohns Ridge was developed as the Norwegian-Greenland sea opened up, now over 500 km from the Jan Mayen Fracture Zone to the south and Knipovich Ridge to the north [16]. The width of the valley continuing from the ridge are not too distinguished by varying from 8-15 km and having different bathymetry images from the northwest side to the southeast side. A current spreading rate of 1.8 cm/year has developed from fluctuating spreading rates at the latest geological periods. As Dauteuil & Brun [16] discuss, the spreading direction does significantly change to produce complex fault patterns. Even though faults for the most part are perpendicular to the spreading direction and thus giving normal faulting, structures also indicate deformation with strike-slip displacements.

The Knipovich Ridge, continuing on from Mohns Ridge, was developed as the Northern Mid-Atlantic Ridge around 20 m.y. ago advanced north to the Spitsbergen Fracture Zone [31]. As Mohns Ridge, Knipovich Ridge have an oblique spreading direction adjusted from the plate boundary and also appears with different spreading rates at the western end around 7 mm/year and the eastern side around 1 mm/year as presented by Kandilarov et. al. [31]. This makes Knipovich Ridge notably slower compared with Jan Mayen Fracture Zone and Mohns Ridge. As Engen et. al. [19] mentions, there are no large transform zones that offset Knipovich Ridge in any considerable way. Spitsbergen Transform System progress from Knipovich Ridge, residing a pattern of short ridge-segments and transform faults [19]. It involves the region to about 85° and is divided into four structural segments. Interesting for this thesis are Molloy Ridge, Molloy Fracture Zone and Spitsbergen Fracture Zone. The seismicity of Molloy Fracture Zone (along with the northern part of Knipovich Ridge) are made up of mainly strike-slip faulting in addition to normal faulting motion. Molloy Ridge, being roughly 70 km long with more oblique components of normal fault structures, leads into Spitsbergen Fracture Zone that resides transform faults [19]. Reasoning that Molloy Fracture Zone and Spitsbergen Fracture Zones are regional comparable as well as for simplicity, the whole structural area after Knipovich Ridge is bundled together as Spitsbergen Fracture Zone.

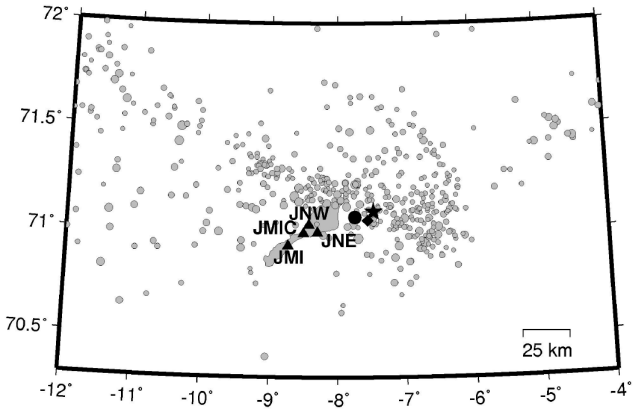

Figure 1.3: Map over seismicity around Jan Mayen with events greater than 3.0 magnitude between 1972 - 2003. Reprinted from Sørensen et. al. [41].

Overall, the part of the Northern Mid-Atlantic Ridge region described hosts steadily moderate-to-large earthquakes caused by faulting zones and tectonically active ridge segments that make up the plate boundaries (figure 1.4).

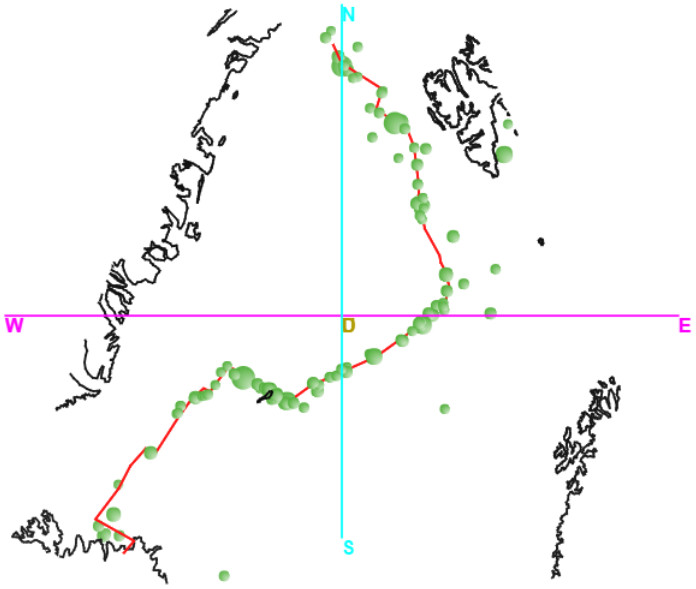

Figure 1.4: Earthquake activity (represented by circles) between Iceland and Svalbard from 1990 to today with search options specified to magnitude range from 5.0 - 8.0 and depth range of 0 - 30 km. In total there are 119 earthquakes selected in this box. Created with IRIS Earthquake Browser.

The land areas in figure 1.4 to the west is Greenland with Iceland further south and part of Svalbard in the northeastern direction. Visible are also the earthquakes that seem to be very much clustered along especially Jan Mayen Fracture Zone, Mohns Ride and Knipovich Ridge. Fewer earthquakes are along Kolbeinsey Ridge, particularly closer to Iceland. Some earthquakes appear to be offset from the ridge system, and rather located more in the interior of the North American and Eurasian plates.
The main objective of this master thesis is to use relative Rayleigh wave time shifts to precise and accurately estimate relative event locations along the northern North Atlantic Ridge. This can aid in a better understanding and knowledge of earthquake physics around mid-oceanic ridges and fracture zones, faulting processes as well as earthquake dependence on other earthquakes. There is also high relevance for earthquake locations and how it is related to spreading rates at the different segments of the ridge. Information and data of the earthquakes are gathered in its entirety from IRIS. To reach the objective simple seismic processing and a double-difference iterative inversion method are performed on time-series waveforms, solved respectively with *pySACio_2.py* and *surfaceWaveRelocation_v2.6.py*. Alike with Cleveland & Ammon [14], the focus lies on shallow moderate-to-large earthquakes much because they are registered well on stations and support easily surface waves. The datasets collectively combine to 179 earthquakes (some used more than one time) with magnitude range from 4.8 to 6.7. However, there is made no particular attempt to include only strike-slip earthquakes as Cleveland & Ammon have done. Though there are many earthquakes with smaller magnitude registered in the region between Iceland and Svalbard, the largest ones do not have a magnitude larger than 7.0. Additionally the depth for practically all earthquakes do not exceed 30 km, meaning this region is well suited and self-constrained in terms of the objective.
This study is motivated by a lack of seismic stations in the vicinity of earthquakes in the North Atlantic Ridge that makes it difficult to confidently determine earthquake locations with traditional methods. Instead the general large distances to stations are taken advantage of in an inversion method for Rayleigh waves. Chapter 2 reviews characteristics of earthquakes, seismic waves propagated due to faulting or earthquakes and lastly description of seismograms. Chapter 3 goes more into detail on the relocation method and how it is set up before Chapter 4 includes more the technical sides. The results and discussion for relocated earthquakes along the North Atlantic Ridge as well as comparison with other works are presented in Chapter 5 and Chapter 6 accordingly. The thesis ends with a conclusion and reflection on future work that can be looked into in Chapter 7.

Chapter 2

General theoretical background

2.1 Seismic waves

Seismology, by definition the study of elastic waves in the solid earth, can be said to be the principal method for earthquake studies. Earthquakes are examples of natural source origins. After generation seismic waves are propagating through a section of the earth before being recorded at a receiver. The relevant section of the earth is termed the medium which commonly have different properties, one being the speed at a particular area. Because signals from sources are registered on seismograms, this information can provide location origin as well as the geometry of the source. The arrival time of the signal is defined as the origin time of when the seismic waves are generated at the source plus the travel time from the source to the receiver. Though an approximation, plane waves can be a good solution viewed as a limit of spherical waves for seismic waves if the source is located at great distances from the receiver [2, 42]. In seismology, the fundamental equation is the *equation of motion* for describing seismic waves that are time-dependent and causing an acceleration of material in the medium. For an elastic continuous medium, the equation of motion can be expressed [40] as

$$\rho \frac{\partial^2 u_i}{\partial t^2} = \partial_j \tau_{ij} + f_i, \tag{2.1}$$

where the first term, ρ, represent the density. The two terms u_i and f_i are component i of displacement and force, respectively. Also, τ_{ij} notes the stress in the *constitutive equation* generally defined as $\tau_{ij} = c_{ijkl} e_{kl}$ with summation notation. Whereas c_{ijkl} is defined as a constant named the elastic moduli and describes properties of a material, e_{kl} symbolize the strain tensor [42]. Solutions of the displacement u_i for models of the Earth are beneficial for predicting ground motion and therefore being able to producing synthetic seismograms [40]. Cleveland & Ammon [14] take advantage of synthetic seismograms to perform sensitivity tests to their methods. The expression for u_i is helpful to study because it gives information on how a seismic wave are generated, either it is a body wave or surface wave.

2.2 Spherical coordinates

Averaging the earth structure to be laterally homogeneous or in the next step be a homogeneous halfspace is justified when the area of study is small compared to the earth's radius. In many cases this holds weight, giving the opportunity to represent spherical wave fronts as approximated plane waves for when the source is far from the receiver. Another advantage is that by making these approximations, it serves as a starting point for more realistic and detailed models. To clarify, the general model of a laterally heterogeneous sphere can be approximated as a laterally homogeneous sphere or further in a stratified halfspace (ignoring the curvature of the earth) [42]. In relocating earthquakes at the northern North Atlantic Ridge this is an simplification that holds if the distances between earthquakes and stations are converted from curvatures to straight lines. Although a spheric model is not used in the relocation method, spherical coordinates are more intuitive to use in describing a system of earthquakes and stations compared with Cartesian coordinates. Treating the source (or epicenter) and the station as two points on the surface, the distance and the direction of the great circle arc they are connected to can be determined [42]. Specifically, the direction of seismic waves from the source is characterized by the *azimuth* angle ζ defined as the clockwise angle from the direction of north at the specific great circle arc. The distance in turn can be found by finding the angle Δ, measured between the station and epicenter from the origin of the spherical earth. Also, the use of spherical coordinates in seismology is often advocated because the earth can be approximated in many situations as spherical symmetric, for example having a velocity profile that vary much more with depth than lateral. Taking the perspective of the station, the *back-azimuth* angle ζ' is defined as starting from the local direction of north to the great circle arc in a clockwise setting. Since seismometers usually record the north-south and east-west components,

the radial and transversal components can be determined by making a coordinate transformation using the back-azimuth [42]. The reason for the extensive use of azimuth when describing a source and a receiver in earthquake studies is on account of earthquakes releasing more energy in some directions and less in others, consequently providing valuable information about the source.

2.3 Focal mechanisms

Accurately describing the complex geometry of a faulting zone is not an easy effort; in a realistic case the dimensions are finite and a fault is not a nice, straight plane. Yet geological observations have shown that faults often can be approximated with a simple geometry [42]. Observed seismic waves with larger dimensions than the characteristics of the fault plane also makes such idealized models as robust approximations. Another plus with simplified fault models is that it helps with defining and understanding concepts related to faulting. There are quite a few different ways of illustrating the geometry of a fault, but in the literature there seems to be a common terminology [40,42]. A visualization of fault geometry with the basic parameters is seen in figure 2.1.

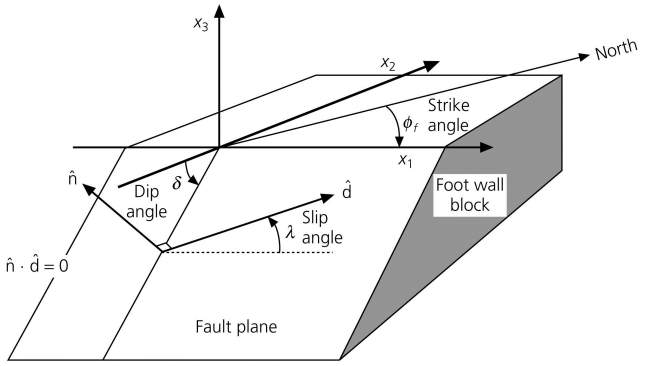

Figure 2.1: The fault plane is defined with normal vector $\hat{n}$ and dip angle δ with the horizontal surface. It moves in direction of the slip vector $\hat{d}$ which have an slip angle λ known as the rake of the fault. The strike ϕ_f, is the angle measured from the local direction of north to the x_1 axis in a clockwise manner. Reprinted from Stein & Wysession [42].

For *strike-slip faults*, when the slip angle is $\lambda = 0°$, the faulting motion is in a left-lateral system whereas when λ equals to $180°$ it is described as a right-lateral system. In their paper, Cleveland & Ammon [14] primarily used observations from the Panama Fracture Zone where the plate boundary motion approximately have north-south striking structures containing strikes-slip earthquakes. The other basic type of faults, *dip-slip faults*, are further separated into normal faulting with $\lambda = 270°$ and thrust faulting with $\lambda = 90°$ [42]. From sensitivity tests with dip, strike and rake Cleveland & Ammon [14] varied these parameters using synthetic seismograms for understanding limitations of the relocation method better. The advantage by having a simple model like in figure 2.1 is that faults that curve and are truly three-dimensional can be viewed as a sum of these more idealized faults. Together, the dip ($0° \leq \delta \geq 90°$), strike ($0° \leq \phi_f < 360°$) and rake or slip angle ($0° \leq \lambda < 360°$) completely characterize the geometry of a faulting event known as the *focal mechanism* [40, 42]. The waveform of seismic waves generated by a fault depends on the fault geometry and direction in which the waves leave the source. As such it is therefore possible to use seismograms recorded at various distances and azimuths for analysis. Any focal mechanism for earthquakes can be represented by a "beach ball" having some variation of strike-slip or dip-slip geometry. As mentioned earlier in addition to being brought up by Barmin et. al. [7], earthquake sources will often have mechanisms quite close to the idealized focal mechanisms. These are illustrated in figure 2.2.

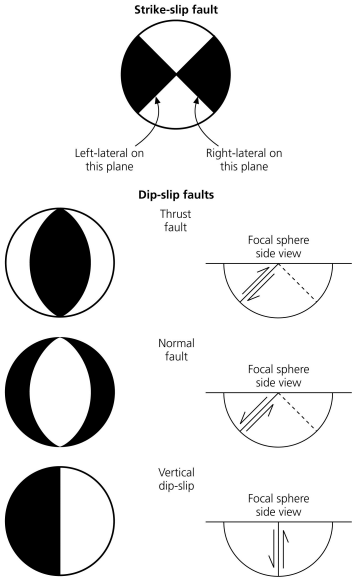

Figure 2.2: Idealized focal mechanisms for earthquakes represented by the "beach ball" image and divided into strike-slip faults and dip-slip faults. The compressional quadrants are filled in with black color while the dilatational quadrants are white. On the right side the fault planes are shown from a side view. Reprinted from Stein & Wysession [42].

The appearance of these are divided into compressional and dilatational quadrants, characterized by first motion on different component seismograms from an earthquake. Generally the first motion is a P wave and records as an upward or downward motion respectively corresponding to the compressional and dilatation quadrants. A fault geometry is uniquely determined if the fault plane and auxiliary plane can be separated. When this is not the case, geological information in the region of interest can usually provide the necessary information to make distinctions between the fault and auxiliary planes. The earthquakes that have been relocated in this thesis between Iceland and Svalbard are shown to mainly have strike-slip and normal faulting or some variation (see chapter 5).

2.4 Moment tensors

Earthquakes are observed to almost always take place on faults, in fact so much that faults can be said to be characterized by the earthquakes they cause [42]. Seismic waves that are registered can provide information on the faulting geometry (or source parameters), including the motion that is produced. To gain this information it is necessary to look at the situation from an inverse problem approach. For theoretical purposes it is possible to use the forward problem to model and describe seismic waves. Earthquakes occurring because of slip on faults are difficult to accurately describe partly because it includes complex rupture processes. However, using *equivalent body forces* and specifically *double-couple forces*, seismic radiation that is produced is good first approximation to the seismic radiation that results from the actual fracture process [42]. A sum of double-couple forces can therefore be used to model larger and more complex sources. One force couple, or two forces pointing in opposite directions, is in a Cartesian coordinate system denoted as M_{ij} where i represent the direction of the force and j the separation axis by a distance d. The other force couple will then be linked to the first and oriented in the orthogonal direction compared to the first force couple. This is analogous to a fault plane and auxiliary plane, so that for double-couple forces, the slip can be put on either planes. A solution to determining the actual fault plane can be by looking at geological information available in the region of interest [42]. The *moment tensor* is defined as

$$\mathbf{M} = \begin{pmatrix} M_{xx} & M_{xy} & M_{xz} \\ M_{yx} & M_{yy} & M_{yz} \\ M_{zx} & M_{zy} & M_{zz} \end{pmatrix}. \tag{2.2}$$

$\mathbf{M}$ provide information about both the fault geometry and its size. The size are determined with the scalar seismic moment, $M_0 = \mu DA$ where μ is the the shear modulus, D the fault displacement and A is the area of the fault [40]. Thus the graphical solution to the moment tensor from a fault can be presented

with the "beach ball". Sources characterized with double-couple forces are considered small compared to the observed seismic wavelength which the seismic energy propagate with so that the simplest case of point sources are relevant. Also, double-couple forces assumes underneath a conservation of angular momentum which is part of why they are good in modeling earthquakes [40]. This requires that the elements in equation 2.2 are symmetric, i.e. $M_{ij} = M_{ji}$, thus having only six independent elements instead of nine.

2.5 Waveform modeling

In order to study focal mechanisms of earthquakes, it is possible to compare observed seismic waves to synthetic waveforms (time series data). These computational synthetic waveforms are modeled to fit with the observations as good as possible. A seismogram will have a distinct waveform depending on the source, the earth structure from the source to the receiver and the workings of the specific seismometer. [42]. If the seismogram is represented by the function $u(t)$, then its Fourier transform can be represented by the frequency-dependent function $U(w)$. Likewise the function $u(t)$ is denoted as the inverse Fourier transform of $U(w)$. Both these functions can be expressed mathematically as

$$\begin{aligned} u(t) &= \frac{1}{2\pi}\int_{-\infty}^{\infty} U(w)e^{iwt}dw \\ U(w) &= \int_{-\infty}^{\infty} u(t)e^{-iwt}dt. \end{aligned} \tag{2.3}$$

By having two forms for the seismogram, either in time domain or frequency domain, it is possible to switch between them depending on which is more preferable to use for analysis. In order to link the factors influencing a seismogram, the *convolution* operation is used. For two time functions $f(t)$ and $x(t)$ convolution is defined as [48]

$$y(t) = f(t) * x(t) = \int_{-\infty}^{\infty} f(t-t')x(t')dt'. \tag{2.4}$$

The seismogram $u(t)$ can be divided into four parts, expressed as $u(t) = x(t) * e(t) * q(t) * i(t)$ as described by Stein & Wysession [42]. Here $x(t)$ represents the source function, $e(t)$ the effects of reflections, conversions and geometric spreading of seismic waves in the earth structure, $q(t)$ represents the attenuation while $i(t)$ is meant as the instrument response of the seismometer. Further, it can be proved that convolution in time domain is identical to multiplication in frequency domain, such that $U(w) = X(w)E(w)Q(w)I(w)$, where the respective functions $X(w)$, $E(w)$, $Q(w)$ and $I(w)$ are Fourier transforms of the time functions.

2.6 Slowness vector and seismic wave types

It is often advantageous to describe the changing propagation by rays instead of wavefronts. Rays are identified by the wavenumber vector $\mathbf{k} = (k_x, k_y, k_z)$ (in a Cartesian coordinate system) being normal to the wavefront. Generally this vector is dependent on which kind of seismic waves are propagating through the medium. Surface waves have general lower velocities compared with body waves and travel only in horizontal directions, not vertically. Assuming a wave travels with velocity v, its *ray parameter* is expressed as the reciprocal of horizontal apparent velocity, $p = 1/c_x = sin(i)/v$, where i represent incidence angle [42]. Alternatively to using the velocity of a seismic wave to connect earthquake and station, the reciprocal or horizontal slowness of the wave can be used. This is particularly useful for the horizontal-traveling surface waves. For example, the relocation solution by Cleveland & Ammon used an average slowness value of 0.245 s/km to characterize the propagation in the PFZ region. It can therefore be said that ray theory is much used for analyzing seismic data, applying it to earthquake locations as well as determining focal mechanisms [40]. With ray theory the complicated nature of seismic waves propagating in a medium is often easier to understand but it also have its use with programming, for example in the *surfaceWaveRelocation_v2.6.py* script.
In situations where the incidence angle exceed 90° a different kind of seismic waves progress. *Evanescent* waves occurs as the incident angle reaches beyond the critical angle of a ray and is dependent on the

incident angle itself as well as the velocity (or slowness). Such evanescent waves propagate along the surface with a decaying displacement as a function of increasing depth.As the name reveal, surface waves have energy mainly close to the surface/shallow depths and generally contain a fair amount of evanescent waves.

2.7 Surface waves

For the reason that seismic waves propagating near the surface are termed surface waves, P waves and S waves described in section 2.1 are grouped together as body waves. They are named so because they propagate through solid volumes and at large depths. Although the velocity of body waves are larger than the velocity of surface waves, the largest amplitudes in recorded seismograms are generally coming from surface waves. Much of the information obtained from seismograms comes from surface waves, especially in the period range 10-200 seconds [**?**]. Further, energy of surface waves decreases approximately as r^-1 whereas energy of body waves decreases approximately as r^-2 [42]. Energy for surface waves spreads geometrically for the most part only in horizontal directions in contrast to body waves that also have energy that spreads vertically, thereby able to propagate through the Earth's core. In situations where there are relatively large distances between source and stations, it would be natural to assume that the surface wave amplitudes often will be the more visible. This is supported with observations of surface waves that are known to be able to propagate around the earth multiple times depending on the specific magnitude of an earthquake [42]. It has been needed to divide surface waves into to basic types named Love waves and Rayleigh waves (after their discoverers) due to different characteristics. That is to say, for a simple model like a laterally homogeneous medium, Love waves are a result of constructive interference from only SH waves while Rayleigh waves are developed from combination of P and SV motions. Although only valid for this idealized system it is still worth describing to give a basic understanding of the difference, similar to the idea behind the basic fault geometries. Both types of these surface waves are described to propagate in path of great circles where the first registered motion come from a minor great circle arc and following pulses from major great circle arcs going the long way around to the station [42]. For large earthquakes there can be many arrivals at a specific station and surface waves propagate at both minor great circle arc and major great circle arc directions. Figure 2.3 illustrate different Rayleigh waves going from the source to the station.

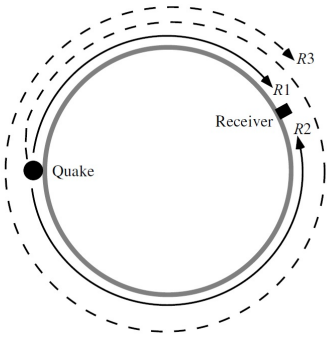

Figure 2.3: The ray path of both even and odd numbered Rayleigh waves are showed, R1 and R3 leave the source in the minor arc direction while R2 leave the source in the major arc direction. R3 is indicated with a dashed line, not being registered at the receiver before going one full round around the earth. Reprinted from Shearer [40].

This is relevant because the time at large distances from an earthquake to different stations the traveltime is a factor to consider. To make sure that energy from surface waves are recorded on seismograms it is necessary to allow for a sufficient time range after the quake has started. The time range is elaborated further in chapter 4. Figure 2.3 also assist in understanding that surface waves are more visible moving closer to teleseismic distances where the energy of body waves are more diminished compared to surface waves.
Amplitudes of surface waves (or seismic waves in general) are affected by distance from the source as well as the earth structure between source and receiver. Due to velocity gradients elastic processes like multipathing and scattering can especially change the appearance or form of surface waves. There is also

an effect to consider where a waveform can have different amplitude for various frequencies, which is a possible explanation for the wave train in figure 2.4.

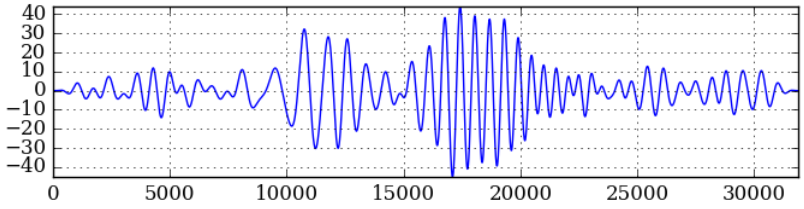

Figure 2.4: A surface wave train from a signal generated by an earthquake occurring 2010-06-03 04:32:42 UTC, with depth 12.4 km and magnitude M_w5.6, close to Jan Mayen. It is registered on station ENH located in Enshi, China (see table D.1). The envelope of this wave train is affected by the amplitude-dip that could have several underlying causes. The plot is drawn with amplitude on the vertical axis and time in seconds on the horizontal axis.

Around the 15000s -mark there is clearly a decreased amplitude value for this surface wave that could have come from elastic or inelastic processes in the earth structure. It is also possible that it is caused by the source depth or focal mechanism. Studying such plots are valuable when considering the relocation method and the solutions that follows from defining relevant parameters. Another plot that do not have this clear reduction is seen below (figure 2.5).

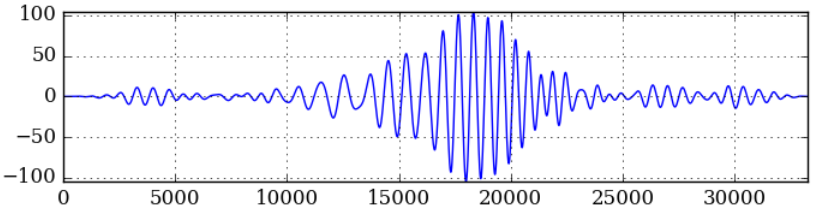

Figure 2.5: Surface wave train from the same earthquake as described in figure 2.4, showing little or no amplitude reduction. It is registered on station KMI located in Kunming, China (see table D.1). It demonstrate that the energy from surface waves decrease with a slower rate compared to body waves at large distances.

2.7.1 Phase and group velocity

In general Love waves and Rayleigh waves are both dispersive for real situations in the earth, meaning the apparent velocity changes with frequency. Simpler models do however describe dispersion as well. As an example it is possible to characterize Love waves in geometries (showing dispersion) that consists of a layer above and having a lower shear velocity in contrast to a halfspace below with a higher shear velocity. Stein & Wyssession [42] shows that by combining displacement in the top layer and the halfspace and then inserting the necessary boundary conditions, a *dispersion relation* is determined that describes the nature of these waves. To describe dispersion for earth models a requirement is vertically velocity gradients in the crust and upper mantle [40]. It is therefore a minimum necessity that relocation of earthquakes using Rayleigh waves should be based on a simple vertical heterogeneous medium. The variation of different velocities with frequency effectively changes the pulse shape of surface waves as they propagate through mediums. This results in interference of different pulses, canceling those with destructive interference and strengthening those with constructive interference. As a consequence the seismic wave pattern develops energy with both a group velocity or *beat pattern* and a phase velocity that is seen as the carrier of the seismic wave [40, 42]. Definitions of group velocity and phase velocity are $U = \partial w/\partial k$ and $c = w/k$ respectively. The group velocity can also be derived to the form $U = c - \lambda\frac{\partial c}{\partial \lambda}$. This form is beneficial considering cases where the phase velocity hardly depends on wavelength, thus the second term basically vanishes and group and phase velocity are made equal (i.e. no dispersion) [42]. It should be noted that the group and phase velocity strictly should be termed horizontal apparent group and phase velocity yet for simplicity the shorter terms are kept.
Another property is that surface waves with longer periods generally travel with group velocities larger

than surface waves with shorter periods [42]. An advantage with the dispersion nature of surface waves is that they can form direct constraints on the velocity and depth profile between the source and receiver [40]. Cleveland & Ammon [14] confirms that Rayleigh wave signals which may be as good as from body waves produce constraints on the relative location of earthquake centroids. The example they use is a teleseismic P wave with horizontal phase velocity of 15-20 km/s and a typical intermediate period Rayleigh wave with phase velocity 3.0-4.0 km/s. Assuming a 16 km distance between an event-pair the P wave would only give a time shift of about 1.0 s in contrast to the Rayleigh wave that would give approximately time shift of 5.0 s. It is not difficult to understand that the larger time shift are determined more accurately due to greater separation of waveforms.
Group velocity curves for fundamental mode Love and Rayleigh waves in the North Atlantic have been determined by Midzi et. al. [33] using the multiple filter technique. In figure 2.6 they are plotted from propagation paths in the Lofoten and Greenland basins, including Mohns Ridge and Knipovich Ridge.

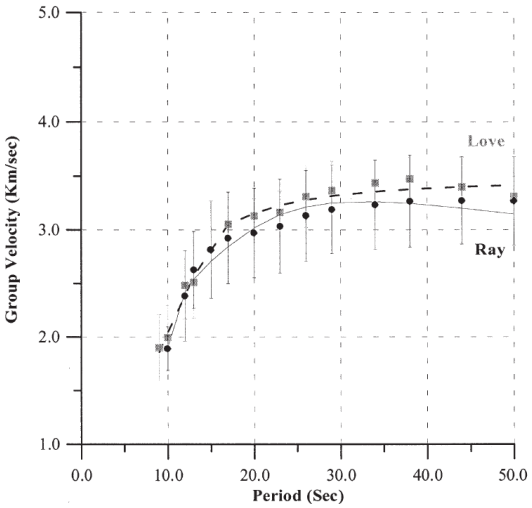

Figure 2.6: The continuous line is the calculated Rayleigh wave curve from observed points. Analogous, the dashed line is the calculated Love wave curve from measurements of group velocities. Vertical bars display the standard deviations found from the curves. The group velocities have been isolated for the period range 10-50 s. Reprinted from Midzi et. al. [33].

The propagations paths in this graph can be said to be relatively similar to the ones taken by the observed earthquakes collected in this thesis. Interesting to note is that Midzi et. al. [33] recognize that the observed group velocities plotted in figure 2.6 are very low compared to other results and where the maximum velocity is even lower than 3.5 km/s. Though there may be some distinction, group and phase velocities of Rayleigh waves appear to be in the same velocity interval. Using the single station method, Weidner [44] found Rayleigh wave phase velocities for different paths in the North Atlantic, partially traveling in the Mid-Atlantic Ridge. The two earthquakes in figure 2.7 are located in the Mid-Atlantic Ridge and velocities are determined with periods from 20-100 s (although some values are measured until the 140 s mark).

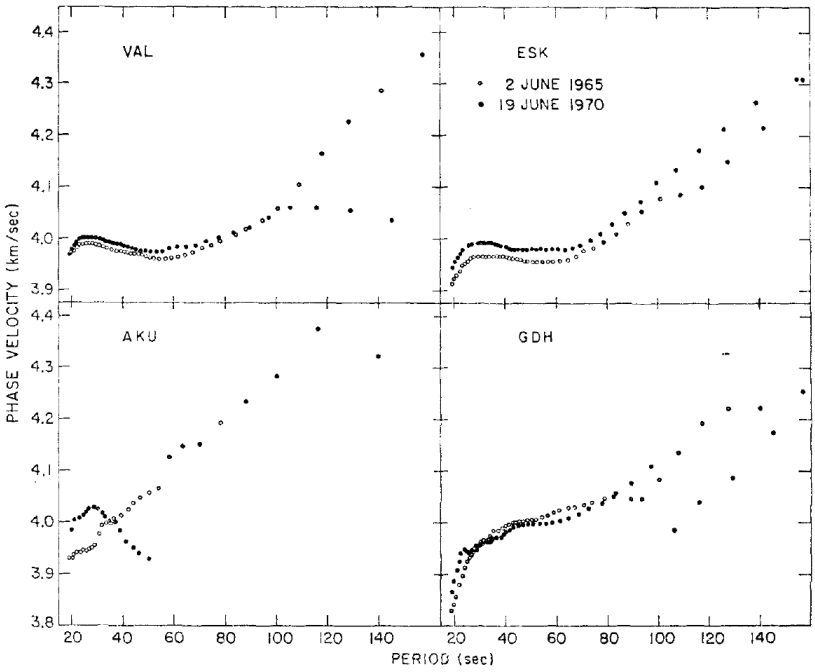

Figure 2.7: Phase velocities for two earthquakes in the Mid-Atlantic Ridge; named *2 June 1965* and *19 June 1970* and registered on 4 different stations (VAL, ESK, AKU and GDH). Reprinted from Weidner [44].

A comparison between the group and phase velocities in these figures show that their values are almost within the same velocity interval, yet at higher periods the phase velocities have a general increasing trend as seen in figure 2.7. Another observation is that the phase velocity pattern for ESK station do seem to have much of the same pattern as the group velocity values at periods from 10-50 s. Extending the comparison brings no substantial advantages because the group and phase velocity values are fundamentally different.

2.7.2 Rayleigh waves

Special attention has been put to Rayleigh waves because the relocation procedure is performed with only Rayleigh waves. Though as Cleveland & Ammon [14] explain, there would not be much difficultly in including Love waves as well for further exploration of the method's validity. The simplest case Rayleigh waves can be modeled in, is in a homogeneous halfspace. Yet in such a model there are no dispersion relations as mentioned earlier for Love waves. Similar to Cleveland & Ammon [14] a vertically heterogeneous medium is chosen to characterize the earthquake excitation. It can be made clearer first by short explaining some general concepts for surface waves; the wave displacement motion can often be described with *potentials* instead of using displacements directly. It can be argued against using potentials in the first place because it is a demanding convention to get familiar with. Determining boundary conditions necessary to solve the wave equation is a clumsy exercise with potentials instead of using displacements directly [?]. A direct approach is taken by evaluating *Green's function* for the displacement formula and the more relevant for this study. In a vertically heterogeneous medium that is bounded by a free surface Rayleigh waves from a point source can according to Aki & Richards [2] be expressed with the two formulas

$$\begin{aligned} u_z^{RAYLEIGH} = \sum_n \frac{r_2(z)}{8cUI_1}\left(\frac{2}{\pi k_n r}\right)^{1/2} exp\left[i(k_n r + \frac{\pi}{4})\right] \times \Big\{ & k_n r_1(h)[M_{xx}cos^2\zeta \\ & + (M_{xy}+M_{yx})sin\zeta cos\zeta + M_{yy}sin^2\zeta] + i\frac{dr_1}{dz}\Big|_h [M_{xz}cos\zeta \\ & + M_{yz}sin\zeta] - ik_n r_2(h)[M_{zx}cos\zeta + M_{zy}sin\zeta] + \frac{dr_2}{dz}\Big|_h M_{zz}\Big\} \end{aligned} \tag{2.5}$$

and

$$u_r^{RAYLEIGH} = \sum_n \frac{r_1(z)}{8cUI_1}\left(\frac{2}{\pi k_n r}\right)^{1/2} exp\left[i(k_n r - \frac{\pi}{4})\right] \times \Bigg\{ k_n r_1(h)[M_{xx}cos^2\zeta + (M_{xy}+M_{yx})sin\zeta cos\zeta + M_{yy}sin^2\zeta] + i\frac{dr_1}{dz}\Big|_h [M_{xz}cos\zeta + M_{yz}sin\zeta] - ik_n r_2(h)[M_{zx}cos\zeta + M_{zy}sin\zeta] + \frac{dr_2}{dz}\Big|_h M_{zz}\Bigg\}. \tag{2.6}$$

Equation 2.5 represents the vertical (z) component and equation 2.6 the radial or horizontal component. To arrive at these equations only the largest Green's function - terms have been kept. The standard form can be traced back to the general formula

$$u_n(\mathbf{x}, t) = M_{pq} * G_{np,q} \tag{2.7}$$

considering a moment tensor representation and the case of point source approximation. A benefit of this solution is that the moment tensor matrix has quite a simple form, depending on the choice of coordinate axes orientation [2]. The expressions in 2.5 and 2.6 have comparable form to the moment tensor point source displacement $u_z(k, h, R, \phi)$ given in Cleveland & Ammon [14]. As explained more in section 4.1 only the vertical Rayleigh wave components are allowed for analysis. Focus is therefore on $u_z^{RAYLEIGH}$ even though the different elements in brackets are the same and only the summation factors are slightly varied. This displacement form is a result from the eigenvalue-eigenfuction problem appropriate due to the necessary conditions required for surface waves. Its solution must be valid for; the free surface z=0 where there are no traction by definition, the limit z=∞ where amplitudes are approaching zero and lastly be specified for the equation of motion [2]. Here n represents the mode number, r_1 and r_2 are two eigenfuctions dependent on receiver depth (z) or source depth (h), c and U are phase and group velocity whereas I_1 is an energy integral for Rayleigh waves defined $I_1 = \frac{1}{2}\int_0^\infty \rho(r_1^2 + r_2^2)dz$. In the exponential the r term is a distance variable depending on the distance from source to station, i.e. not an eigenfunction. The wavenumber k_n is dependent on the angular frequency ω that for surface waves can only give certain phase velocities $c_n = \omega/k_n$. Collectively the first factor not including the exponential function is an amplitude factor depending on the studied earth structure. The Rayleigh wave propagation with phase shift is included in the exponential part. This leaves only the last part reflecting the displacement dependence of faulting depth as well as faulting geometry. It includes the different elements of the moment tensor and the azimuth noted with ζ.
By inspecting the vertical displacement formula that must fulfill boundary conditions it is clear that the eigenfunctions decrease with increasing depth/z value. This is illustrated in figure 2.8, showing the variation with depth of u_x and u_z for a Rayleigh wave in a halfspace. Because the Rayleigh wave is plotted in a halfspace, no variation with depth of horizontal group velocity or phase velocity exist. The same approximation is made in the relocation method by Cleveland & Ammon [14], as they assumed a near constant slowness value. Even though the velocities do not change with depth, figure 2.8 also illustrates that the amplitude or displacement do vary with depth. It is characterized by the eigenfunctions r_1 and r_2, looking slightly different for the structures in the North Atlantic Mid-Oceanic Ridge but still with the same general form. The propagating wave with distance r from earthquake to station also play an important role in that if the distance is relatively large the displacement will likewise have a small relative value, for arguments sake provided the rest of the terms are constant. A similar notion is made by instead of the distance r, the group and phase velocity terms are considered. The moment tensor containing the force couples can simplify the displacement expression depending on the earthquake's fault geometry. For example, Cleveland & Ammon [14] show that for a simple strike-slip earthquake the fundamental displacement mode loses all moment tensor components except for M_{xy}. Determining different displacement expressions for the various fault geometries in the northern North Atlantic Ridge is not easy. However, the idea of a phase shift emerging from cross-correlating two waveforms with different fault geometry is what is central. As a function of azimuth a phase shift is produced with correlating observational waveforms from event-pairs [14]. This is described further in chapter 4.

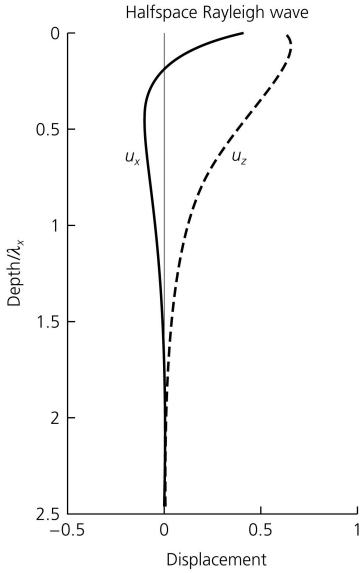

Figure 2.8: The variation of depth for displacement of a Rayleigh wave is plotted with a normalization by horizontal wavelength on the vertical axis, and displacement on the horizontal axis. Reprinted from Stein & Wysession [42].

2.8 Seismological networks

To locate earthquakes it is a necessity to study distributed seismic data. Because of this basic ambition, making data available began more than a century ago [42]. The seismic waveform data used for this thesis are requested from the Incorporated Research Institutions for Seismology (IRIS) which is incorporated in the Federation of Digital Broad-Band Seismographic Networks (FDSN). Thanks to connectivity between scientists and such data centers as IRIS, it is now possible to get free access to high quality, digital seismic data. This progress and historical development should not be underestimated, it is a large part of the reason for making this master thesis achievable. Worth recognizing also is the important work done by the International Seismological Centre (ISC) that gathers earthquake data from about 130 agencies around the world, including NORSAR, having records from 1900 up until today [26]. *The Bulletin of the ISC* provides different data such as hypocenters, phase arrival time and focal mechanisms to mention some. The ISC catalog have been used through IRIS to gather earthquake data from almost all of the earthquakes in the Iceland-Svalbard region.
In theory there are three types of seismological networks, depending on how the seismometers are used but also on their location and covered area [42]. The three types are going from covering the whole earth to a local scale; namely global networks, regional networks and local arrays. For global networks the most important aspect is to have good coverage of seismometers and spread evenly, in contrast to local arrays where the goal is to place seismometers in geometries that are well suited for specific investigations. Global networks have the benefit of studying seismicity on large scales like plate tectonics and mantle convection, yet in certain places (for example in oceanic regions) the station density are often not developed enough to provide a full record of the subsurface. It is for this reason suited also for 3D-tomography and locating earthquakes [42]. An example of two-dimensional local arrays are found deployed in northern Norway, Finland and Germany from NORSAR. Regional networks do monitor seismicity same as local arrays yet commonly over a relative larger area. As the seismology community expands and being more and more interconnected, the characteristics separating the types of networks are naturally becoming more alike therefore making progress and leaps in analyzing information from seismic sources.
Together with U.S. Geological Survey (USGS), IRIS have developed GSN (The Global Seismographic Network) that now consists of more that 150 stations in a global and digital seismological network. This global network can be seen in figure 2.9.

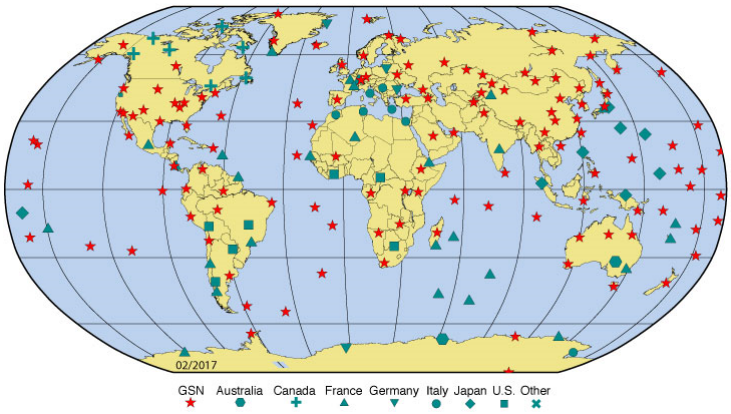

Figure 2.9: Distribution of station networks as of 2017 where the GSN is represented by red stars. This is apart of the FDSN that includes other networks as well (seen in green), divided into which country that are operating the stations. Reprinted from Incorporated Research Institutions for Seismology [25].

The seismic data recorded in GSN are free to access through the IRIS Data Management Center (DMC) that distributes different types of data such as time series data, metadata and event data. The time series data is considered the main archive and have been used extensively in the challenge of precisely relocating earthquakes, for example in Cleveland & Ammon [14] and Cleveland et. al. [15]. To work with and process seismic data different data formats exist, perhaps the most used is the SEED (Standard for the Exchange of Earthquake Data) format. As its name reveals, it is the international standard format used to exchange digital seismological data, largely in use by the earthquake research community [1]. Another format effective for studying time series data is the SAC format, used in the purpose interactive program SAC (Seismic Analysis Code). It includes possibilities in analyzing seismic events as well as viewing the data graphically, for example in computing Fourier transform, filtering the signals and doing correlation [24]. This is the format downloaded from IRIS and applied to the relocation method.

Chapter 3

Relative relocation of earthquakes using DD

3.1 The inversion problem for linear systems

For many aspects in seismology it is necessary to find solutions to inverse problems. Depending on the goal, this approach can for example be used to determine the earth structure by inverting time and amplitude data or studying earthquake sources by inverting waveform and polarity data [42]. Common to all inverse problems in seismology is to start with the seismograms, viewed as the end result of the problem and then working backwards to the starting point, to say something about the characteristics of the source that generated the seismic waves as well as the medium that the seismic waves propagated through. Due to this backwards or reversed way of thinking and the mathematical techniques taken advantage of, it is easy to understand that performing inversion means finding the cause behind the observational data. Unfortunately solving inverse problems is more complicated than solving the forward problems (which is beneficial for describing seismic waves coming from a known source). Fundamentally, it is not possible to precisely explain the form of the seismogram, being dependent on both the source and the medium from the source to the seismometer. Also there will in general not be an unique solution to the inversion, in contrast to the forward problem that is solved in a more clear-cut way [42]. This means that there can be many solutions and they are not without errors given by the observational data. Having a model that fits well with the observations does not infer that the model describe the true physical region that is studied. By such a reasoning there can never be an exact solution in the fact that we are always trying to develop a model for reality. Despite this, more precise and accurate models have been developed from advances such as numerical analysis supplied with experimental data. The inversion methods are widely applied for its strength in being able to work with different types of data as listed above. Even though the details and variables may differ, for example in earthquake location and *travel time tomography* (dealing with lateral velocity perturbations), the general setup of the inversion equations will be the same. In order for the inversion method to produce viable results, it is far from good enough to assume a large simplification of the earth like a homogeneous halfspace. Instead, if a more realistic solution to the forward problem is known and a sensible guess can be made to the parameters, then the inversion method shows its advantageous character. As long as the perturbation from starting or initial guess do not grow too much, it is common practice to linearize the inversion equations [2, 42]. Specifically this can be done by expanding the observational data in a Taylor series about the initial guess or model $\mathbf{m}^\circ$. For earthquake location it is a vector containing four parameters, $\mathbf{m} = (x, y, z, t)$, in a Cartesian coordinate system. If the hypocenter is denoted $\mathbf{x} = (x, y, z)$, or disregarding the depth z by looking at the epicenter (x, y) as well as having stations at points $\mathbf{x}_i = (x_i, y_i, z_i)$ then the arrival time can be expressed mathematically as

$$d_i^{'} = T(\mathbf{x}, \mathbf{x}_i) + t \tag{3.1}$$

The first term is meant to represent the travel time whereas the second represent the origin time. Estimating the data $\mathbf{d}^\circ$ from the initial model $\mathbf{m}^\circ$ is the first step to the linearized inversion method. These two vectors are related by

$$\Delta\mathbf{d} = G\Delta\mathbf{m} \tag{3.2}$$

where G is an operator on $\Delta\mathbf{m}$, often just written $\mathbf{d} = G\mathbf{m}$ for simplicity. This equation is on the form of a forward problem and represent a linear matrix system. For an easier visualization, we can look at a single component such that the equation can be written $\Delta d_i = \sum_j G_{ij}\Delta m_j$. The term Δd_i is equal to the difference between observed and predicted arrival time, G_{ij} is defined as $G_{ij} = \frac{\partial d_i}{\partial m_j}$ and Δm_j is equal to the difference between the true and present model [42]. The subscripts i and j are noted to the station and the model component, respectively. For the problem of earthquake location

Δm_j characterize the true and assumed location of an earthquake. Even though the arrival time is used for theoretical purposes, when doing a three-dimensional velocity inversion or dealing with the double-difference algorithm described in section 3.2, it is equivalent to work with the *residual* travel time, defined as $t_{resid} = t_{obs} - t_{pred}$ [40]. A positive residual travel time signify that the earthquake analyzed is farther away from the station that what is assumed, i.e. the observational travel time value is larger than the predicted travel time value. In contrast a negative residual travel time value signify that an earthquake closer to the station (where it is observed) than it is predicted by the model. Instead of considering only one earthquake with Δm_j for a system of earthquakes it is more appropriate to use the vector $\Delta\mathbf{m}$. This vector include the locations of all earthquakes that are interesting for relocation. Waldhauser & Ellsworth [43] note the differentiation between small clusters of earthquakes where equation 3.2 can be solved with the singular value decomposition (SVD) method and larger systems of earthquakes that solve for the model by the conjugate gradient algorithm LSQR. The latter approach is described by Paige & Saunders [36], however, relative relocation of 86 events by Cleveland & Ammon [14] is well within the boundary what is considered small and therefore not focused on in this thesis. Both these approaches uses iteration, starting with an initial model and then using this information to find a new model closer to the actual solution. Normally the number of steps for the SVD method is 2-3 whereas for the LSQR it lies around 5 steps [43]. In the results from Cleveland & Ammon [14] they found that from the second to the third iteration, the distance the earthquakes moved was insignificant. Relevant for the PFZ and the northern North Atlantic region are the SVD method due to being more capable for smaller systems; this is further described in section 4.5.
Due to generally non-square matrix G, the solution to equation 3.2 is not straightforward. Though this can be solved by introducing the *generalized inverse* matrix G^{-g} defined as $G^{-g} = (G^TG)^{-1}G^T$, giving common least squares solution to the model, $\Delta\mathrm{m} = (G^TG)^{-1}G^T\Delta\mathrm{d}$ [42]. To clarify, having the special case of G being a square matrix it would simply result in $G^{-1} = G^{-g}$.

Before going into the specifics of the methods, it will be beneficial to elaborate on the idea of inversion for determining earthquake locations. Starting by finding $\mathbf{d}^o$ from $\mathbf{m}^o$, the initial misfit $\Delta\mathbf{d}^\circ = \mathbf{d}^{'} - \mathbf{d}^\circ$ is computed. Thereafter the matrix G is evaluated by using the relation $G_{ij} = \frac{\partial d_i}{\partial m_j}|_{\mathbf{m}^o}$. The next step is then to use the solution $\Delta\mathbf{m}$ to find the change in the starting model, $\Delta\mathbf{m}^o$ such that the new model $\mathbf{m}^1 = \mathbf{m}^o + \Delta\mathbf{m}^o$ can be decided. By using the new model, dataset $\mathbf{d}^1$ should be a better approximation to the observed dataset than the estimated $\mathbf{d}^o$ (if the initial model is well estimated to the real model). One way to check this is to make a comparison of the total squared misfit $\sum(\Delta d_i^1)^2 = \sum(d_i' - d_i^1)^2$ to the squared misfit with the initial predicted data $\sum(\Delta d_i^0)^2$. Assuming that the model is improved, the process is repeated or iterated by again determining the G matrix about the new model, $G_{ij} = \frac{\partial d_i}{\partial m_j}|_{\mathbf{m}^1}$. Because $\mathbf{d}^1$ is now known, $\Delta\mathbf{d}^1$ and consequently $\Delta\mathbf{m}^1$ can be resolved. The next model will therefore be found by the relation $\mathbf{m}^2 = \mathbf{m}^1 + \Delta\mathbf{m}^1$. A continuation of this iteration process will hopefully produce smaller and smaller changes in the model, or likewise smaller and smaller total squared misfits, illustrated in figure 3.1 below.

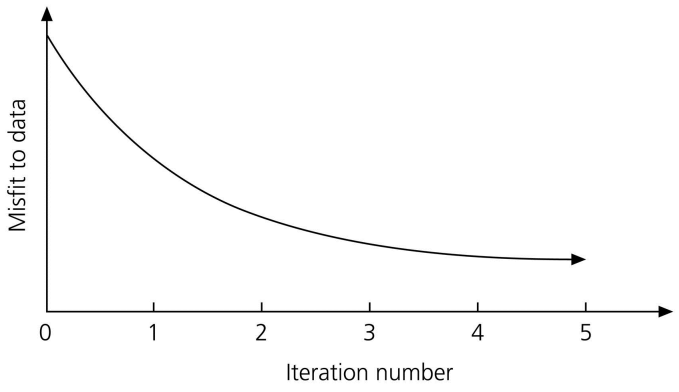

Figure 3.1: The graph illustrates schematically how misfit of data typical decreases with the number of iterations for a linear inversion problem. Reprinted from Stein & Wysession [42].

As mentioned, indications for misfit to data seem in many cases to reach a stagnant point after about three iterations, though this figure depicts still visible decreasing value from the third to the forth iteration number and perhaps even from the forth to the fifth iteration number. Therefore the results for

Cleveland & Ammon [14] may very well not apply exactly for the process with events that lies between Iceland and Svalbard. For example, in the results (chapter 5) the number of iterations have in some plots been created with 4 or 6 iterations, to make certain that the moved event distances are insignificant.

3.2 Double-difference method

Locating earthquakes in oceanic areas with high precision is generally difficult because of (1) limited stations at close range and (2) poor station distribution. A relative relocation between events in a region has the strength of better accuracy compared to an absolute location [40]. By working with difference in travel times between two events at a single station, it is possible to find the relative offset between these two events which can be advantageous for adjustment in relocation. For it to be valid, the hypocenter distance between two earthquakes must be small compared to the distance between the hypocenters-to-the-station as well as the scale length of the velocity heterogeneity. An illustration is presented in figure 3.2 to better the understanding of what assumptions are made and how relocations are done in practical terms.

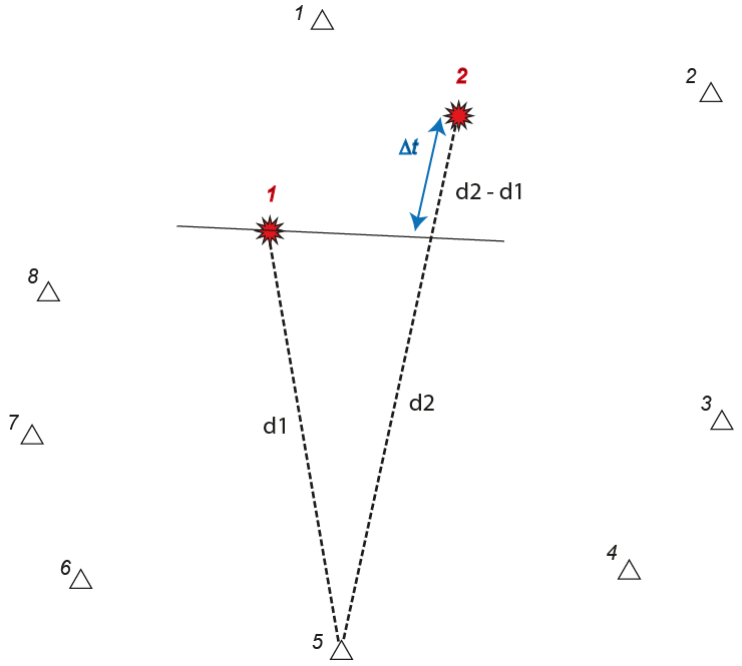

Figure 3.2: Illustration of two earthquakes marked in red that are recorded on the eight stations (represented by the triangles) surrounding them. It is meant strictly as demonstration of how the relative relocation method is done in simple terms, the separation of the earthquakes is greatly exaggerated for this reason. The black line crossing earthquake number 1 is a helping line to visualize the same propagation characteristics except for distance length $d2 - d1$ with time shift Δt.

There are some key elements to this illustration that needs to be in place to have the relocation working properly. First, distance between any two earthquakes cannot be too large such that the seismograms recorded at the stations still have some similarities (see section 4.4). Second, distance from the earthquakes to the stations should be much greater than the distance between the earthquakes. The setup in figure 3.2 is meant to explain this. If distance from earthquake 1 and 2 to station 5 is so large that the seismic wave path can be assumed to be roughly the same, then the only length that needs to be considered is the part that measures difference Δt. In more general terms the seismic energy is considered to travel the same path for all event pairs except in the area around the sources, characterized by a small difference in time (Δt). This can be viewed as contradictory to the point made in the lead-in of this this section, implicating that stations nearby the earthquakes are better than using stations farther away. Such a wanted scenario arises due to analyzing pairs of events rather than single events in traditional location methods. One important assumption in this setup is that the earth structure in the area between the earthquakes and stations are not changing. A vital importance is also the station network surrounding the collection of events, more stations that records the events the better. To constrain the

relocations from the Rayleigh waveforms it is essential with good azimuthal coverage of stations as well. In figure 3.2 an ideal situation would be to have a couple more stations north of the earthquakes. It is much the same situation in the real case, with most of the stations south, west or east from the collection of events. In the northern latitudes there are currently a severe lack of stations, affecting the precision and accuracy of relocations that can be done. Having a comfortable amount of stations in all directions of the event pairs assures a good start for initiating the DD inversion procedure.
The Δt defined here represents difference in observed travel time, exemplified for station 5. Figure 3.2 is drawn only with two events as an example yet to reflect the real case additional events should ideally be added so that it makes up a cluster. The relocation method shows its strength if clusters of events are collected, this requirement has been crucial throughout the maps presented in chapter 5. By running the inversion for all event pairs and all stations, each event is moved relative to all other events that are similar, i.e. that meets the requirements set by the user. Although fracture zones and earthquake activity around the Mid-Atlantic Ridge are not an input to the inversion procedure caution should be taken if events are relocated far from these local areas, potentially signifying that these events diverge somewhat from the general seismic activity pattern. Another point deserving to be stressed is that these events have all occurred on different dates, it is therefore necessary to define a common reference time that allows for determining the difference in observed travel time. Cleveland & Ammon [14] have in their script *surfaceWaveRelocation_v2.6.py* chosen that the reference time is equal to the beginning of the trace recorded by the specific station. Because the linear inversion method is done with the DD-algorithm, the situation is more complicated than using t_{resid} described in section 3.1. An effort on the mathematical description of the DD-method is shown under, however, before performing the inversion it is imperative with a cross-correlation of the traces, detailed more in section 4.4. It is possible by studying the appearance of seismograms from event pairs with how similar or alike they are to see how it is dependent on distance between the events. This can mean that the time difference or time shift can prove unreliable if the event separation is too large, in which case the propagation of the events comes from the outside boundary of the first *Fresnel zone* [43]. Such a challenge can be worked out by examining whether or not there is a systematic cosine variation in the time shift at different stations located in different azimuths from the events [14]. A cosine pattern typically results when there is a difference in event location as for the event pair in figure 3.2. The sketch in figure 3.3 with imagined travel time differences for event 1 and 2 is meant to better visualize this.

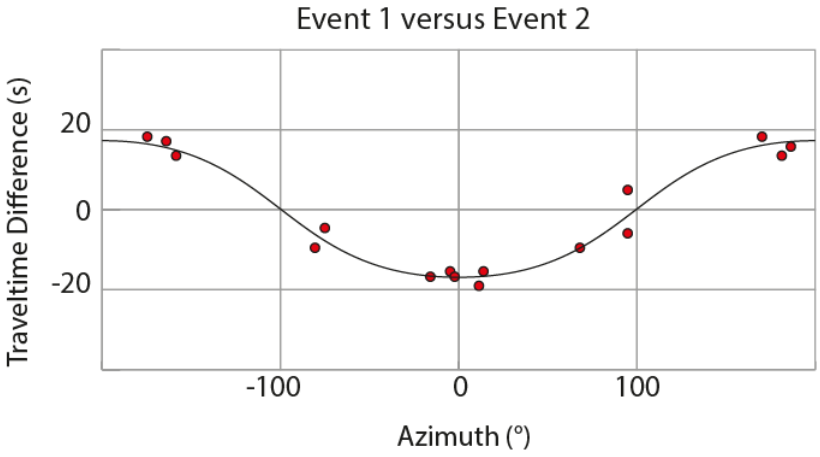

Figure 3.3: The red circles represent hypothetical observed traveltime differences between event 1 and 2 as a function of azimuth. Due to their placement or coordinates on this graph, a cosine fit seems to compare well to the points.

The continuous black line is meant to represent a cosine fit to the data points and is important in terms of analyzing how the travel times between two events behave. If there are few measurements or not a good cosine fit it may indicate a large event distance or that the waveforms are not sufficiently similar.
In theory the DD inversion method works both for body waves and surface waves, so there are no differentiation between these types of seismic waves as the idea of this algorithm is presented. The conditions necessary are dependent on having similar waveforms (at each station) between event-pair

earthquakes such that the source mechanisms are approximately the same. In addition the earthquake sources needs to be sufficiently close together, something that depends on the region of interest. In the work by Waldhauser & Ellsworth [43], they affirm that a relative timing precision of around 1 ms is possible with waveform cross-correlation that can result in a relocation with errors of only a few meters or few tens of meters. A slightly different form of the component equation of 3.2 gives insight into the derivation of the DD method. Here the arrival time from an event i to a seismic station k is expressed in a linear form (derived from a general non-linearity between the travel time and the earthquake location) as [43]

$$\frac{\partial t_k^i}{\partial \mathbf{m}} \Delta \mathbf{m}^i = r_k^i, \tag{3.3}$$

with $r_k^i = (t^{obs} - t^{cal})_k^i$ and t^{obs} and t^{cal} are respectively the observed travel time and calculated or estimated travel time for an event i observed at station k. It can be directly compared to t_{resid} defined in section 3.1. A quick analysis of the units in the fraction $\frac{\partial t_k^i}{\partial \mathbf{m}}$ reveal it's the components of the slowness vector describing the ray from the source to the station. Finally, $\Delta \mathbf{m}^i = (\Delta x^i, \Delta y^i, \Delta z^i, \Delta \tau^i)$ where each parameter symbolize the change of the model in a direction or origin time (the latter is represented by τ). It is easily seen that equation 3.3 do not apply for time shift of two linked events in a double-difference analysis. The DD principle is rather based on waveform cross-correlation which looks at the travel-time difference between two events, $(t_k^i - t_k^j)^{obs}$, i and j symbolizing two different events. Fortunately this challenge can be worked around by taking the difference between two events which can be found to get the following result

$$\frac{\partial t_k^{ij}}{\partial \mathbf{m}} \Delta \mathbf{m}^{ij} = dr_k^{ij}. \tag{3.4}$$

This is quite similar to equation 3.3 with the exception that the change in model $\mathbf{m}$ is considered with the change in relative parameters between two events, $\Delta \mathbf{m}^{ij} = (\Delta dx^{ij}, \Delta dy^{ij}, \Delta dz^{ij}, \Delta d\tau^{ij})$. The fraction is described in the same manner as before though with an assumption of a constant slowness vector for any event-pair. As Cleveland & Ammon [14] points out simple source points have to be necessarily described more realistically as earthquake centroids or epicentroids, the reason being that Rayleigh waves with period range from 30 - 80 s have horizontal wavelengths ranging from roughly 100 km up to 300 km. This is also translated over to the origin time which should correctly be replaced with the centroid time for the arithmetic mean of several origins of a given earthquake. The right side of equation 3.4 is defined by Waldhauser & Ellsworth [43] as the double-difference

$$dr_k^{ij} = (t_k^i - t_k^j)^{obs} - (t_k^i - t_k^j)^{cal} \tag{3.5}$$

with same notation as described earlier. It should be stressed in derivation of the DD equation the slowness vector is taken to be constant, thus its relation is valid only strictly as long as two earthquake events are adequately close to each other. If the distance is too large it cannot be expected to hold, though the actual maximum distance value is dependent on the structure region of interest. A solution where evaluating equation 3.3 for two different events i and j and with subtracting them with each other can be shown to generally be robust [43]. The mathematical form is expressed as:

$$\left(\frac{\partial t_k^i}{\partial \mathbf{m}} \Delta \mathbf{m}^i\right) - \left(\frac{\partial t_k^j}{\partial \mathbf{m}} \Delta \mathbf{m}^j\right) = r_k^i - r_k^j = dr_k^{ij} \tag{3.6}$$

or by writing the equation explicit with all components,

$$\left(\frac{\partial t_k^i}{\partial x}\Delta x^i + \frac{\partial t_k^i}{\partial y}\Delta y^i + \frac{\partial t_k^i}{\partial z}\Delta z^i + \Delta \tau^i\right) - \left(\frac{\partial t_k^j}{\partial x}\Delta x^j + \frac{\partial t_k^j}{\partial y}\Delta y^j + \frac{\partial t_k^j}{\partial z}\Delta z^j + \Delta \tau^j\right) = dr_k^{ij}. \tag{3.7}$$

This is exactly the same as the double-difference equation (3.5) and therefore it has been fully connected to inversion equation 3.2 to complete the basis of the relocation method. Equation 3.7 is a difference expression of the partial derivatives of traveltimes t with respect to coordinate directions x, y and z for events i and j. The origin times τ is also included as well are the changes in hypocentral parameters, Δx, Δy, Δz and $\Delta \tau$ for step-wise improving the model to the observational data. Because we use surface waves and not body waves, we need to assume that the earthquakes have similar depths and so the depth is assumed to be kept fixed. Of course, for events in the datasets the depths do vary roughly within the shallow earthquake interval and therefore the relocation method by Cleveland & Ammon [14] is only an approximate method. Additional assumptions apply for the relocation method and depth was only used

as an example to highlight this point. The DD equation is simplified by omitting the z parameter to effectively

$$\left(\frac{\partial t_k^i}{\partial x}\Delta x^i + \frac{\partial t_k^i}{\partial y}\Delta y^i + \Delta\tau^i\right) - \left(\frac{\partial t_k^j}{\partial x}\Delta x^j + \frac{\partial t_k^j}{\partial y}\Delta y^j + \Delta\tau^j\right) = dr_k^{ij}. \tag{3.8}$$

It can be combined to finally study all event-pairs observed at all available stations in a system of linear equations expressed in vector-form as:

$$\mathbf{WGm} = \mathbf{Wd}. \tag{3.9}$$

Represented by $\mathbf{G}$, the matrix of size $M \times 3N$ of partial derivatives M signifies the number of double-difference observations and N the number of events. The vector $\mathbf{d}$ consists of the double-differences, $\mathbf{m}$ the model vector with a length of $3N$. Finally the vector $\mathbf{W}$ is a diagonal matrix included to weight the two sides accordingly with *a priori* information. Excluding $\mathbf{W}$, equation 3.9 has the same form as equation 3.2. Because of limited information enclosed in the matrix $\mathbf{G}$, the solution can become numerically unstable. This is a common consequence when dealing with earthquake locations and is therefore given a great deal of attention in the literature [2, 42, 43]. The number $3N$ will in most cases have significantly fewer values than the number of DD observations M. Such situations are not problematic in itself but having the general form of equation 3.9 presents *overdetermined* problems as described by Stein & Wysession [42]. For the DD-based inversion method this transforms as numerical instability. The solution of equation 3.9 can be stabilized by introducing a prefiltering where only event-pairs that have a minimum number of station observations are included in the inversion method [43]. This requirement makes the solution more regularized in contrast to not limiting this characterization of event-pairs. The number of observations is defined by Waldhauser & Ellsworth [43] as number of links between event-pairs that are robust. What this robustness involve is elaborated on in chapter 4. Cleveland & Ammon [14] uses the term *unlinked events* for earthquakes that have for whatever reason not been relocated. Throughout this thesis unrelocated events and not linked events therefore mean exactly the same. At the PFZ, Cleveland & Ammon [14] determined this number to 12 by trial-and-error, a number which depends on the events in the region as well as the station distribution around the events. As such equation 3.9 should not contain events that are not well linked to other events [14, 43]. There may be several causes for why an event pair should not be taken into the DD inversion method, for example that the distance between them are very large or that their cross-correlation value is relatively low. The first point can be partially dealt with since the equations in 3.9 can be reweighted according to the distance between event pairs, calculated from the misfits (in each step). Here lies much of the entire premise to confidently estimate precise and accurate event locations over quite extensive regions, namely that the Rayleigh-wave traveltime observations have high waveform similarity and each event is linked with a multiple of other nearby events in the DD inversion procedure.

Chapter 4

Data collection, processing and plotting

4.1 Catalog search

The seismic waveforms or time series data are gathered from IRIS or more correctly from the IRIS DMC. The purpose of the IRIS DMC, located near the University of Washington in Seattle, is to archive as well as distribute high quality seismic data easily to scientists around the world [28]. There are several data types available at IRIS, with time series data, metadata and event data as three examples of this. Although the time series data type make up most of the seismic data collected and archived at IRIS, these data types are not all mutually exclusive. The search tools *Wilber 3* and *JWEED* can be used to transfer seismic data from events and having the waveform format. Additionally, the earthquake catalogs used for the most part at IRIS are the Preliminary Determination of Epicenters (PDE) bulletin of the National Earthquake Information Center (part of USGS) and the ISC. Important to note is that the ISC bulletin do not contain observations for the last two years counting from present time. The digital seismometers available today are largely versatile in broadband systems since they can record seismic waves over broad frequency ranges [42].
Historically, there have been many different approaches for naming channels and with introduction of modern instruments as well as different networks needing to cooperate, the goal of having a standard for channel naming has been complicated [21]. The SEED format (as mentioned in 2.8) have such an standardization for different sensor channels that can display different parts of the spectrum. It uses three letters for naming seismic channels to provide complete information about the type and placement of sensor in the seismometer. The three letters make up the *channel code*, specifying type of sensor, bandwidth as well as the orientation of the sensor. In this terminology, broadband seismometers are represented with B for broadband [21]. The collection of letters placed first all go under a table of band codes, specifying the possible sample rate and response band of the instrument used [21]. B has a general sampling rate (Hz) in the range $[10, 80]$ where this interval notes the number of samples per second. The following two letters indicate the instrument code and the orientation code. An instrument code is essentially the letter that informs about what instrument type being used or what is being measured. Three examples of instrument types are the *High Gain Seismometer* with the letter H, the *Low Gain Seismometer* with the letter L and the *Gravimeter* with the letter G [21].
Lastly, an orientation code is the third letter in the channel name that informs about which direction the sensor have made measurements. As Halbert [21] explains, there are different groups depending on how the directional system is defined. Of interest here is the traditional orientation with orthogonal directions termed North (N), East (E) and Vertical (V). It should be stressed that these definitions are meant only for seismometers, for other instruments there may be slightly different instrument and orientation code. In this thesis the primary objective is to use only Rayleigh waves for relative relocation of earthquake, such that to remove Love wave energy to a large degree, the channel BHZ is the only channel used. It is justified by the knowledge of Love waves are seen mostly on the transverse component whereas Rayleigh waves are visible on the radial and vertical components [42]. Regarding the description so far, special emphasis is put on the first and third letter of the channel BHZ, being of vital importance to the inversion method and successfully relocating the earthquakes in the north North Atlantic.
The SAC interactive program, as introduced in 2.8, reading in SAC data files, can do seismic processing of the recorded waves. Unfortunately, the SEED format cannot directly be used for data processing before being converted to other formats such as the SAC format [1]. In doing an event-based catalog search, there are many more options to consider for narrowing down to the wanted observational data. In the preliminary stage it can be said to be three main specifications that must be decided to collect a set of earthquake data, regardless of the interface or approach taken. The first one is choosing the starting and end date for which to make a search of earthquakes in this time period. Depending on the size of

region that is considered (being the second specification), the time period cannot stretch over too long such that the amount of seismicity or number of earthquake events will be too large to work with. On the other hand, the time period should be long enough as to see a seismicity pattern, perhaps especially if mid-oceanic ridges are studied. Concerning the problem, there will naturally be large variations of this specification. Already mentioned are the latitude and longitude limits that must be specified for a catalog search. This will in an easy way solve itself with the goal of the study or investigation. The third and last preliminary specification to be made is the magnitude (described in section 1.1) limits. If possible, and in most cases, only looking at the moment magnitude M_w will provide a well enough range of earthquake sizes. Unless the range of the earthquake magnitude is very narrow because it is wanted in the investigation, this specification can also often solve itself by the boundaries that make up the interesting area.

4.1.1 Wilber 3

For gathering event-oriented data the web application Wilber 3 [11] was used in the beginning phase as well as in the later stages of the thesis. It is build up of an interactive map and a set of interactive controls where the user have the options to filter the search for an event by location, date and magnitude (as explained earlier in this section). Once an event is chosen, further sorting consists of selecting which network(s) to request data from, which channel(s) and setting a distance range as well as an azimuth range to the stations that will have records from the earthquake events. Lastly, there is also the option to set the time range of the waveform data counting from the event time, the P wave or S wave arrival. The data types available when making a request include the SEED and SAC formats as previously mentioned. In this case the GSN network described in section 2.8 was chosen and the BHZ channel for the reasoning described in the beginning of section 4.1. A more detailed description of waveform data is also available, i.e. viewing plots either from several/all stations or a single station and the different phase arrival times. After everything is defined by the user, the data can be downloaded after only a few minutes. An obvious downside to this web application is of course that it is only possible to make request for one event at a time. This makes Wilber 3 unpractical for large datasets, but as the method for relative relocation of events in the north North Atlantic is the same as in the study of the PFZ by Cleveland & Ammon [14], the number of events going through the inversion are in no more than two digits. Figure 4.1 illustrates the Wilber 3 interactive map developed by the IRIS DMC [28].

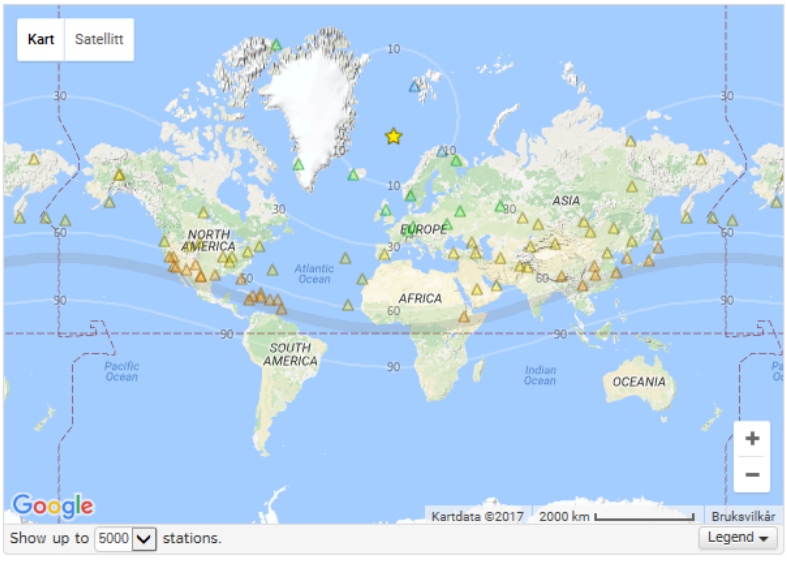

Figure 4.1: Map over an earthquake in the Norwegian Sea with $M_w = 6.0$ at date 2009-08-20 06:35:05 UTC, depicted with the yellow star. The triangles represent stations that have been included with recorded time series files, where blue triangles are located less than 10° from the event, green triangles between $10 - 30°$, yellow triangles between $30 - 60°$ and the orange triangles between $60 - 90°$.

The earthquake 2009-08-20 06:35:05 UTC in figure 4.1 is registered on 80 stations which are all listed in table D.1. Some of the events collected in the datasets may have slightly more stations than

this earthquake and some are registered with fewer stations. In general earthquakes dated earlier are registered with fewer stations, for example the earthquake labeled 1990-05-27 21:49:35 UTC that only has 13 stations. Details for all events that have been downloaded are listed in the appendices. These data originates from both the ISC and NEIC PDE catalogs. Even though Wilber 3 is easy to use and provide information about each event and station, the software program JWEED has the option to request many events at a time.

4.1.2 JWEED v. 4.1.3

JWEED is a Java client that can be installed on Mac, Windows and Linux operating systems, able to obtain data either event-oriented or station-oriented [12]. Of interest here is making event-oriented requests, this can be done in a similar way as with Wilber 3. Going into details of using JWEED will be more intricate than of interest here, yet with a short characterization is it possible to successfully do a request and download the data. The current version is 4.1.3, released in 2015, fixing an important problem with incorrect origin times in the SAC-format. Looking for finding the set of events first, the start time, end time, magnitude range and depth range are decided by the user. The next step is to use a latitude/longitude drawing tool where events inside of this are loaded such that an event query can be done. As with Wilber 3, the events can further be limited by determining the network(s), channel(s) and with the added option to choose a catalog wanted in the study, which is all done when making the station query. Depending on the size of the latitude/longitude box, a new box should be drawn in order to have a minimum amounts of stations that the records are taken from. After the data request is finished listing, the seismograms can be saved in various file formats as SAC, SEED and so on. Because this downloads all events onto the disk, the running time is reliant primarily on the number of events. Being very similar to Wilber 3 in terms of the options available, much of the same specifications can be made in JWEED. One substantial difference however is the length of the time period from which the events are taken from. Wanting to not having hundreds of events to download, the time period using JWEED will be limited to a couple of years, in contrast to data collections made with Wilber 3 which is easier to include longer time periods. An example of this is again the 39 events in table A.1, starting from 1998 and ending in year 2016. However, as this software was installed on a personal computer, the technical limitations proved to not download events with a dense enough collection of events. Therefore JWEED has not been used in this master thesis (even though it has the potential to be useful) to effectively collect data, although it would likely made the relocation procedure easier if this could have been solved.

4.2 SAC v. 101.6a

The SAC interactive program and the SAC format were briefly mentioned in subsection 2.8. Elaborating on the SAC program and especially the SAC format, all waveform data in the SAC format is readily available for seismic processing as well as for cross-correlation that can be used in the iterative inversion method. Benefits of the SAC interactive program have been taken advantage of mainly through the scripts provided from Cleveland & Ammon cleveland13. Working with time-series data in SAC on an expert level requires time and lots of experience, fortunately it is relatively easy to get into and learning the basics, because it contains default values for operational parameters in the data files [24]. Studying seismic events such as earthquakes can thus be done also on a basic level, freeing up time and focus to instead do simple analysis, routine processing as well as more detailed investigations with the added opportunity for high quality plotting. To perform these tasks, SAC expects different commands from the user, having the opportunity to choose from over 200 commands in the current version [23]. A signal from an earthquake is recorded on a seismometer and saved in a SAC data file which contains a header providing information about the signal. Figure 4.2 is an example of a SAC header, taken from the earthquake labeled 2010-06-03 10:16:14 UTC, located in the Jan Mayen region.

```
FILE: ./HK.HKPS..BHZ.M.2010.154.044353.SAC - 1
-----------------------------------------

      NPTS = 146400
         B = 5.000000e-04
         E = 3.659976e+03
    IFTYPE = TIME SERIES FILE
     LEVEN = TRUE
     DELTA = 2.500000e-02
    DEPMIN = -8.169000e+03
    DEPMAX = 8.344000e+03
    DEPMEN = 5.917188e+02
   OMARKER = -671.02
    KZDATE = JUN 03 (154), 2010
    KZTIME = 04:43:53.019
    IZTYPE = BEGIN TIME
     KINST = Streckei
     KSTNM = HKPS
     CMPAZ = 0.000000e+00
    CMPINC = 0.000000e+00
       STLA = 2.227760e+01
       STLO = 1.141415e+02
       STEL = 1.963000e+02
       STDP = 0.000000e+00
     KEVNM = Jan Mayen Island
       EVLA = 7.066630e+01
       EVLO = -1.433080e+01
       EVDP = 1.240000e+01
       DIST = 8.951396e+03
         AZ = 4.731189e+01
        BAZ = 3.446743e+02
      GCARC = 8.059128e+01
    LOVROK = TRUE
     NVHDR = 6
     SCALE = 2.508770e+09
    LPSPOL = TRUE
    LCALDA = TRUE
    KCMPNM = BHZ
    KNETWK = HK
```

Figure 4.2: A SAC header from a signal of an earthquake in the Jan Mayen Fracture Zone, occurring on Jun. 3, 2010. The header variable *KCMPNM* represent the channel name that in this case is the BHZ channel.

It is important to note that not all SAC headers include the same entries, although some, like the number of data points, the start and end time and the file type are always provided. Particular attention should be put on the *IZTYPE* variable, representing the reference time. For my setup and perhaps in many normal situations the description chosen is the *IB*, symbolizing begin time for which time system the data file is applied into. Other central SAC variables are; the *NPTS* giving the number of points in the data set (as seen in figure 4.2 this is for the Jan Mayen earthquake equal to 146400), *B* and *E* noting the beginning and ending time value respectively, and *DELTA* representing the time increment with evenly spaced samples [24]. For the rest of the SAC variables the Seismic Analysis Code Users manual [24] and Hellfrich [**?**] are good sources of extensive information. In relations to the variable *IZTYPE*, both in Wilber 3 and JWEED v. 4.1.3, the description *IB* has to be added to the SAC header in order to successfully perform the numerical processing as well as the inversion method. This is done with a simple SAC macro where the SAC commands *CHNHDR* and *WRITEHDR* are used, able to change a header variable to a specific option and after saving the time series files to the disk [24].

4.3 Structure and seismogram processing

After obtaining datasets from either Wilber 3 or JWEED, the scripts made available from Cleveland & Ammon expect the waveforms structured by event such that the recorded seismograms to a particular earthquake are all gathered in one folder [13]. This makes possible seismic processing of waveforms as well as applying the mathematical inversion techniques as described in chapter 3. Specifically, the seismic processing has been done through a python script named *pySACio_2.py* which also reads in the SAC files and saves them for further use after processing in HDF5 files [13]. In order for *pySACio_2.py* to be functional, the Python library *SciPy* (depending on the *NumPy* package) [30] and the Python framework for processing seismological data [8], have to be imported. The functions *cosTaper* and *detrend* in the script respectively tapers the seismological trace as a cosine and removes the linear trend from the recorded signal. Additionally a Butterworth-bandpass filter [8] is applied to only pass through frequencies within a certain range and discard the frequencies outside the range. Being the reciprocal of frequency, the period range in the case for surface waves used by Cleveland & Ammon [14] are going from 30 to 80 s. Within this interval they chose an average slowness value fitted to the period range. They also decided to only focus on vertical component Rayleigh wave seismograms due to a consistent good signal-

to-noise ratio in the chosen frequency band. Still, as they explain, there is no fundamental difference with also taking advantage of Love waves. As mentioned in section 1.2, only Rayleigh waves are regarded for the inversion procedure. The challenge of cycle-skipping can often arise when performing inversion of seismic data, specifically when the difference between predicted and observational data are larger than a half cycle [32]. Fortunately this problem can be reduced significantly if access to lower frequencies is available. Therefore the motivation of filtering the signals in the period range from 30 to 80 s as done by Cleveland & Ammon [14] is also a reason for avoiding the chance of cycle-skipping. They found that when the signal-to-noise ratio was below 4, some cycle-skipping started to occur depending on the nature of the noise. Much of this is fortunately countered with quality control related to the cross-correlation (section 4.4) embedded in the scripts. To further isolate Rayleigh waves the chosen time window is defined using a group-velocity window with minimum and maximum propagation velocity. Such a task effectively filters away P and S wave phases. The next step after seismogram processing is performed is cross-correlating the traces from each event pair with the python script *surfaceWaveRelocation_v2.6.py*.

4.4 Cross-correlation

The purpose of *cross-correlation* is simply put to measure how similar two signals are and what the time difference between them is. It can be defined with a normalization factor as

$$C(L) = \lim_{T\to\infty} \frac{1}{T} \int_{-T/2}^{T/2} x(t)f(t+L)dt, \tag{4.1}$$

according to Stein & Wysession [42], where in this case it is integrated in time from $-T/2$ to $T/2$. These two signals $x(t)$ and $f(t+L)$, the latter shifted by the *lag time* L, are cross-correlated in a similar operation as convolution described in section 2.5, though with an opposite sign of the time shift. Of interest in particular is the largest peak or maximum value in the cross-correlation operation that gives the lag or arrival time difference between two phases [42]. For a maximum cross-correlation value the relevant lag is equal to the time difference or time shift where phases are most similar. It is understood that similarity in this context refers to waveform similarity. Without a high waveform similarity, the time difference or time shift has no useful meaning. Further, the benefit with high waveform similarity generally expresses as comparable faulting geometry and depth for any two events that will be linked together [14]. Because the recorded waveforms represent the continuous recording of Rayleigh waves with discrete time series points, the cross-correlation operations and the relating Fourier transforms as well as inverse Fourier transforms necessary to analyze surface wave trains have to be calculated accordingly. The cross-correlation function in the python script *surfaceWaveRelocation_v2.6.py* is simply defined as the conjugate of a seismogram multiplied with another seismogram. This is done in the frequency domain by Fourier transform operation. Afterwards it is converted back to time domain with the inverse Fourier transform. For Fourier transforms and inverse Fourier transforms to be calculated on a computer, the established algorithm *Fast Fourier Transform (FFT)* can determine the discrete and inverse discrete versions of these functions noted respectively as *DFT* (Discrete Fourier Transform) and *IDFT* (Inverse Discrete Fourier Transform) [42]. As it name implies, the FFT calculates these functions rather effectively, instead of requiring roughly N^2 operations (N representing number of sampled time points) it uses $Nlog_2N$ operations [42]. In the SAC header in section 4.2 with 146400 time points, the number of operations necessary to calculate DFT and IDFT for the two expressions are:

$$\begin{aligned} N^2 &\approx 2,14 * 10^{10} \\ Nlog_2N &\approx 2512159. \end{aligned} \tag{4.2}$$

With the FFT algorithm this means that the number of operations for the file in figure 4.2 are approximately 8500 times less, making the seismic processing much faster, particular beneficial perhaps when dealing with event datasets of the sizes here. To illustrate the waveform cross-correlation calculations, the plots in figure 4.3 and figure 4.4 shows respectively how two similar or rather different phases results in contrasting seismograms at the top. In both figures the vertical axis shows values for the amplitude (units differ depending on the signals strength), while the horizontal axis marks the time in seconds. Figure 4.3 is taken from station CCM located in Missouri, USA (see table D.1 for more detailed information). This cross-correlation is calculated from the earthquake 2015-01-22 00:39:16 UTC (the middle seismogram) and the earthquake 2015-06-09 19:23:55 UTC (bottom seismogram). Figure 4.4 is taken from station

KIV located in Kislovodsk, Russia. The cross-correlation here is a result from the earthquakes 2010-06-03 10:16:14 UTC (middle seismogram) and 2008-01-15 06:55:27 UTC (bottom seismogram). It is clear by comparison of the two figures that the signal pair in figure 4.3 display definitive envelopes in contrast to the bad signal pair in figure 4.4. In the first case we see a well behaved waveform with a maximum value of about 7 s, i.e. the lag.

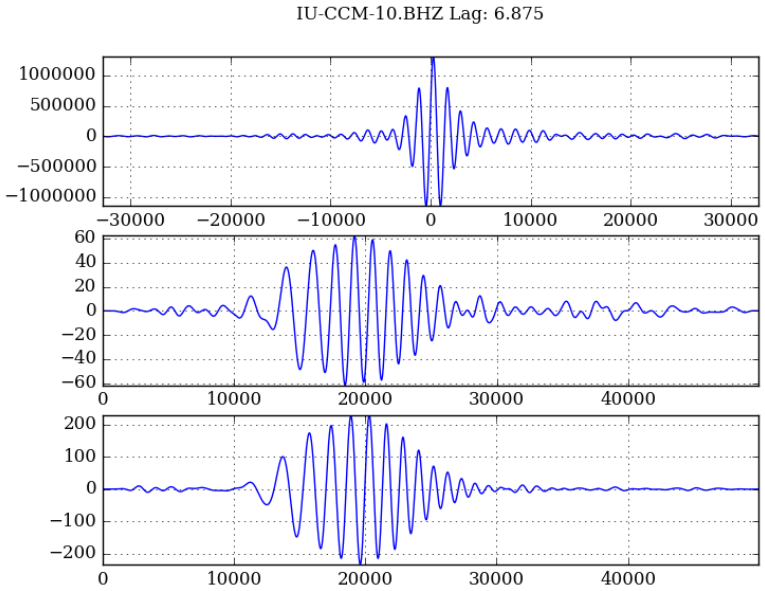

Figure 4.3: The envelope pattern of a typical surface wave is shown in the two bottommost seismograms, giving a clear maximum value of the cross-correlation at the top seismogram.

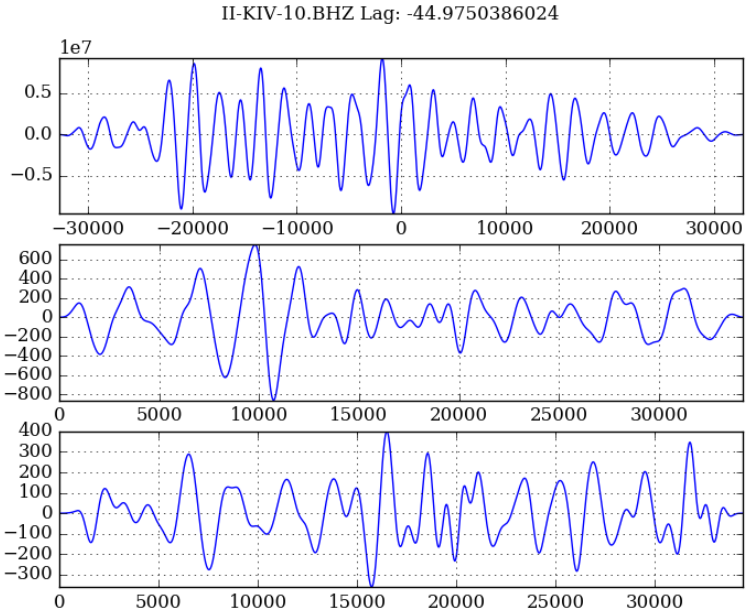

Figure 4.4: In the two bottom seismograms there are no typical surface waveforms, instead they are largely dominated by noise. It therefore results in a cross-correlation with a maximum value that cannot be used in the inversion method.

By doing cross-correlation it contribute two things as brought up earlier; a time shift is required to perform the DD inversion method and also it gives a measure of how similar the waveforms are, of

phases from two linked events. Figure 4.4 is an example of low signal-to-noise ratio that clearly affect the cross-correlation result. Fortunately the work done by Cleveland & Ammon [14] assures quality by removing much of these results. Their sensitivity tests shows that the effects of depth and especially faulting geometry on cross-correlation must be carefully considered when trying to relocate the events from a catalog search. For PFZ they decided on a threshold CC-coefficient (cross-correlation normalized to 1.0) of 0.90 to assure that only waveforms that produce cross-correlation coefficients of 0.90 or higher be included. Because the northern North-Atlantic Ridge is a complicated structure with different focal mechanisms, mainly strike-slip and normal faulting, the same CC-coefficient was chosen for all parts of the ridge system.

4.5 Singular value decomposition using LAPACK routines

Instead of using Cartesian coordinates in the DD equations, Cleveland & Ammon [14] applies a spherical earth version with partial derivatives of the arrival times, having the form

$$\begin{aligned} \frac{\partial d_i}{\partial \theta} &= \frac{\partial T(\Delta_i, z)}{\partial \Delta} cos(\zeta_i) \\ \frac{\partial d_i}{\partial \phi} &= -\frac{\partial T(\Delta_i, z)}{\partial \Delta} sin(\theta) sin(\zeta_i). \end{aligned} \tag{4.3}$$

This is derived elegantly in Stein & Wysession [42] with the same parameters as described in section 2.2, thus effectively changing the parameters of the model vector to $\mathbf{m} = (\theta, \phi, t)$. A typical way for solving equation 3.9 is to find the normalized least-squares solution or equivalently minimizing the L2-norm. This can be expressed mathematically as
$\hat{\mathbf{m}} = (\mathbf{G}^T\mathbf{W}^{-1}\mathbf{G})^{-1}\mathbf{G}^T\mathbf{W}^{-1}\mathbf{d}$. Because we are dealing with a set of events that is smaller, it is possible to take advantage of the SVD method as introduced in section 3.1. This actually comes, as Jia [29] describes, from wanting to solve the system using a numerically stable algorithm as well as doing it without being too time consuming. In this regard, finding the solution with a least-squares method or Gaussian elimination is to an extent known for not being numerically stable nor being appropriate for overdetermined systems. The frist step in the SVD method is to compute the matrix $\mathbf{G}$ (size mxn) by making the following decomposition: $\mathbf{G} = \mathbf{U}\mathbf{\Lambda}\mathbf{V}^{\mathbf{T}}$. The term $\mathbf{\Lambda}$ is the diagonal matrix of singular values of $\mathbf{G}$, whereas $\mathbf{V}$ and $\mathbf{U}$ are the orthogonal matrices of singular vectors of the matrix $\mathbf{G}$, possibly including the weighting $\mathbf{W}$ [29, 43]. There is a similarity between the Gaussian elimination and the SVD approach, both looks to find the $\mathbf{m}$ that when taking the product with $\mathbf{G}$ minimizes the error to the observational data $\mathbf{d}$. Both finds the minimum norm in a least-squares sense. Though as Jia [29] argues, in the SVD method there are both pre-multiplication and post-multiplication with orthogonal matrices, consequently decreasing the possibility of having noise and errors affecting the solution, as can be the case with Gaussian elimination. The pre-multiplication comes from the matrix $\mathbf{U}^{\mathbf{T}}$ while the post-multiplication comes from the matrix $\mathbf{V}$. For the general case where $\mathbf{G}$ is not a square matrix the mathematical expression for the SVD method, presented by Waldhauser & Ellsworth [43], is:

$$\hat{\mathbf{m}} = \mathbf{V}\mathbf{\Lambda}^{\mathbf{-1}}\mathbf{U}^{\mathbf{T}}\mathbf{d}. \tag{4.4}$$

By representing the pseudoinverse of $\mathbf{G}$ as $\mathbf{G}^+ = \mathbf{V}\mathbf{\Lambda}^{\mathbf{-1}}\mathbf{U}^{\mathbf{T}}$, equation 4.4 can also be written as $\hat{\mathbf{m}} = \mathbf{G}^+\mathbf{d}$. As long as a set of events remains small and behaves well, the SVD method is often used for solving linear problems. After determining an initial solution $\mathbf{d}^o$ to equation 3.9, *a priori* weights, residuals and the partial derivatives must be updated to continue the inversion method. In the case of Cleveland & Ammon [14] the weighting, dependent on the distance between the events, begins with the original epicenter locations and is then continuously reweighted as the locations are moved. This is slightly different from iterating just using *a priori* information until a stable solution is found. After the first step, the weighting takes into account the result from the calculated misfit of data and the distance between event-pairs [43]. Using a catalog search to collect the events similar to Cleveland & Ammon [14] as well as using their relative relocation method, it is not surprising that the results (provided in chapter 5) converge with approximately the same number of iterations.

In practice, the SVD algorithm is carried through by the software package LAPACK (Linear Algebra PACKage) providing routines in linear algebra. It it structured with driver routines that among other

things can solve linear equations and singular value problems, computational routines that are used for specific calculation tasks and lastly auxiliary routines used for subtasks or more simpler computations (like the scaling of matrices) [5]. The driver routines are in this way at the top hierarchically and can pick out sequences of computational routines necessary for dealing with problems in linear algebra. In particular, a matrix factorization such as the SVD is handled by the computational routines. As Anderson et. al. [5] describes, an advantage with LAPACK is that it can be used for both high performance workstations as well as scalar machines that for example could be PC's. Since version 3.2 LAPACK is written in the programming language Fortran 90 (superseding Fortran 77) and with this additional routines and functions to better the performance [5,34] which includes faster computation of the SVD. The LAPACK routines are to a high regard performing the computations by making requests to the BLAS (Basic Linear Algebra Subprograms) that strictly is not a part of the LAPACK but include routines for vector and matrix operations [35]. The benefits of BLAS is that it is efficient, easily available and transportable, meaning that LAPACK implements well on different types of modern machines. It have been made possible by designing LAPACK to supersede the software packages LINPACK and EISPACK with combining algorithms from these two as well as adding new algorithms and functionality [5]. Even though only real data is used for the inversion method here, LAPACK routines can work with complex data equally well. Further, the routines are all adapted to both single and double precision versions effectively influencing the amount of information used in the computations. This has relevance in the naming scheme of the routines where the first letter can be noted as one of the following: S, D, C and Z representing real (and single) data, double precision, complex data and double complex data, respectively. The driver routines and the computational routines have this common form generally written as **XYYZZ** [5]. Here the two letters **YY** is an indication the the type of matrix whereas a combination of the last three letters, **ZZZ**, indicates the specific computation implemented. As stated by Anderson et. al. [5], the driver routines have readily available all the computational routines except matrix inversion, for this we can determine a least-squares SVD solution to the frequently cases of overdetermined systems for linear equations as previously mentioned.
The goal, as described before, is to minimize $\mathbf{m}$ for studying $||\mathbf{d} - \mathbf{Gm}||_2$. In a general situation the matrix $\mathbf{G}$ cannot be expected to have full rank but rather it will be rank-deficient as the condition $rank(\mathbf{G}) < min(M, 4N)$ is true. There are several driver routines for single precision, of special interest are $xGELSS$ and $xGELSD$ because they use the SVD method. It can be mentioned that another method, looking at the *complete orthogonal factorization*, is also possible [5]. In the work by Cleveland & Ammon [14], the driver routine $SGELSS$ (indicating real data) is the one used for the inversion procedure. Actually the $xGELSS$ is an older routine compared with the faster $xGELSD$, although unless more large problems are studied, the $xGELSS$ will be working sufficiently [5]. As the $xGELSD$ needs more workspace and necessary only with larger datasets, this is likely the reason why they decided on using the $SGELSS$ routine. Still, this can possibly be a point to bring up for question in future work when dealing with larger regions and datasets.

4.6 Defining parameters

There are several parameters that have been defined or chosen, depending on the region of interest but also on how the DD-based inversion method will be executed. The period band needs to be defined with short and long period values to filter out data that are not in this range. Analyzing this parameter has proven to affect the end results (see 6). The group velocity range parameter has been needed to define the lower and upper Rayleigh group velocity limits, used for windowing the data. It was defined by default to be from 2.5 - 5.0 km/s, ergo a relatively wide range, and therefore it has not been necessary to change this parameter. The channel parameter lets you define the channel or channels to use before cross-correlating traces. As described in section 4.1, for vertical component Rayleigh waves this is noted BHZ. An additionally parameter that has been used and defined is the horizontal slowness value (for Rayleigh waves) with unit s/km. It is dependent on regional earth structure and is described more in chapter 5 and 6. It can also be mentioned that as a precautionary step a parameter that remove measurements with very high lag times or time shifts has been in use. Though it has not been seen necessary to change the default value defined to 50 s.
Other parameters do affect the relocation of earthquakes in a more direct way. One of these parameters define the maximum linking distance for any event-pair which the validity of the method rely on (section 3.2). Cleveland & Ammon [14] found that only with inter-source distances of larger than 120 km did dispersion differences between two events significantly affect CC. They therefore defined it to 120 km

which has in this thesis been used as a reference to observe different relocation results for the northern North-Atlantic Ridge. In regards to CC, to determine the minimum acceptable CC-value to relocate events the CC-coefficient parameter is defined. Explained in section 4.4 the 0.90 value has been kept from Cleveland & Ammon [14], even though lower CC-values like 0.75 and 0.80 were tried, the best results came with defining the CC-coefficient to 0.90. In addition to these two important parameters, the relocation rest much on observations that create systematic traveltime difference patterns (section 3.2). This is achieved through defining the minimum number of common observations at stations for an event-pair to be linked as well as the minimum azimuthal range (in degrees) that the stations must span so that the events will be linked. Lastly, the double-difference observations have been weighted by distance between the two events so that if they are spaced more apart they will be down-weighted compared to other two events that are close together [14]. More specifically, there are four scenarios depending on the defined maximum linking distance. If the distance is less than or equal to $0.25 \times$ *maximum linking distance* the weight is unity. If the distance is less than or equal to $0.33 \times$ *maximum linking distance* then DD-observations are weighted by $\frac{1}{2}$. Is the distance less than or equal to $0.50 \times$ *maximum linking distance* the weighting becomes $\frac{1}{4}$. For any distances larger than these (not larger than the maximum linking distance), the weighting is $\frac{1}{8}$.

4.7 GMT

The relative relocation plotting of events is done through *the Generic Mapping Tools (GMT)* with the version used being GMT 5.2.1. GMT is an open source software and include roughly 80 command tools to analyze and manipulate data sets (both x,y data and x,y,z data) as well as commonly producing figures post script. Because it can create high quality graphical plots, GMT is now favorably used by a large part of the scientific community in need of presenting different data and geological structures available with over 30 map projections [45]. As an example, the map projection used for this master thesis is the well known Mercator projection ($-JM$), a cylindrical projection that are increasingly distorted towards the poles. From GMT 4 to GMT 5 there have been made some fundamental changes that affected the process of plotting the relocated events by the DD-based inversion method. GMT 4 has competence to grid data and making plots in individual programs linked to GMT, whereas in GMT 5 the possible executions like gridding, imaging and contouring commands is gathered into one self-contained program called **gmt** [45]. This makes it easier for the user in that GMT modules simply reads in the data specified and returns the output in a predestined place. Since the codes in *surfaceWaveRelocation_v2.6.py* written by Cleveland & Ammon assumed GMT 4 (and originally provided the relocation plot directly from the execution), it was necessary to create a GMT module made with the GMT 5 syntax to make the relocation plot. It is demonstrated in the GMT script shown in figure 4.5, written specifically for plotting the relocations in Kolbeinsey Ridge and JMFZ (section 5.1). The GMT scripts for the other two parts are the same except for a different scale and latitudinal/longitudinal limits.

```
#!/bin/csh
gmt set FONT 10p,Helvetica
gmt set PS_MEDIA 6.5ix6.5i
gmt set PROJ_LENGTH_UNIT point
gmt set MAP_FRAME_TYPE fancy
set PSFILE=Plot-Relocation.ps
set NEIC=eventInfo.txt
set SCALE=0.036315

set PROJ=-JM5i
set LIMITS=-R-18.0/-3.0/68.0/72.5
set SIZE=70
set colour=ibcao4.cpt
#gmt grdraster 7 $LIMITS -GETOPO1_Bed_g_gmt4.grd -I3Oc -V
gmt psbasemap $PROJ $LIMITS -Bpx2 -Bpy0.5 -P -Xc -Yc -K -V > $PSFILE
gmt grdimage IBCAO_V3_30arcsec_RR.grd -C$colour $PROJ $LIMITS -O -K -V >> $PSFILE
#gmt pscoast $PROJ $LIMITS -Dfull -W0.5p -Na -Gred -O -K -V >> $PSFILE
gmt grdcontour IBCAO_V3_30arcsec_RR.grd $PROJ $LIMITS -C200 -L-5000/0 -O -K >> $PSFILE   #Water
gmt grdcontour IBCAO_V3_30arcsec_RR.grd $PROJ $LIMITS -C100 -L0/3000 -O -K >> $PSFILE   #Land
#gmt pscoast $PROJ $LIMITS -Dfull -W0.5p -Na -Gred -O -K -V >> $PSFILE
gmt psscale -C$colour -Bx1000+l"Topography/Bathymetry (m)" -D6.3c/-1c/12c/0.35ch -V -O -K >> $PSFILE
sort -r -k7 $NEIC > neic.xy
awk '{print $2, $3,'$SCALE'*2*10^(($7-4.5)/2)}' $NEIC > usgs.xy
gmt psxy  $PROJ $LIMITS usgs.xy -Sc5p -Gwhite -W1p -O -K -V  >> $PSFILE
awk '{print $4, $5, '$SCALE'*2*10^(($7-4.5)/2)}' $NEIC > usgs2.xy
gmt psxy  $PROJ $LIMITS usgs2.xy -Sc5p -Gred -W1p -O -K -V  >> $PSFILE
gmt psxy  $PROJ $LIMITS black.txt -Sc5p -Ggreen -W1p -O -K -V  >> $PSFILE
gmt psxy /uio/lagringshotell/geofag/students/ceed/chrisgko/wilber6/Results/Maps/locationLines.txt $PROJ $LIMITS -W0.7p -A -O -V >> $PSFILE
ps2pdf -dColorConversionStrategy=/sRGB -dProcessColorModel=/DeviceRGB -dPDFSETTINGS=/prepress -dEPSCrop $PSFILE Plot-Relocation.pdf
```

Figure 4.5: GMT module written to plot the relocation procedure in Kolbeinsey Ridge and JMFZ. The GMT commands to pay particular attention to is *gmt psbasemap*, *gmt grdimage*, *gmt grdcontour*, *awk* and *gmt psxy*. The *awk* commands organize the data into the original locations (to the text file *usgs.xy*) and the relocations (to the text file *usgs2.xy*). Then the command *gmt psxy* plots these latitudinal and longitudinal locations on the map created by the commands *gmt psbasemap* and *gmt grdimage*.

Chapter 5

Focal mechanisms and relocation plots

Event data collected from Wilber 3 range all in magnitude from 4.8 up to 6.7, though with a majority of the events between 5.0 and 6.0 and having a time window defined from P-wave propagation. Stations with distances greater than 70° to an event is not included in the process, see figure 4.1. This is a consideration that is based partly upon having a comfortable amount and good azimuthal coverage of stations included, but also from requests of data one minute before P wave arrival and ending 60 minutes after P wave arrival. By excluding stations farther away, the waveform will also be simpler, as the seismic waves are not propagating in additional earth structure. The dates of the events range from as early as 1990 up to the first quarter of 2017. After considering the number of events gathered, duration of the execution or implementation of the module as well as regional geology between Iceland and Svalbard, the relocation has been divided into three main parts. These three parts are Iceland-Jan Mayen Ridge (also termed Kolbeinsey Ridge) together with Jan Mayen Fracture Zone, Mohns Ridge and lastly Knipovich Ridge together with parts of Spitsbergen Fracture Zone (northwest of Svalbard). The regional setting that this is referring to is seen in figure 1.2 and Midzi et. al. [33], the latter presented in figure 5.1 below.

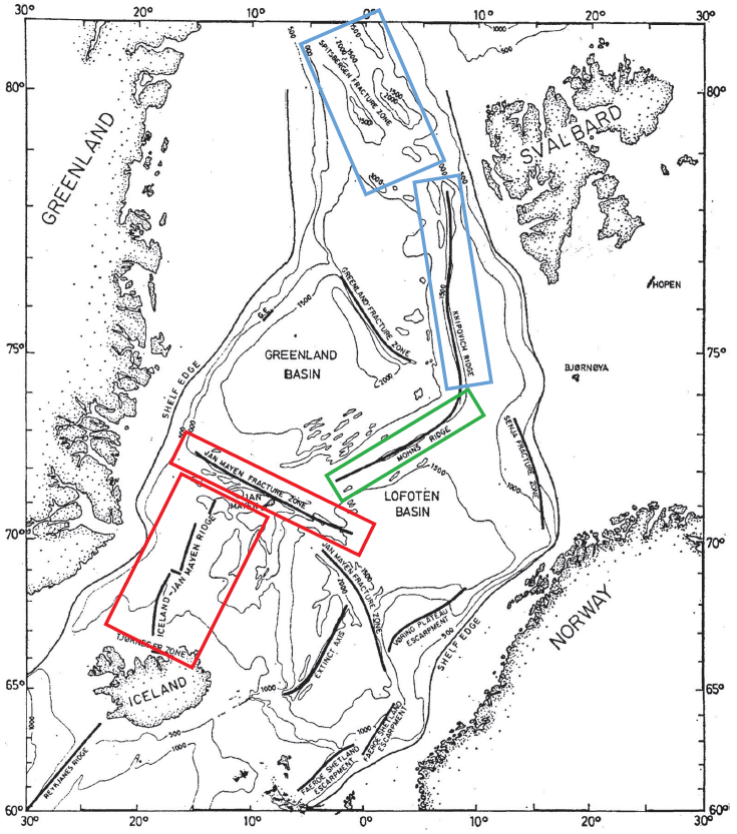

Figure 5.1: Of interest is Iceland-Jan Mayen Ridge, the part of Jan Mayen Fracture Zone (JMFZ) crossing Jan Mayen grouped together in red rectangles, Mohns Ridge in the green rectangle and Knipovich Ridge along with Spitsbergen Fracture Zone area grouped together in blue rectangles. Edited from Midzi et. al. [33].

A downside with this figure is that the North Atlantic Mid-Oceanic Ridge is not continuous because it does not connect the Iceland-Jan Mayen Ride and JMFZ nor JMFZ with Mohns Ridge. More importantly however is that the map show larger-scale structures that have the same general pattern as the associated earthquakes presented in section 1.3. An observation is the zig-zag pattern that appears to happen on Iceland-Jan Mayen Ridge moving up to JMFZ. It can also be noted that where Knipovich Ridge ends close to Svalbard, in reality continues in a more erratic pattern in a northwestern direction, as can be seen in the article by Byrkjeland et. al. [9]. As a whole this northern part of the North Atlantic Mid-Oceanic Ridge is therefore quite complex but still has relatively good determined ridge system established by research, such that comparison with the relocation solutions is possible.

5.1 Kolbeinsey Ridge and Jan Mayen Fracture Zone

In total data from 39 earthquakes around the Jan Mayen Island region have been subjected to the relocation procedure. Table A.1 contains information about the earthquakes, taken from the Wilber 3 interface. The majority of events are defined with a depth of 10.0 km and the deepest event a depth of 16.4 km. Also, magnitudes lie between M_w5.0 and M_w6.7, though some are registered with magnitude scale m_b. Both catalogs NEIC PDE and ISC have been used to gather the SAC - files, this goes for the two other defined parts of the northern North Atlantic region as well, i.e. Mohns Ridge and Knipovich Ridge/Spitsbergen Fracture Zone. The focal mechanism of 37 earthquakes from the Global CMT catalog search [6] are plotted in figure 5.2. Two of the earthquakes from the CMT catalog have not been included in Wilber 3 and at the same time there are 4 earthquakes in the data collection that are missing from the CMT catalog.
The preferred relocations can be seen under in figure 5.3. In the relocation map there are three earthquakes which have kept their original location, namely the earthquakes dated 01.07.1999 02:06:58 UTC with depth 10.0 km and M_w5.5, 15.01.2008 06:35:14 UTC with depth 10.0 km and M_w5.0 and lastly 30.08.2012 13:51:05 UTC with depth 16.4 km and m_b5.2 (see also table A.1). With exception of the last earthquake mentioned, none of these events are not the same as the ones missing from the CMT catalog. Because event data are collected both from the ISC and NEIC PDE catalogs whereas the CMT catalog lack earthquakes only registered with the ISC catalog, it may explain why there are some irregularities with the number of earthquakes. However, why there are two earthquakes in the CMT catalog that are not listed by Wilber 3 is difficult to say. The discrepancies between the two collections are summarized in table 5.1.

Table 5.1: Difference in events for Kolbeinsey Ridge/JMFZ

CMT catalog	**ISC and NEIC PDE catalogs**
-	2001-08-01 09:20:08 UTC 10.0 km mb5.0
-	1998-03-23 20:19:27 UTC 10.0 km mb5.2
-	2008-09-29 19:20:22 UTC 10.0 km mb5.0
-	2012-08-30 13:51:05 UTC 16.4 km mb 5.2
1998-12-16 09:28:37 UTC 15 km Mw5.1	-
2015-09-01 13:26:29 UTC 12 km Mw5.0	-

The remaining 35 events (out of 39) not listed in table 5.1 with the ISC or NEIC PDE catalog are plotted with their focal mechanism, thus permitting to an extent comparison between the focal mechanism plot and the events from Wilber 3. Despite having irregularities, a further look at the focal mechanisms can also give insight and possibly explaining why some events are not relocated or relocated "out of sync" with the rest. The map in figure 5.2 seem to correspond well to the regional description made in section 1.3 as we can see for the most part strike-slip and normal faulting.

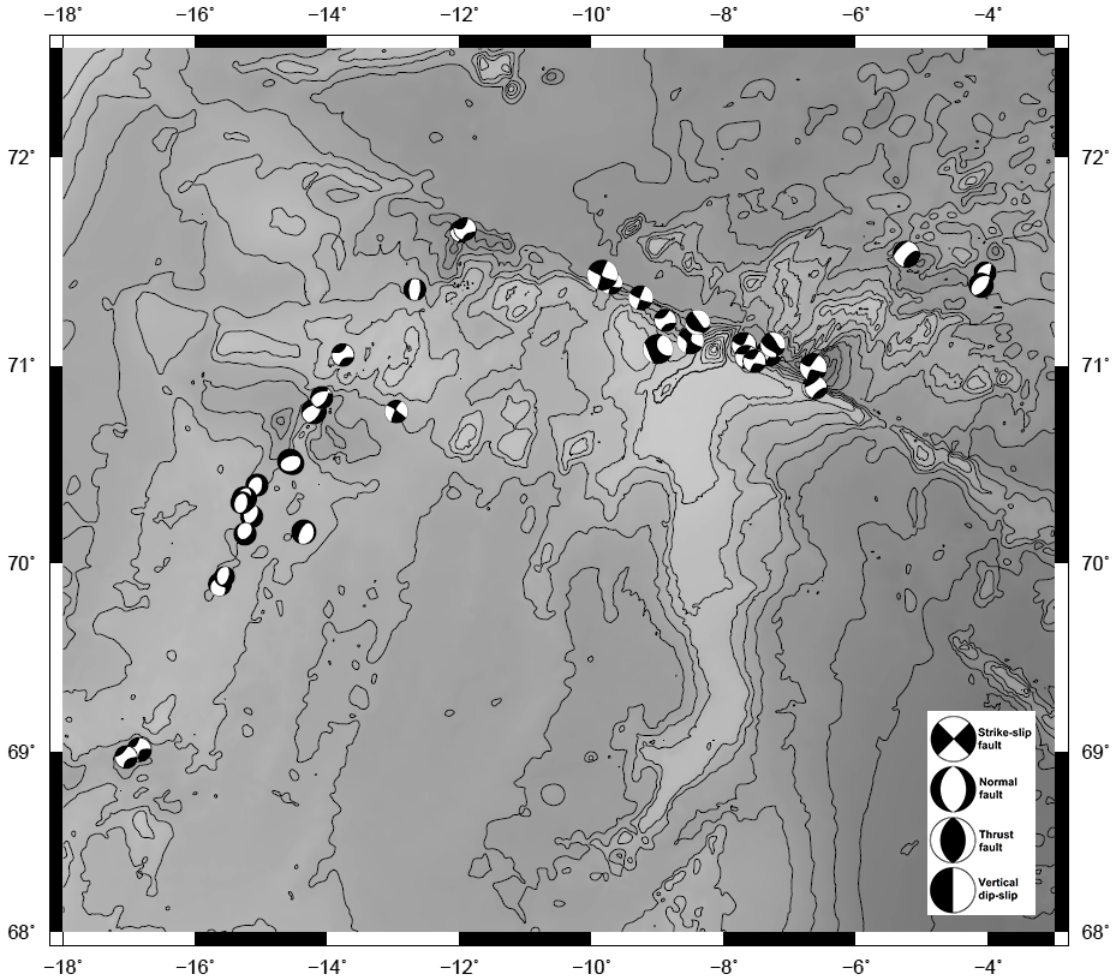

Figure 5.2: Map over 37 earthquakes at Kolbeinsey Ridge and JMFZ, showing focal mechanisms with the "beach ball" appearance as described in section 2.3. Collected with the Global CMT catalog search [6].

A few central differences in information between the CMT catalog data and the earthquakes collected with the NEIC PDE and ISC catalogs are worth pointing out. Closer look between the two figures 5.2 and 5.3 make it clear that the events are not necessarily located at the exact same latitude and longitude degrees. This can be related to the two data collections having slightly different origin time for the same earthquakes. Another point is that the origin depth for an earthquake do not match in every case. For example, the earthquake 2005-11-12 17:01:35 UTC (table A.1) is defined with a depth of 10.0 km whereas with the Global CMT catalog search the same earthquake is defined with a depth of 17.2 km. Likewise for the earthquake 2012-07-15 13:02:43 UTC it has been defined with depth 24.6 km in the CMT catalog yet with the ISC catalog the depth has been put as 11.1 km. These are two of the more extreme examples, though other instances also exist with smaller differences in depth. Several of the 39 earthquakes collected are described with a 10.0 km depth (similar situation for earthquakes at Mohns Ridge and Knipovich Ridge/SFZ). A likely reason for this is not that so many earthquakes originate from 10.0 km down but rather that it has been decided on this value (from ISC or NEIC PDE) when there have been some uncertainty with determining exact depths. In fact, none of the earthquakes in the CMT catalog within the same latitude and longitude limits are defined with 10.0 km depths. Consequently, making implications from relocations or lack of relocations are not based too much on the depths in this thesis.

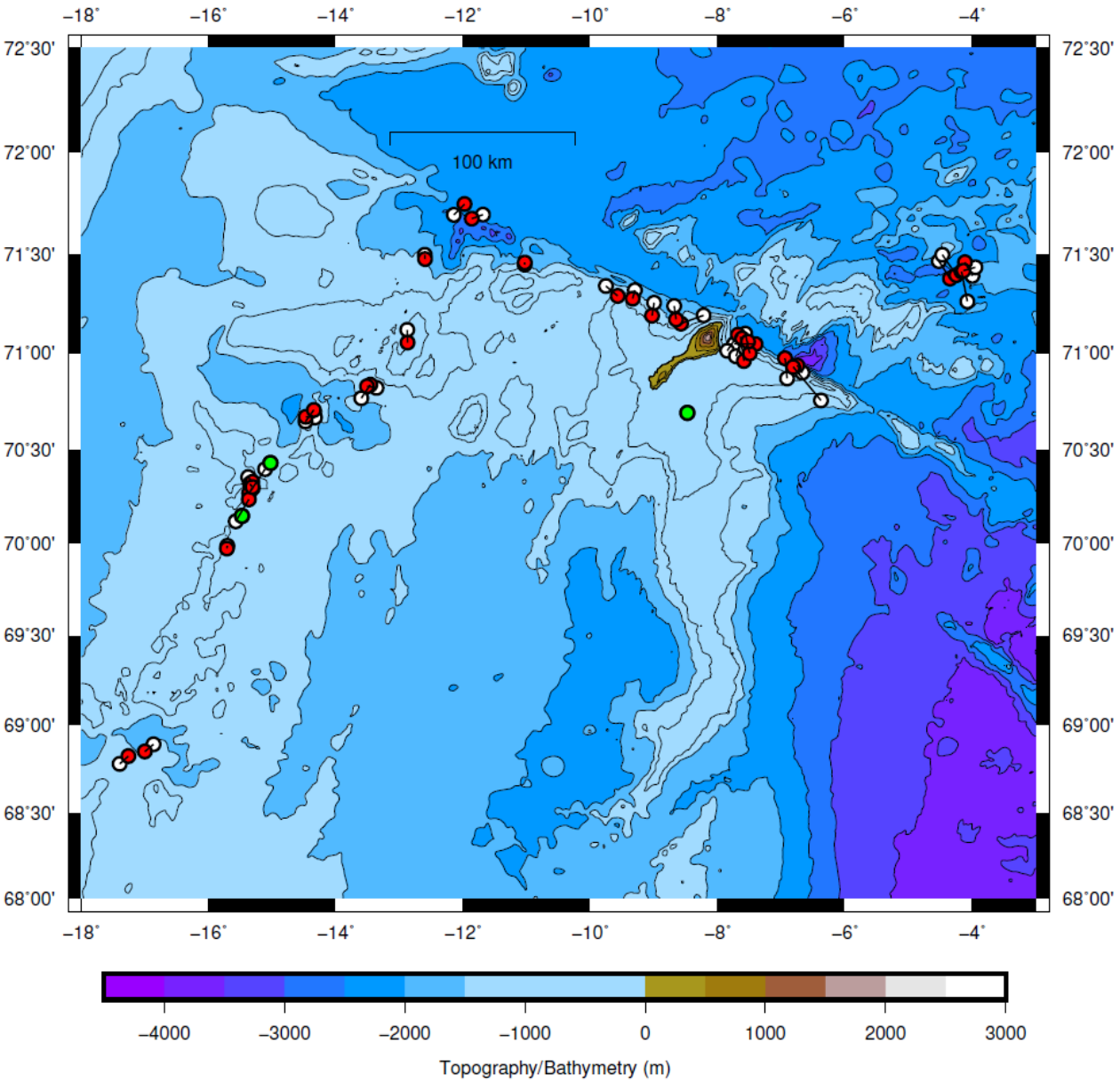

Figure 5.3: Red circles represent the relocated epicentroids by using Rayleigh waves while the white circles represent the original event locations. The old and new locations linked together with black lines indicate the amount of change in distance. The three green circles are original events that have not been moved. The small island with a brownish color is Jan Mayen.

The two earthquakes not relocated (01.07.1999 02:06:58 UTC and 15.01.2008 06:35:14 UTC) that still are plotted in figure 5.2 do not seem to have a focal mechanism solution much different from the other events surrounding that do have been relocated. Their magnitude sizes do not deviate from the rest of the events either. To get a better grasp of why the three earthquakes have been omitted from the relocation procedure, analyzing the CC-plots will be helpful (subsection 6.3.1).
To achieve the relocation several parameters have been specified. The most central ones are the maximum linking distance, the minimum acceptable CC - coefficient, the minimum number of stations with observations that pass the CC coefficient criteria as well as defining the average Rayleigh-wave slowness. Although not directly part of the DD-based inversion, setting the period range with short period and long period is part of the seismic processing prior to calculating the cross-correlations. Much of the same argument done by Clevenland & Ammon [14] for their the relocation solution, this relocation is chosen to a large extent because it minimizes the difference in location between the old and new events. Still, it has been considered that the relocations are dependent on geological region, number of events and

how they are (or not) clustered together. Parameter values chosen here are maximum linking distance with 80.0 km, the minimum acceptable CC - coefficient to 0.90 and the minimum number of links to 12. Based on the paper by Christensen et. al. [10] and partly Midzi et. al. [33] the Rayleigh-wave horizontal slowness value was chosen to 0.26 s/km derived from a 3.85 km/s speed. The period range is defined from 20 s to 80 s, quite similar to the period range of 30 - 80 s decided by Cleveland & Ammon [14]. An exaggerated period range of 15 -100 s results in 8 unlinked events and more random relocation of original events. Further, another period range with the same parameters from 15 - 60 s results in 6 unlinked events. The preferred period range is therefore based on not having too many unlinked events yet not linking events that potentially could relocate events to suspicious locations. Cleveland & Ammon [14] discovered from conducting sensitivity tests that with shorter periods, inter-event dispersion can play a substantial role in the relocation.
The period range of 15 - 100 s roughly corresponds to horizontal wavelengths on the scale of 50 - 400 km whereas the preferred period range 20 - 80 s roughly correspond to horizontal wavelengths of 80 km - 300 km.
Since there are three events that have not been relocated, a total number of 36 events are relocated. Instead of using three iterations as the default, it was necessary with four iterations to let the distance moved for all events go to 0.0. From the third to the forth iteration most of the events were not moved and those that moved, all moved 0.5 km or less. At the northeast corner of the map earthquakes around Mohns Ridge are included to extend into the next part. As noted in subsection **??** there are roughly 80 stations (table D.1) that have registered the earthquakes. This number is approximately cut in half or have available even fewer stations for earthquakes before 1995. Despite this reduction for older earthquakes, the azimuthal distribution of stations appear to be relatively good with stations on both sides of the Atlantic Ocean. The same can be said for the datasets at Mohns Ridge and Knipovich Ridge/Jan Mayen Fracture Zone.
The DD - inversion procedure resulted in a mean absolute misfit from initial 2.77 s to final 0.30 s, see figure 5.4.

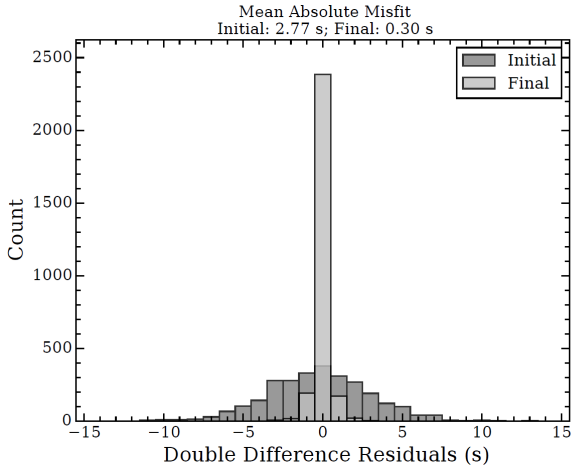

Figure 5.4: Histogram over the initial and final misfits of 36 earthquakes in the Jan Mayen Island Region. The initial fit is calculated from the original NEIC PDE and ISC catalog locations and times.

This histogram shows that the number of final DD - residuals is close to 2500 and fit all in the single column centered on the 0 s mark, thereby supporting a high precision of the relative relocated epicentroids. It demonstrates that the predicted or calculated DD for each step moves closer to the observed DD based on equation 3.5, until it reaches the calculation limit. The distances between the original earthquake locations and the relocated epicentroids goes from about 0.2 km to 25 km and the median is found to be 7.49 km (figure 5.5).

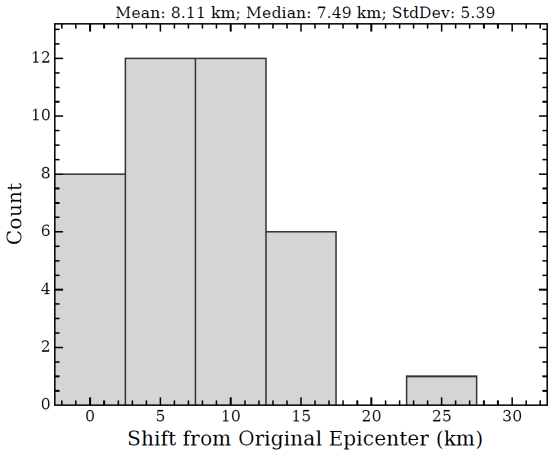

Figure 5.5: Distribution of distance shift between relocated epicentroids and the original epicenter locations. The vertical axis shows the number of earthquakes.

Moreover, the mean and standard deviation of distance shift have been calculated to be respectively 8.11 km and 5.39 km. The results also include a graph over the distribution shift of the origin time between relocated events and original locations with a mean of 0.89 s and median 0.73 s (figure 5.6).

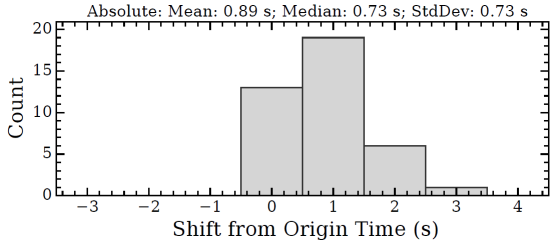

Figure 5.6: Distribution of origin time shift between relocated epicentroids and the original epicenter locations. The vertical axis shows the number of earthquakes.

The standard deviation have been calculated to 0.73 s as seen in figure 5.6. A quick look at the relocation map show that new locations are in general more clustered together, for example with the two southernmost earthquakes as well as the earthquakes that belongs to Mohns Ridge. Additionally the events at JMFZ appear to form more of an even line compared to the original epicenter locations. This, along with that no events stands out by being moved large distances, presents the solution as relatively realistic, i.e. the events are placed to a larger degree in relations to the fracture zones and ridge system. To test the parameters resulting in relocations presented in figure 5.3, another execution is done with different parameters. Figure 5.7 is constructed with a maximum linking distance of 120 km, minimum CC - coefficient of 0.75 and minimum number of observations put to 6.

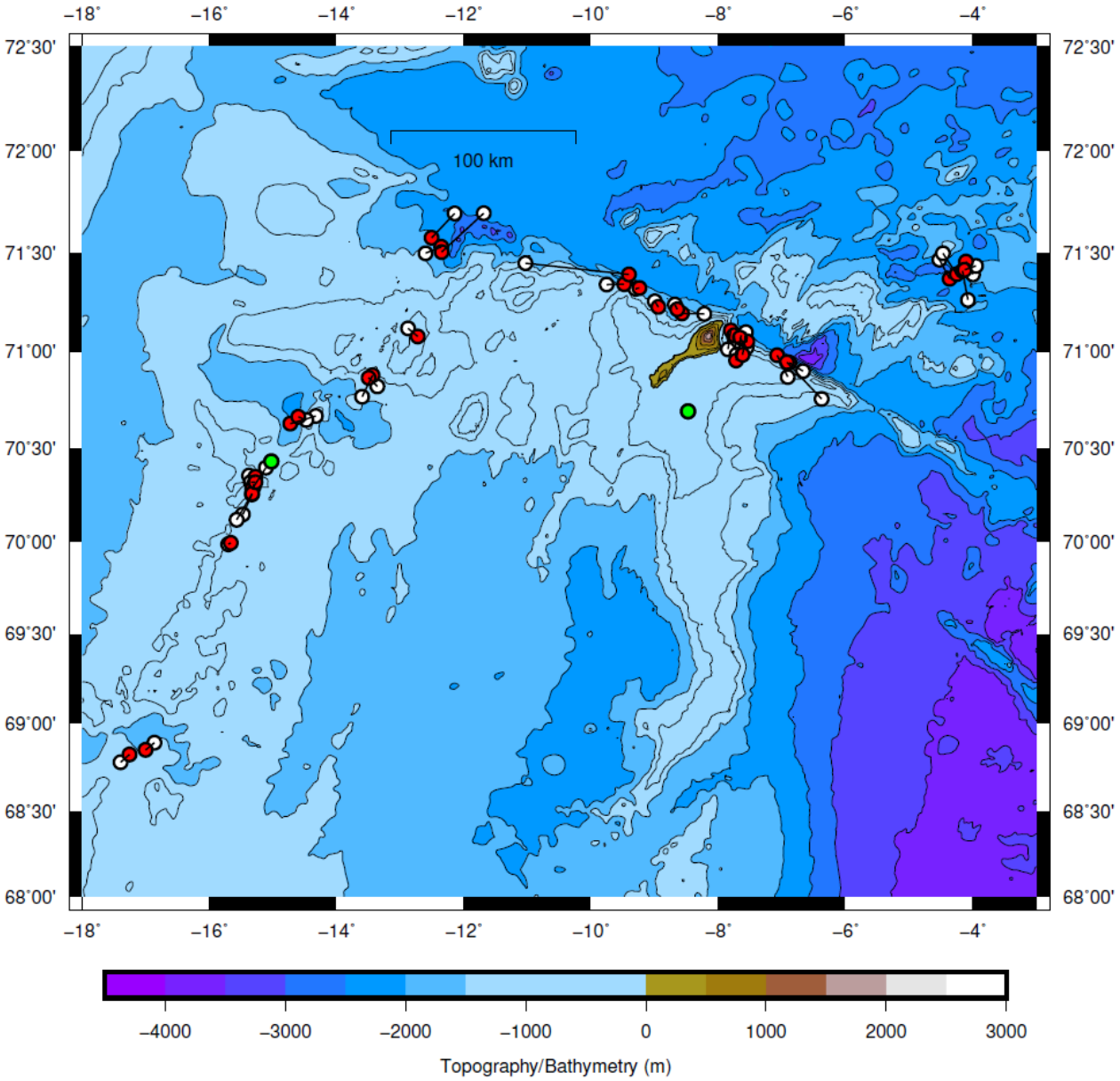

Figure 5.7: A change in parameters in the relocation method change the relocations of the earthquakes at Kolbeinsey Ridge and JMFZ. Instead of three original earthquakes not included in the method like in figure 5.3 there are only two as indicated by the green circles. In total there are therefore 37 earthquakes that are relocated.

A substantial difference between the two scenarios is the longest distance moved, having an epicentroid changing position to about 60 km from the original epicenter location. In this execution one event in the preferred solution not relocated, has now passed the new requirements and therefore been relocated. Figure 5.7 shows that there are two "green" earthquakes that have kept their original epicenter location. Because the depth and magnitude of the three unlinked events (in the preferred solution) are quite similar, it do not provide any indication to why this single event now has been included in the relocation process. The earthquake plot in figure 5.2 for the two events not relocated have similar focal mechanisms as the surrounding earthquakes and so do not either give further understanding to why they have not been subjected to the DD - inversion method. Another execution identical to the second one, except having the minimum number of links changed to 12, reveal that the cause is largely connected to the low CC-coefficient. The mean and median in the second execution have changed accordingly to respectively 11.33 km and 9.41 km as seen in figure 5.8. Most of the earthquakes have been relocated at the same location or close to the same location as in the preferred solution. Though the three earthquakes that lies between $12°W$ and $10°W$ stands out and deviates significantly. In this relocation they

effectively create a larger gap where no earthquake seismicity is occuring. The two most northern events are also moving away from the JMFZ- zone and instead towards Kolbeinsey Ridge. Overlooking the map in figure 5.7 it is suspicious that the event which is relocated furthest should be moved so drastically, implying that the original epicenter location is quite inaccurate. As such the solution in figure 5.3 look better compared with the solution seen in figure 5.7.

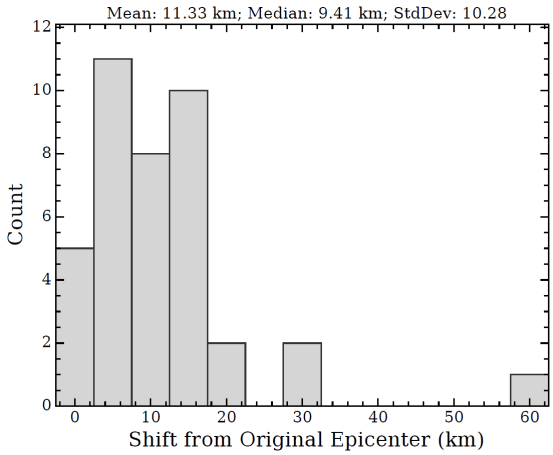

Figure 5.8: Same as figure 5.5, only with different parameters that shows an effect on the distribution of distance shift between relocated epicentroids and the original epicenter locations. One earthquake has been shifted roughly 60 km. Make note that the largest distance shift in the two runs are not coming the same earthquake.

The changes to the results with the second execution gives an initial mean absolute misfit of 3.75 s and a final mean absolute misfit of 0.44 s. Calculating the difference in final misfits shows that the preferred execution is 0.14 s lower to the DD observational time shift from an initial misfit of 2.77 s compared with 3.75 s (figure 5.9).

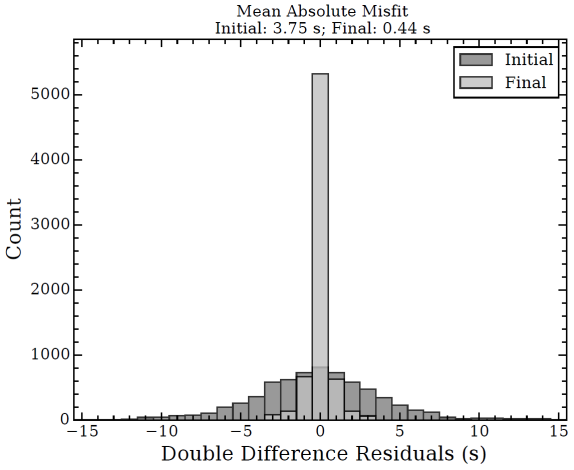

Figure 5.9: Same as figure 5.4, yet with a higher initial and final misfit as the parameters were defined differently.

An important note regarding the results of distance shifts, origin time shifts as well as the absolute misfits is that the numbers do not directly provide evidence of whether the relocations are true or not, even though it can help with discussing if it is realistic and how precise and accurate the new locations are.

5.2 Mohns Ridge

This includes the largest dataset gathered with 62 earthquakes along Mohns Ridge to be subjected to the DD - based inversion (table B.1). The parameters defined are relatively similar to the ones for Kolbeinsey Ridge and JMFZ. Rayleigh-wave slowness is put as 0.26 s/km and the CC-coefficient with value 0.90. The deepest earthquake is registered at 17.0 km down and the shallowest earthquake at 0.0 km (both with the ISC catalog). As mentioned in section 5.1 there are likely to be some uncertainty with the depth values, it is made clear by using the shallowest earthquakes as an example. To have an earthquake being generated at the ocean level is an unlikely scenario at the Mid-Atlantic Ridge system. In the CMT catalog the same earthquake has a depth of 12 km which again demonstrate the uncertainties with confidently being able to make implications from earthquake depths. However, Mohns Ridge appear to have relatively constrained earthquake depths as listed in table B.1 and examined from the CMT catalog. In the latter all earthquakes are defined with depths that range from 12.0 km to 16.8 km. Plotted below are focal mechanisms for 64 earthquakes collected with the Global CMT catalog (5.10). Several events collected with the ISC and NEIC PDE catalogs are missing from the CMT catalog, similar as is experienced with events from Kolbeinsey Ridge/JMFZ. Table 5.2 lists all earthquakes that are missing their focal mechanism solution. The earthquakes plotted with their focal mechanism that are missing in the dataset used for relocation is however not listed.

Table 5.2: Events with missing focal mechanisms at Mohns Ridge

ISC and NEIC PDE catalogs	**CMT catalog**
1995-07-15 10:54:18 UTC 10.0 km mb5.4	-
1995-09-20 06:53:43 UTC 10.0 km mb4.8	-
1997-10-06 21:13:10 UTC 10.0 km mb5.0	-
1998-01-17 23:52:59 UTC 10.0 km mb4.8	-
1998-01-18 02:53:32 UTC 10.0 km mb4.8	-
1998-03-23 20:19:27 UTC 10.0 km mb5.2	-
2000-02-15 18:37:20 UTC 10.0 km mb4.9	-
2000-09-02 06:58:13 UTC 10.0 km mb4.8	-
2001-11-08 02:00:05 UTC 10.0 km mb4.9	-
2002-02-09 21:48:04 UTC 10.0 km mb4.8	-
2002-04-08 03:55:37 UTC 10.0 km mb4.8	-
2002-07-10 14:13:11 UTC 10.0 km mb4.9	-
2002-10-12 03:46:47 UTC 10.0 km mb4.8	-
2003-01-09 19:29:23 UTC 10.0 km mb4.8	-
2006-01-29 19:49:46 UTC 10.0 km mb4.8	-
2008-09-29 19:20:22 UTC 10.0 km mb5.0	-
2010-04-06 23:50:23 UTC 17.0 km mb5.3	-
2012-05-25 00:25:55 UTC 12.2 km mb5.0	-
2017-03-10 16:41:12 UTC 10.0 km mb5.0	-

The earthquakes collected with Wilber 3 include magnitudes ranging from the smallest of $M_w 4.8/m_b 4.8$ to the largest of $M_w 6.3$. Still the majority of events selected have magnitude of 5.0 or larger. Not all earthquakes with the smallest magnitudes below 5.0 have been downloaded and the focal mechanism map in figure 5.10 consists of several earthquakes with magnitude 4.8 or 4.9 that are excluded from the relative relocation procedure. In total there are today approximately 90 events (using Wilber 3) within the latitude/longitude boundaries giving 30 events not downloaded that have magnitude 4.8 or 4.9. These events are omitted because the focus has been on earthquakes with magnitude at 5.0 or larger. The specific and preferred solution for relocations at Mohns Ridge is executed with maximum linking distance of 120 km and minimum number of stations to 8. This region proves to be more complex as it is necessary with 5 iterations to let the distance moved for events converge towards 0.0. In figure 5.11 a total of 57 events are relocated which makes a total of 5 events not moving from their original location. Table 5.3 lists these earthquakes. Even though three out of the 5 earthquakes are missing their focal mechanism, it is clear from figure 5.10 that the fault geometries are quite homogeneous, as is also supported by the description in section 1.3. That these earthquakes would have widely different fault

geometry is therefore not likely, but it should not be ruled out that it may be some of the explanation for them not being relocated.

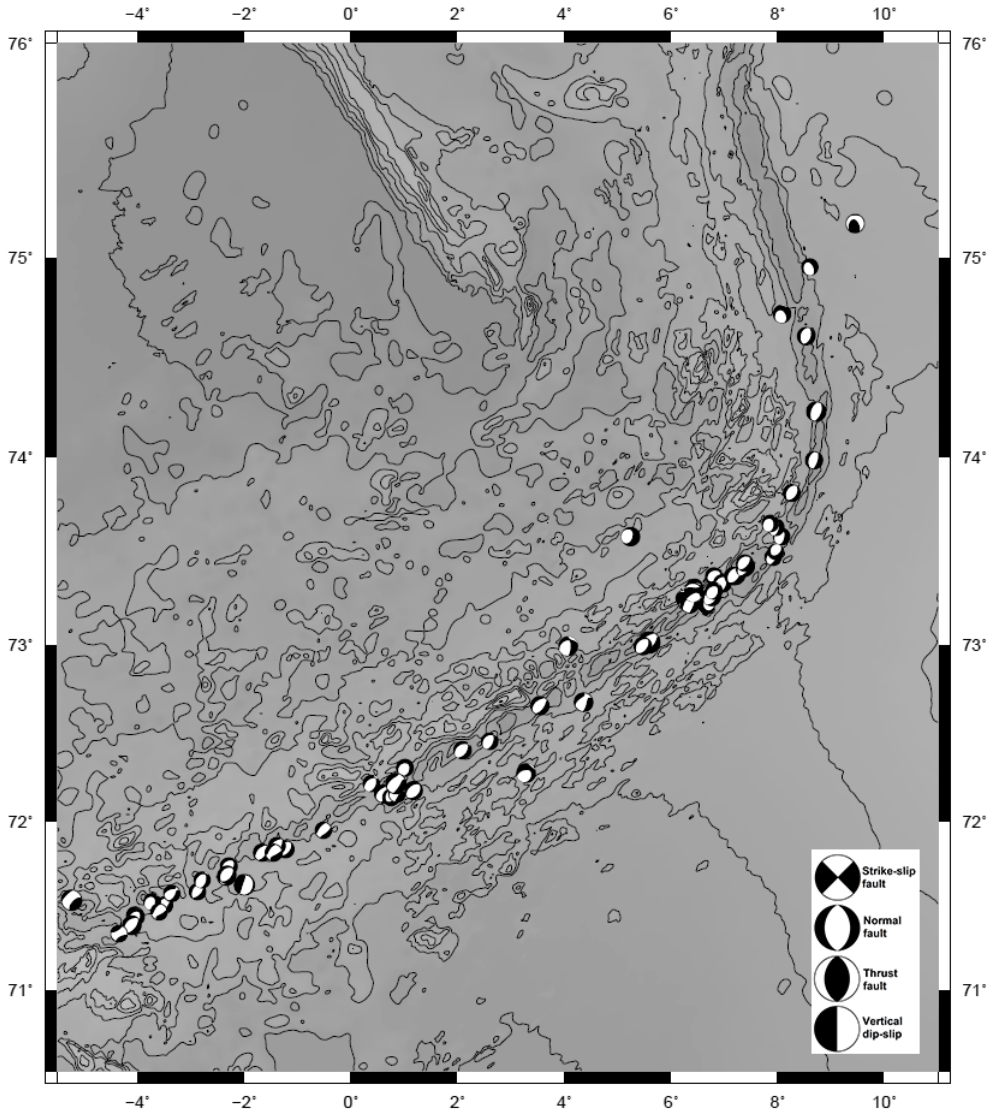

Figure 5.10: Map over 64 earthquakes at Mohns Ridge, showing focal mechanisms with the "beach ball" appearance as described in section 2.3. Collected with the Global CMT catalog search [6].

Table 5.3: Unlinked earthquakes at Mohns Ridge

75.249 N	10.249 E	2000-02-03 15:53:13 UTC	10.0 km	Mw5.5	Svalbard Region
72.712 N	5.005 E	2000-02-15 18:37:20 UTC	10.0 km	mb4.9	Norwegian Sea
72.579 N	3.697 E	2000-09-02 06:58:13 UTC	10.0 km	mb4.8	Norwegian Sea
72.1609 N	1.0954 E	2006-11-02 22:48:10 UTC	10.0 km	MW5.0	Norwegian Sea
73.4399 N	7.2253 E	2010-04-06 23:50:23 UTC	17.0 km	mb5.3	Greenland Sea

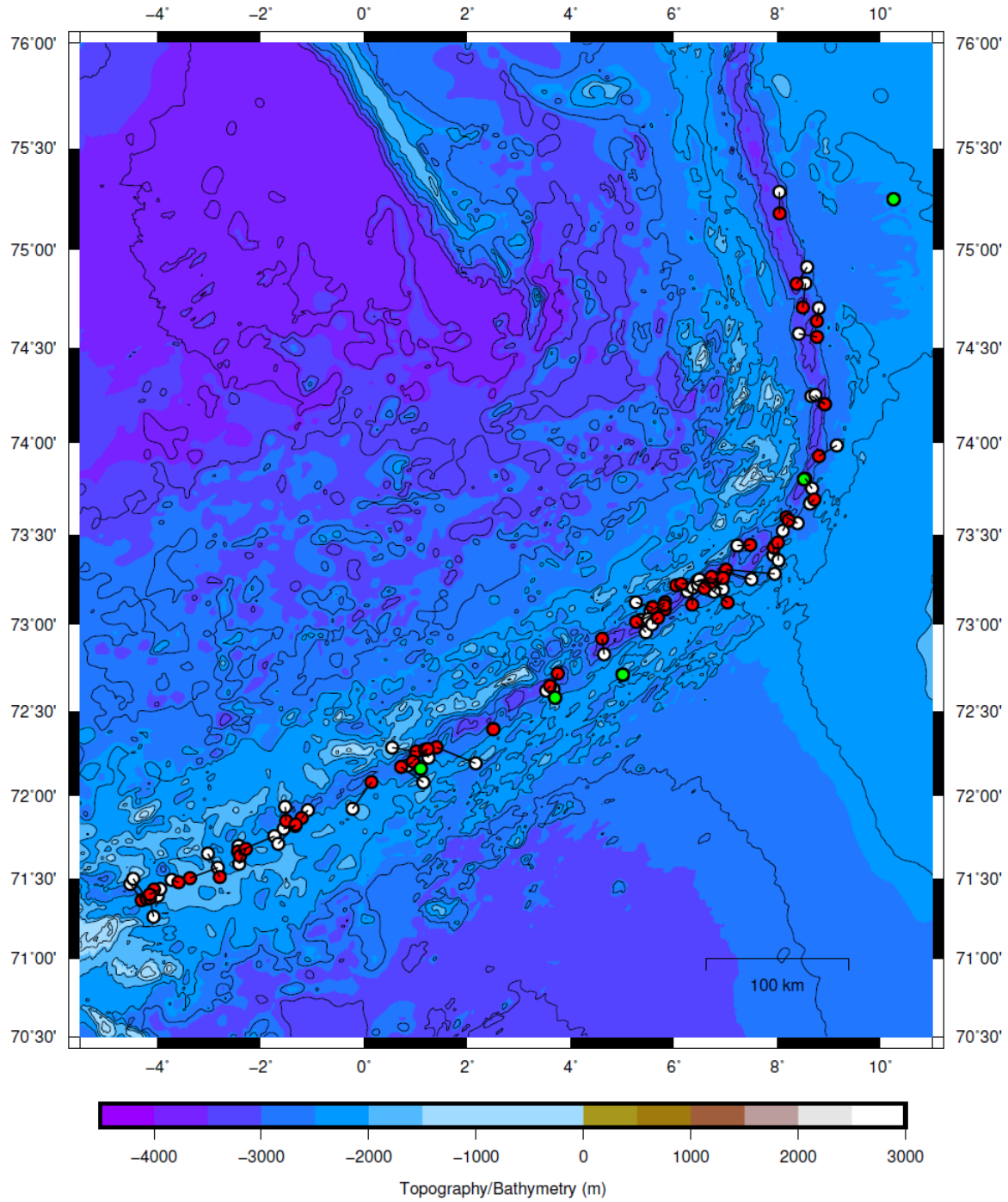

Figure 5.11: Map over 62 earthquakes around Mohns Ridge used in the relocation method. Red circles represent the relocated epicentroids by using Rayleigh waves while the white circles represent the original event locations. The old and new locations are linked together with black lines indicate the amount of change in distance. The 5 green circles are original events that have not been included in the relocation procedure.

After some trial and errors with finding preferred relocations, a period range of 30 - 90 was decided upon. It corresponds approximately to horizontal wavelengths from 100 - 340 km. Marginal differences is found with period range of 25 - 80 s and another with 25 -100 s, though not necessarily better. For example in the execution with the period range of 25 - 100 s the final misfits are identical, the mean slightly larger (12.35 km) and median just a bit smaller (10.03 km). The results with final period range of 30 - 90 s are given under.
For Mohns Ridge the DD - inversion procedure resulted in a mean absolute misfit with an initial misfit

of 4.60 s and final misfit 0.25 s (figure 5.12).

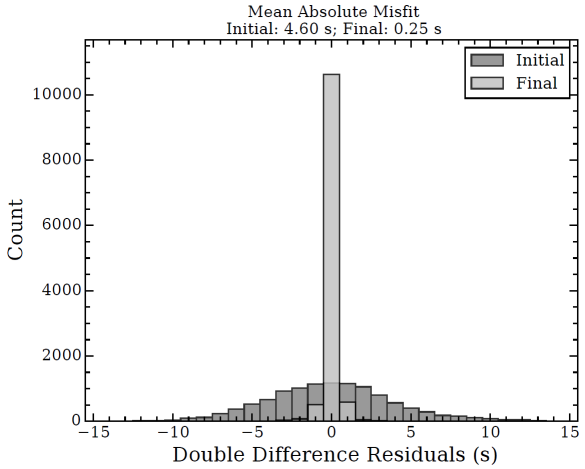

Figure 5.12: Histogram over the initial and final misfits of 57 earthquakes around Mohns Ridge. The initial misfit is calculated from the original NEIC PDE and ISC catalog locations and times.

The median shift from original epicenter is 9.67 km, the mean is 10.69 km and the standard deviation is 6.87, see figure 5.13 under.

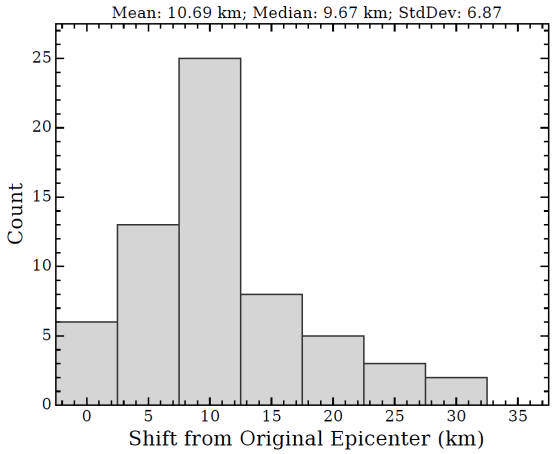

Figure 5.13: Distribution of distance shift between relocated epicentroids and the original epicenter locations at Mohns Ridge. The mean, median and standard deviation have been calculated for analysis.

Overall there are a few earthquakes that have been shifted larger distances than in Kolbeinsey Ridge/JMFZ, still it shows the same trend of most being moved about 10 km and then fewer and fewer earthquakes have increased their distance from the original epicenter as we go right on the horizontal axis. The relocated epicentroids are generally more clustered together compared with the epicenters, for example as seen for earthquakes that lie in vicinity of the 0-2 ° W/E column. No relocated earthquake stand out to have been moved in a particular suspicious direction and as a consequence there is here more of an even line of event locations resulting from the inversion method. The earthquakes that do not have been relocated are all close or fairly close to the other earthquakes, with the exception of the northernmost "green" earthquake seen between 75° 00′ N and 75° 30′ N (figure 5.11). Further, the earthquake information given in table 5.3 are relatively alike with the relocated earthquakes in terms of depth and magnitude. This information do not give any strong indications to why these 5 earthquakes are not relocated. The focal mechanism for the southernmost "green" earthquake do not appear to be significantly different from the rest (figure 5.10), yet for the single outlier event to the north the focal mechanism is somewhat different, displaying mainly a thrust fault geometry. Having three other events not relocated and at the same time with undetermined focal mechanisms it cannot be ruled out that a difference in fault geometry is the underlying cause for being omitted from the relocation process. By

studying the CC-plots in chapter 6 it is possible get a better understanding of why also the three other earthquakes out of the 5 are not relocated.

5.3 Knipovich Ridge and Spitsbergen Fracture Zone

To limit this part of the northern North Atlantic Ridge, i.e. making the relocation maps more readable, it has been divided into two sectors or areas. It has also been divided in a practically sense for researching purposes as it is two separate areas that accommodate different geophysical processes. The first section is determined to include the part of Knipovich Ridge that continues from Mohns Ridge and ends up at approximately 79° latitude. The second sector continues further north and more in a western longitude direction that is termed the Spitsbergen Fracture Zone (SFZ). Combined the two sectors lists 77 distinctive earthquakes downloaded from Wilber 3 (see table C.1), 41 at Knipovich Ridge and 37 at SFZ. Adding up the numbers from each area makes the total to 78 earthquakes, the reason being one earthquake (1992-07-20 07:46:47 UTC) is used in the relocation execution for both structures. As explained in section 5.2 there may be some earthquakes that have been omitted in the dataset, though nearly all earthquakes within the latitude and longitude limits are included. Most of the earthquakes here are defined with magnitudes between 5.0 and 6.0. The smallest earthquakes have a defined magnitude of M_w4.8/m_b4.8 and the largest with a M_w6.6 - magnitude. Also, more of the earthquakes have been characterized with higher depths compared to those at Kolbeinsey Ridge/JMFZ and Mohns Ridge. For example, there are three earthquakes defined below 25 km whereas there are none at these depths neither at Kolbeinsey Ridge/JMFZ nor Mohns Ridge. The shallowest earthquake has been determined to 3.2 km and the majority of earthquakes are simply put to 10.0 km. The depth span can be said to be considerable larger even though some skepticism must be taken with these values. As stated in section 5.1 the possibility should be kept open that many of the depth values could have been defined from a calculated guess because the exact depth cannot be accurately determined. Figure 5.14 show focal mechanisms plotted with the Global CMT catalog. Events in the dataset missing their focal mechanism are listed in table 5.4.
At Knipovich Ridge and SFZ there is a general tendency of greater separation of earthquakes as well as less clustering compared to the other two parts of the region between Iceland and Svalbard. Such features have lead to more uncertainty deciding on a set of parameters as well as doubts about how the relocated earthquake should be moved. Especially from the end of Knipovich Ridge continuing north there are not enough earthquakes with a decisive pattern to give confident solutions like for Kolbeinsey Ridge/JMFZ and Mohns Ridge shown in sections 5.1 and 5.2. Still, preferred relocations for the two sections are shown in the relocations map in figure 5.15. For both 4 iterations were necessary for letting the moved distance be 0.0 or equivalently so small it has not been picked up by the relocation algorithm. Table 5.5 lists the 17 earthquakes that have stayed in their original position. This is a considerable higher amount compared to the findings in section 5.1 with 3 unlinked events and section5.2 with 5 unlinked events.

Table 5.4: Events with missing focal mechanisms at Kniponich Ridge and SFZ

ISC and NEIC PDE catalogs	**CMT catalog**
1991-03-18 14:26:02 UTC 10.0 km mb4.8	-
1995-05-13 22:38:47 UTC 10.0 km mb4.8	-
1995-06-05 04:40:21 UTC 33.0 km mb5.2	-
1997-02-06 14:41:51 UTC 10.0 km mb5.3	-
2001-02-04 06:55:53 UTC 10.0 km mb4.8	-
2002-02-09 21:48:04 UTC 10.0 km mb4.8	-
2002-05-27 06:58:48 UTC 12.0 km mb4.8	-
2003-01-09 19:29:23 UTC 10.0 km mb4.8	-
2004-07-21 11:25:42 UTC 10.0 km mb4.8	-
2010-10-02 21:26:02 UTC 16.2 km mb4.9	-
1991-06-09 10:57:06 UTC 10.0 km mb4.9	-
1993-04-24 10:38:30 UTC 10.0 km mb4.9	-
1994-11-10 08:45:57 UTC 10.0 km mb5.3	-
2012-10-29 14:54:53 UTC 10.0 km mb4.9	-

Again the different information given with the Global CMT catalog search compared to the event dataset provided by IRIS should be stressed. The earthquake labeled 1991-09-01 06:51:04 UTC in table C.1) is defined with a depth of 10.0 km while the same earthquake in the CMT catalog has a depth of 34.9 km, a difference of 24.9 km. Another event at 1992-09-09 13:08:54 UTC has with the ISC catalog a depth of 24.0 km though for the same event with the CMT catalog is described with a 15.0 km depth. Just as with the events for Kolbeinsey Ridge/JMFZ and Mohns Ridge it creates doubt and limits making conclusions for relocation solutions. Further, the magnitude sizes do not necessarily match up perfectly either. The event 1993-09-23 20:04:01 UTC in the dataset downloaded has a magnitude of m_b4.9 whereas it is defined with m_b4.7 in the CMT catalog. This is one example of a 0.2 (absolute) difference in magnitude, usually there is only a 0.1 difference or no difference at all. Despite small differences in locations, origin time, depth or magnitude between catalogs, the earthquake description from IRIS is the basis for any discussion regarding the methods or results.

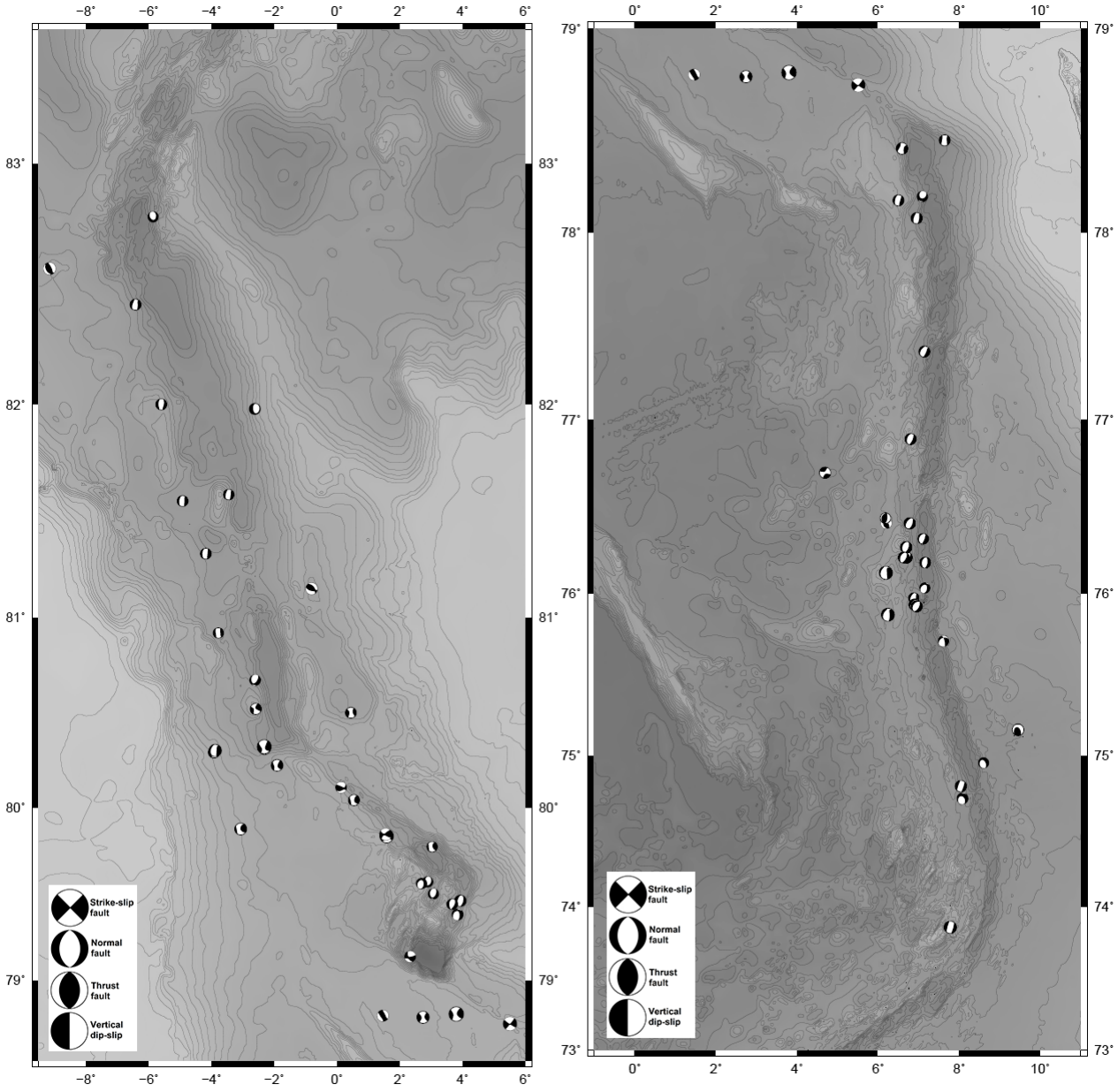

Figure 5.14: Maps over 32 earthquakes at Knipovich Ridge (right map) and 36 earthquakes at SFZ (left map), both sections displaying focal mechanisms as the "beach balls" described in section 2.3. Collected with the Global CMT catalog search [6].

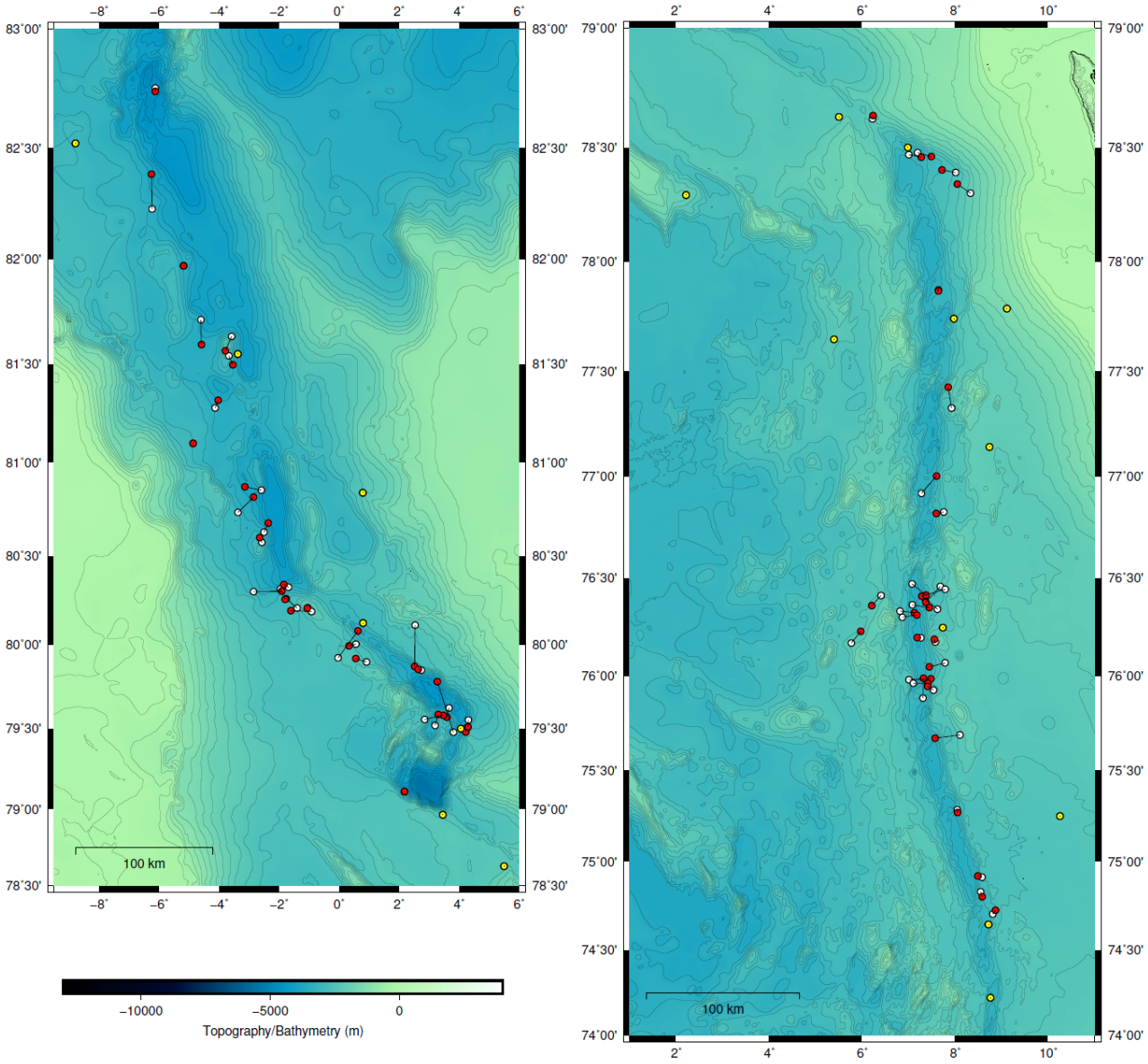

Figure 5.15: Two maps over 78 earthquakes around Knipovich Ridge and SFZ used in the relocation method. The one on the right show relocations around Knipovich Ridge and the left map relocations at SFZ. Red circles represent the relocated epicentroids by using Rayleigh waves while the white circles represent the original event locations. The old and new locations are linked together with black lines indicate the amount of change in distance. The 18 yellow circles are original events that have not been included in the relocation procedure.

At Knipovich Ridge the events that have been relocated produce a pattern of earthquakes more assembled or moving towards each other. This can be seen in particular between 75° 30′ N and 76° 30′ N at the map to the right (figure 5.15). Another observation for relocated events in the vicinity of 78° 30′ N, close to *Forlandet National Park* that is seen on the same map between 78° 30′ N and 79° 00′ N, is that they appear to be moved in direction away from Svalbard. Instead the events are gathered together what is likely more the center of Knipovich Ridge. Earthquake clustering is also visible to an extent at SFZ at the left map (figure 5.15), for example within 80° 00′ N and 80° 30′ N where relocated events create almost a straight line. From 80° 00′ N to more northern latitudes the lack of events with considerable distance between them affirm the difficulty in describing the accuracy of the DD-inversion method. Even though many more earthquakes are unrelocated at Knipovich Ridge/SFZ, the solutions can be said to be relatively robust for the earthquakes that have been relocated, not shifting over larger distances or in particularly suspicious directions. This description fits well for Knipovich Ridge and the first half or so of SFZ (see figure 5.16).

Table 5.5: Unlinked earthquakes at Knipovich Ridge and SFZ

74.2207 N	8.7535 E	1990-05-27 21:49:35 UTC	29.1 km	mb5.5	Greenland Sea
74.6444 N	8.71 E	1990-11-11 07:06:29 UTC	10.0 km	mb4.9	Greenland Sea
* 77.7413 N	7.9659 E	1991-03-18 14:26:02 UTC	10.0 km	mb4.8	Svalbard Region
77.6459 N	5.3883 E	1992-05-07 08:24:27 UTC	10.0 km	mb5.0	Svalbard Region
78.6289 N	5.4946 E	1992-07-20 07:46:47 UTC	10.0 km	mw6.6	Svalbard Region
76.2468 N	7.7292 E	1992-09-10 14:54:38 UTC	27.8 km	mb5.3	Svalbard Region
78.4994 N	6.9775 E	1993-09-23 20:04:01 UTC	10.0 km	mb4.9	Svalbard Region
78.2927 N	2.206 E	1995-03-09 07:04:22 UTC	10.0 km	mb5.1	Greenland Sea
* 77.1413 N	8.7305 E	1995-06-05 04:40:21 UTC	33.0 km	mb5.2	Svalbard Region
*77.7866 N	9.1059 E	1997-02-06 14:41:51 UTC	10.0 km	mb5.3	Svalbard Region
75.249 N	10.249 E	2000-02-03 15:53:13 UTC	10.0 km	Mw5.5	Svalbard Region
* 80.1209 N	0.7949 E	1991-06-09 10:57:06 UTC	10.0 km	mb4.9	North Of Svalbard
78.9617 N	3.4538 E	1991-09-01 06:51:04 UTC	10.0 km	mb5.2	Greenland Sea
* 81.547 N	3.3789 W	1993-04-24 10:38:30 UTC	10.0 km	mb4.9	North Of Svalbard
79.4992 N	4.0538 E	1994-01-26 12:07:14 UTC	10.0 km	mb5.1	Greenland Sea
80.839 N	0.786 E	2001-12-08 06:44:22 UTC	10.0 km	MW5.3	North Of Svalbard
82.5186 N	8.7914 W	2009-05-17 19:24:21 UTC	16.0 km	MW5.5	North Of Svalbard

Five out of the 17 unlinked events are missing their focal mechanism in figure 5.14 and these are marked with the * -sign in table 5.5. Due to a mis-match with number of events at the two maps (figures 5.14 and 5.15), including a relative location difference, it has proven difficult to analyze in detail whether the focal mechanisms play a large role in the unlinked events or not. Still, it is clear that the "beach balls" in figure 5.14 display various focal mechanisms where some seem to deviate more from the majority. The event 2009-05-17 19:24:21 UTC located at the latitudinal coordinate 82.5186 N and longitudinal coordinate 8.7914 W show to a large extent thrust fault motion, in contrast to the surrounding earthquakes that display normal faulting. A similar observation can be made for the event 2000-02-03 15:53:13 UTC located at 75.249 N and 10.249 E by comparing the two maps. There are also cases where the focal mechanism of the unlinked event appear to be similar to the neighboring events, as for the event 1992-09-10 14:54:38 UTC located at 76.2468 N and 7.7292 E, seen in the cluster of earthquakes (middle of Knipovich Ridge). As there also are 5 earthquakes with undetermined focal mechanisms it has to be considered that including earthquake with different fault geometry affect the relocation result, the same remark made for Kolbeinsey Ridge/JMFZ and Mohns Ridge. This is supported by the findings of Cleveland & Ammon [14]. As for the other parts of the northern North Atlantic Ridge, the relocation solutions were chosen with goal of having as small as possible misfit and mean or median distance shift for the relocation. The parameters are identical to those for Knipovich Ridge and SFZ except for the maximum linking distance that is 120 km for Knipovich Ridge and 100 km for SFZ. Both have been relocated with a minimum CC -coefficient of 0.90, a horizontal slowness of 0.26 s/km and minimum number of observations of 10. A period range of 25 - 80 s was chosen that corresponds to horizontal wavelengths of 100 - 300 km, almost identical to Cleveland & Ammon [14]. In figure 5.16 the distribution of distance shift from original epicenters are shown. Smallest and largest distances for SFZ are approximately 0.1 km and 35 km while for Knipovich Ridge they are approximately 0.5 km and 15 km. At Knipovich Ridge the mean and median are respectively 5.39 km and 4.11 km whereas for SFZ the mean and median are 7.19 km and 4.72 km.

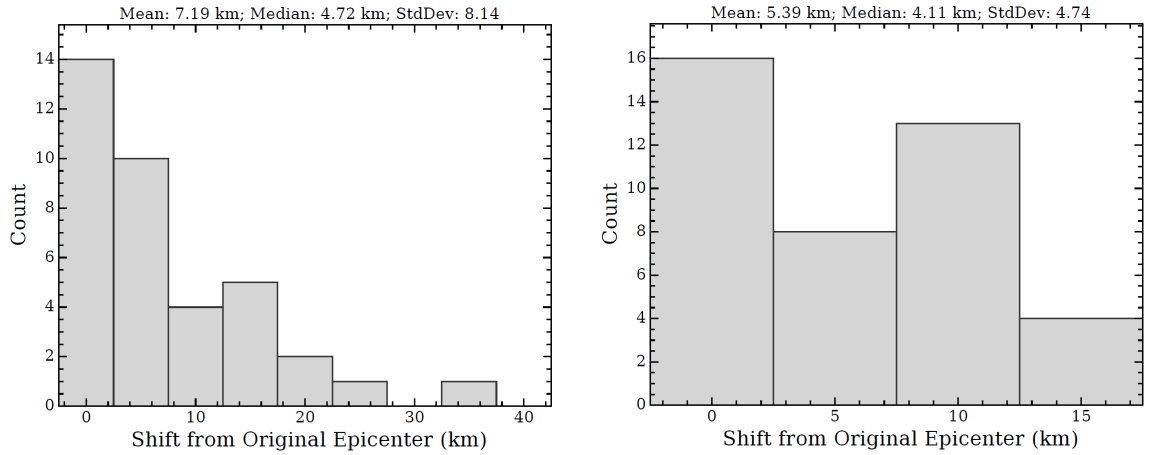

Figure 5.16: Distribution of distance shift between relocated epicentroids and the original epicenter locations. The left figure is for SFZ and the right figure is the shift for Knipovich Ridge. The mean, median and standard deviation have been calculated for analysis.

The resulting mean absolute misfit with initial and final misfit are compared between the two sections in the same way as with the distance shift, for Knipovich Ridge the initial and final misfit are 2.84 s and 0.25 s while for SFZ it is 3.03 and 0.39 s (figure 5.17).

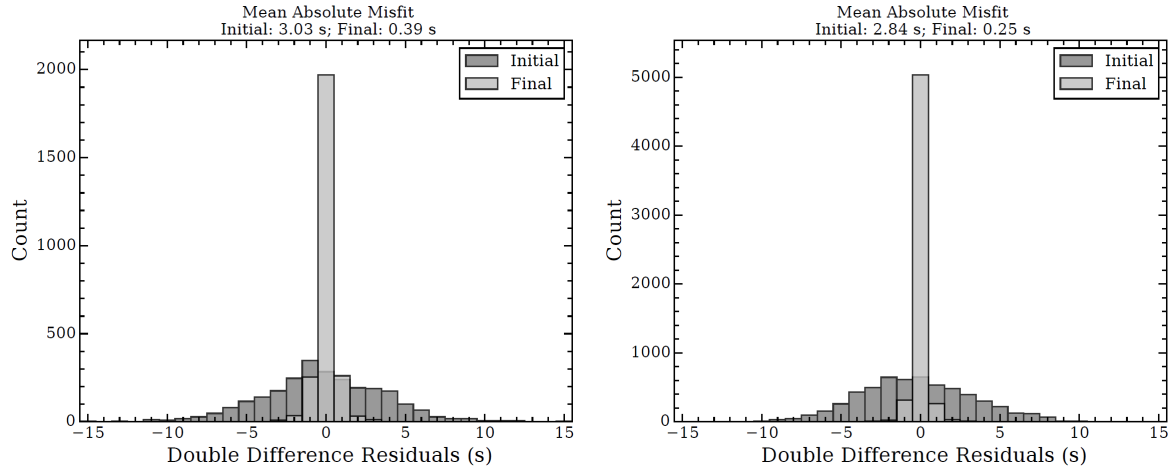

Figure 5.17: Histogram over the initial and final misfits of 60 earthquakes around Knipovich Ridge, right figure, and SFZ at the left figure. The initial misfit is calculated from the original NEIC PDE and ISC catalog locations and times.

Chapter 6

Discussion

6.1 Period and magnitude range

Using surface waves to locate or relocate seismic events have for several decades been taken advantage of by researchers. In many earlier works like Seggern [39] a reference event in a similar source area as another event are cross-correlated. There is also the long-established technique of using a master event where all other events are relocated accordingly to this one master event [43]. For more recent work, waveform envelopes have been cross-correlated with synthetic source pulses to locate seismic sources as presented by Ekström [18]. It therefore establishes that for shallow sources using surface waves over short period body-wave phases can effectively determine earthquake locations. Both Seggern [39] and Ekström [18] argues that even if arrival time of surface waves are not as precise as body waves, long-period surface waves make it possible to locate events with a greater certainty, even for sources that are of moderate size. The starting point of long period ranged surface waves to relocate seismic events can vary, however, a conservative value is found above period values of 10 s [39]. Cleveland & Ammon [14] picked the arrival times of surface waves by seismic processing that filters in the period from 30 to 80 s. A very similar processing was done by Rouland et. al. [38] with applying to filter in the period range 30-70 s. They argue that for periods smaller than 20 s, the level of noise begins to be a significant factor to the data collection. Even though with a different goal of locate unnoticed earthquakes in the Southern Hemisphere, broadband records was used to associate the earthquakes with Rayleigh waves. Cleveland & Ammon [14] further point to that for shorter periods, inter-event dispersion can prove to substantially affect the relocation. As such the period ranges chosen in this study (chapter 5) are to a large extent justified by these accords where the lowest period included is 20 s at Kolbeinsey Ridge and JMFZ. Ekström [18] bases his event-location method on the fact that observations in the period range from 30 - 500 s the noise have a considerable low level that is beneficial for surface waves.
As mentioned earlier in this study the magnitude range for earthquakes collected are M_w4.8-M_w6.7. The lower limit is chosen from a wanted focus on magnitudes starting from 5.0 and going up to 7.0 which most of the earthquakes have, but also from Cleveland & Ammon [14] which found good results from earthquakes down to M_w4.7. Whereas Ekström [18] used moment magnitude of M_w4.6 or higher to detect and locate events, Rouland et. al. [38] included events with magnitude of 3.7 to estimate epicenter locations. There are of course differences that must be considered when comparing studies, for example the specific location algorithm procedure used. Still, even though smaller earthquakes have not been treated in this thesis, it could have been a possibility to see if the DD inversion methods also give stable results. A potential pitfall with relocating smaller events are that then smaller periods must necessarily be added, thus increasing the likelihood for dispersion [14].

6.2 Azimuthal coverage and slowness

In a follow-up article by Cleveland et. al. [15], they relocate earthquakes in the northeast Pacific region, and the azimuthal coverage parameter is introduced. The first work by Cleveland & Ammon [14] only has the minimum number of stations parameter required to link any two events (along with the maximum linking distance parameter). It is well argued that even if a moderate amount of stations is required there is still a possibility that all the stations are found in a narrow azimuthal range. Such a scenario will affect the travel time difference for event-pairs, where the multiple-event DD inversion method is based on having a good azimuthal coverage [15]. They therefore decided on a minimum 50° observational span, meaning that the largest gap in stations should be no more than 310°. The value of 50° are chosen in order to include enough data while constraining the cosine pattern in the cross-correlation plots. In the python script *surfaceWaveRelocation_v2.6.py* both parameters of minimum number of stations and minimum azimuthal coverage are used. This parameter was tested for earthquakes in section 5.1, and it showed no visible difference in relocation both for a minimum azimuthal coverage of 80° as well as 150°.

Also, for the earthquakes at Knipovich Ridge a minimum azimuthal coverage of 30° was attempted. There were no visible sign of improved relocation either in this sequence. In fact, neither by removing the parameter altogether is there any notable change in relocation at a test for events in Kolbeinsey Ridge and JMFZ. Still, the default value of 50° have been entered into the execution, the same for the other two parts between Iceland and Svalbard. Why this parameter seem to have no effect on relocations is not easy to say, however, there is still the parameter of minimum number of stations that does have an effect and by looking at figure 4.1 as well as table D.1, the azimuthal coverage that each earthquake is gathered with is relatively good to begin with.
The horizontal slowness value decided upon is established from Midzi et. al. [33] and Christensen et. al. [10] as introduced in chapter 5. Both articles have analyzed fundamental mode Rayleigh waves and isolated group velocities dependent on period. In addition Christensen et. al. [10] separate the Rayleigh group velocities with oceanic age information as well. This is similar in the sensitivity tests ran by Cleveland & Ammon [14] where they used fundamental mode (synthetic) seismograms and an oceanic lithospheric model which took into account the age (0-20 Myr) the Rayleigh waves propagate through. Even though they use different period ranges and methods, both find that with longer periods there are larger errors in the group velocity values because amplitudes are heavily decreasing in such intervals. From studying figure 5 in Midzi et. al. [33] and table 3 in Christensen et. al. [10] an initial guess of $3.85km/s$ was made, the horizontal slowness corresponding approximately to $0.26s/km$. All the results displayed in chapter 5 are created with this slowness. Tests with alternative values have been tried out. In Kolbeinsey Ridge and JMFZ earthquakes a slowness of $0.25s/km$ gave an initial/final misfit of 2.69/0.29 s, a mean and median distance shift of 7.86 and 7.01 km respectively and an absolute origin time shift with mean/median of 0.89/0.75 s. In the same part of the Iceland and Svalbard region, a slowness of $0.28s/km$ gave an initial/final misfit of 2.97/0.32 s, a mean and median distance shift of 8.78 and 8.37 km respectively and an absolute origin time shift with mean/median of 0.91/0.75 s. Comparing with the results in section 5.1 the slowness $0.25s/km$ provides results with overall smaller values whereas with slowness $0.28s/km$, the values are slightly larger. In both scenarios there are no change in number of unlinked events. A comparable situation arise with alternative values for events at Knipovich Ridge. Change of slowness to $0.25s/km$ gave an initial/final misfit of 2.77/0.24 s, a mean and median distance shift accordingly to 5.39 and 3.51 km and an absolute origin time shift with mean/median of 0.95/0.73 s. A higher slowness (corresponding to a lower group velocity) of $0.28s/km$ gave an initial/final misfit of 3.03/0.27 s, a mean and median distance shift accordingly to 5.45 and 6.00 km and an absolute origin time shift with mean/median of 0.91/0.65 s. The number of unlinked events remain the same for the slowness $0.25s/km$ while for slowness $0.28s/km$ there are one less unlinked event, making the total to 10 unlinked events. Although the slowness $0.25s/km$ have smaller values it does not necessarily translate to better or more true locations. To move closer to this goal it is imperative to have a more detailed description of the seismicity at the ridges and fracture zones as well as compare locations with other studies. Looking at different values of the slowness parameter shows that the results are not fluctuating much at all, changing with a few percent or in the vicinity of ten percent.

6.3 Tests from cross-correlation

Despite Rayleigh waves usually have good signal-to-noise ratios and the noise level from a sensible determined period range as well as magnitude range is low, cross-correlation from events are very much dependent on earthquake depth and faulting geometry. Cross-correlation has the benefit of showing signal-to-noise ratio and waveform similarity. The latter is attributable to depth and faulting geometry which again are controlled by the minimum acceptable CC-coefficient and maximum linking distance in particular. Cleveland & Ammon [14] performed synthetic tests to explore how these parameters affected the cross-correlation. They found with a 0-20 Myr oceanic lithosphere model that for pairs of events with a maximum distance of 120 km the dispersion effect of surface waves did not influence the cross-correlation much. Further, in the chosen period range of 30-80 s there were little difference between the group and phase velocity. Within depths of roughly 0-30 km they concluded that this variable or parameter had little or no outcome of poor waveform similarity. Therefore it was concentrated highly on faulting geometry with varying strike, dip and rake. Also, because they studied almost only pure strike-slip faults ($strike = 0°$, $dip = 90°$, $rake = 180°$) it allowed them to look at several cases and changing just one focal parameter at a time. Strong nodal effects from large differences in focal parameters reduces the CC value greatly. The five events in the PFZ that are not linked are consequently due to a *splitting* phase shift. This is an effect that originates because the Earth do not display perfectly spherical sym-

metry, causing eigenfrequencies to separate for different azimuths [40]. In the newer study by Cleveland et. al. [15] they linked both strike-slip and normal faults together in the Northeast Pacific which makes the relationship between strike, dip and rake more complicated. In the same way it is a complicated affair to determine how the focal parameters create splitting phase shifts for the Iceland-Svalbard region. Still, the differences in focal parameters in strike, dip and rake from inter-event strike-slip faults and normal faults at the northern North Atlantic Ridge gives phase shifts that can produce the wanted cosine pattern. The complication lies in that too large differences in focal parameters can create large distance uncertainties between events. For example, for synthetic waveforms analyzed by Cleveland & Ammon [14] a dip difference of 20° can give a 10-15 km uncertainty. By choosing a CC-coefficient to 0.90 the impact of strong nodal effects on relative relocation are highly decreased. This discussion clarifies the importance of studying CC plots to confidently see if the relocation solutions are robust for earthquakes in the northern North Atlantic Ridge.

6.3.1 Cross-correlation plots for Kolbeinsey Ridge and JMFZ

The cross-correlation pattern for all 39 events at Kolbeinsey Ridge and JMFZ was examined. Even though three events were excluded for the DD inversion method they are a part of the results, mainly for getting a better understanding of why they were rejected. Also, the cross-correlation plots for event-pairs are illustrated as events are linked if the distance between them is less than the maximum linking distance and their CC-coefficients equal to or higher than the minimum acceptable CC-coefficient. A consequence is that the number of observations at stations is not considered as a parameter in the CC-plots for linking the events or not. Thus if the number of links is 1 or 4, the events show up as linked even if the minimum number of links required in the script *surfaceWaveRelocation_v2.6.py* is higher. For example, the minimum number of viable links from Kolbeinsey Ridge and JMFZ defined to 12, would still with observations from an event-pair having a CC-plot of 4 viable links look as they are relocated (though they are not). In figure 6.1 and 6.2 cross-correlation plots of two different event-pairs are presented, the first is included in the location analysis with 12 links whereas the last is not included because the maximum linking distance is too high.
Each figure consists of two plots; the upper plot shows measured traveltime differences (in seconds) as a function of azimuth of the station. The maximum absolute value for a traveltime difference or lag-time is also a parameter in the relocation method of Cleveland & Ammon [14], defined to 50 s. This is the reason why the vertical axis in the upper plot is limited to values from -50 s to +50 s. The title of the figures gives the two events characterized by their origin time, that are cross-correlated. It also specifies the channel, which for all CC-plots in the work of this thesis is only BHZ. The number of observations or links will therefore for BHZ be the same as the total number. The lower plot shows CC-coefficient from 0.0 to 1.0 (previously described in section 4.4), as a function of azimuth of the station. The continuous black line marks the minimum acceptable CC-coefficient value, defined by the user. Points with red color are measurements that have a CC-coefficient at or above this defined value. Gray points are the rest of the measurements that did not meet this requirement. Using figure 6.1 as an example, there are several measurements with a CC-coefficient of approximately 0.5, and even a few that are at the very bottom (barely visible). This wide range of CC-coefficients demonstrate that waveforms for these two events are at some stations very similar, and in other stations they are quite different. It is natural effect when having stations with good azimuthal coverage, therefore in most CC-plots, a similar pattern will emerge.

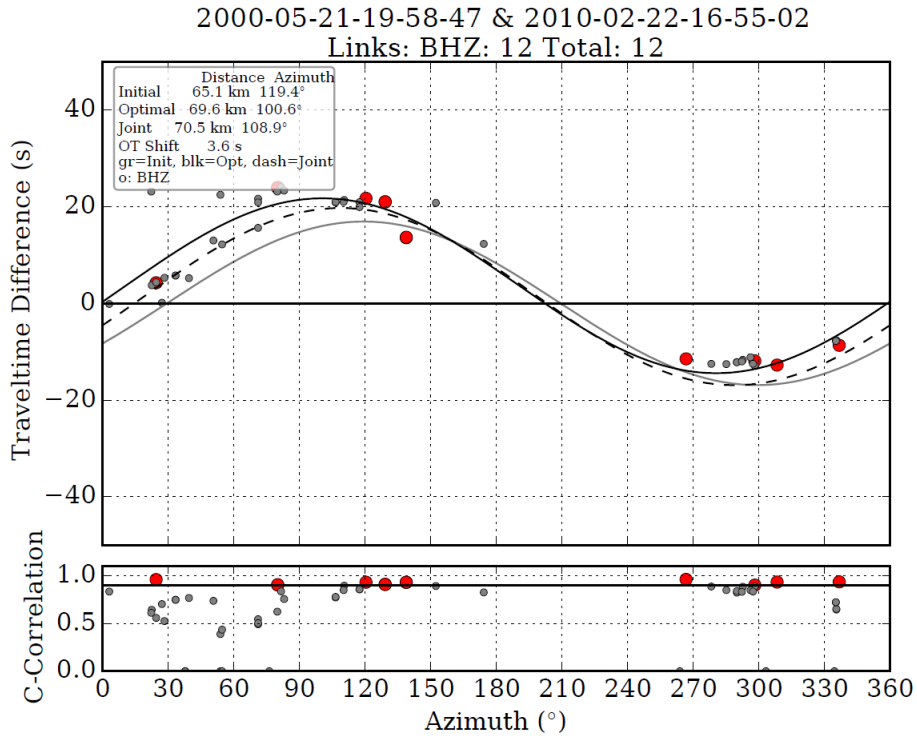

Figure 6.1: The earthquakes labeled 2000-05-21-19-58-47 and 2010-02-22-16-55-02 are cross-correlated and show 12 observations at stations which pass the requirements (red circles). Gray circles are observations at stations that do not meet the requirements, i.e. the CC-coefficient is under 0.90. The solid black line is termed *optimal* (uppermost left corner) and is a sine curve function that best fits the red measurements. The gray solid line is a sine curve termed *initial*, calculated from the initial earthquake locations. The dashed line shows the result of the inversion when all event-pairs have been cross-correlated.It is a sine curve termed as *joint*. Relative locations of the two events corresponding to the 3 curves is given in the upper left box. Plot of cross-correlation values at the bottom show the minimum acceptable CC-coefficient with the clear horizontal black line, drawn at the 0.90 mark. Both the traveltime difference plot at the top and the CC-coefficient plot at the bottom is a function of azimuth going from 0° - 360°.

Having just the minimum number of links required, figure 6.1 show a cross-correlation between two events that are used in the relocation procedure. The optimal distance of the events are changed from 65.1 km to 69.6 km by combining the traveltime difference values and horizontal slowness value. A cosine pattern is visible from the observations which matches relatively well with the solid line sine curve. A likely cause for seeing only 9 red points though the title clearly states it is 12, is that two or more measurements are sometimes included in the same red circle. There are no indications of strong nodal effects with a splitting phase shift, even though the number of observations is quite low to give a definitive pattern. Instead it is seen that a difference in event location does indeed produce at systematic cosine variation from the time shifts as stated by Cleveland & Ammon [14]. Had the red circles in figure 6.1 on the right side been removed, there would not be a characteristic cosine pattern to describe variation of traveltime with azimuth. If a good coverage of variation of traveltime with azimuth is not present, the DD inversion method will be limited in its ability to precisely and accurately relocate earthquakes (as described in section 3.2). The plots for the 36 events that are relocated all display a systematic cosine pattern similar or better compared with this CC plot. In some cases a fewer number of observations than 12 do produce a robust correlation pattern confidently. The joint sine curve and the optimal sine curve are quite similar (figure 6.1), and the calculations only differ by 0.9 km. This demonstrate that the final distance between event-pair is almost the same as the distance calculated from just the observations marked in the figure.
On the other hand the maximum linking distance parameter can affect cross-correlation time shifts by not linking together an event-pair (figure 6.2). It appears that there are more than 12 measurements above or at the 0.90 CC-coefficient mark. They are not red because the maximum linking distance defined to 80 km are below the event distance, approximately 90 km. By this example it could be possible to increase the maximum linking distance decided on in section 5.1 to have more double-difference expressions.

Figure 6.2 shows the definitive cosine pattern that is so central for relocating earthquakes. Because the maximum linking distance has been defined so low for events at Kolbeinsey Ridge/JMFZ, the results from this CC plot is one of few that could easily been used in the relocation procedure. If it would improve the locations much is unlikely as these two events are none of the events that are unrelocated. This is seen by comparing the joint sine curve with the initial sine curve, although not very different, there are minor changes in the traveltime difference. Increasing the maximum linking distance from 80 km to 120 km differ little in most relocations and the number of unlinked events stay the same. The unlinked events all have a majority of either large inter-distances or very low CC-coefficient values or both. Some display average CC-coefficient values around 0.50 to 0.80 both at large distances (200-400 km) and moderate distances (120-200 km). A few CC plots do have observations that meet the requirements, but the number of these observations do not exceed 3.

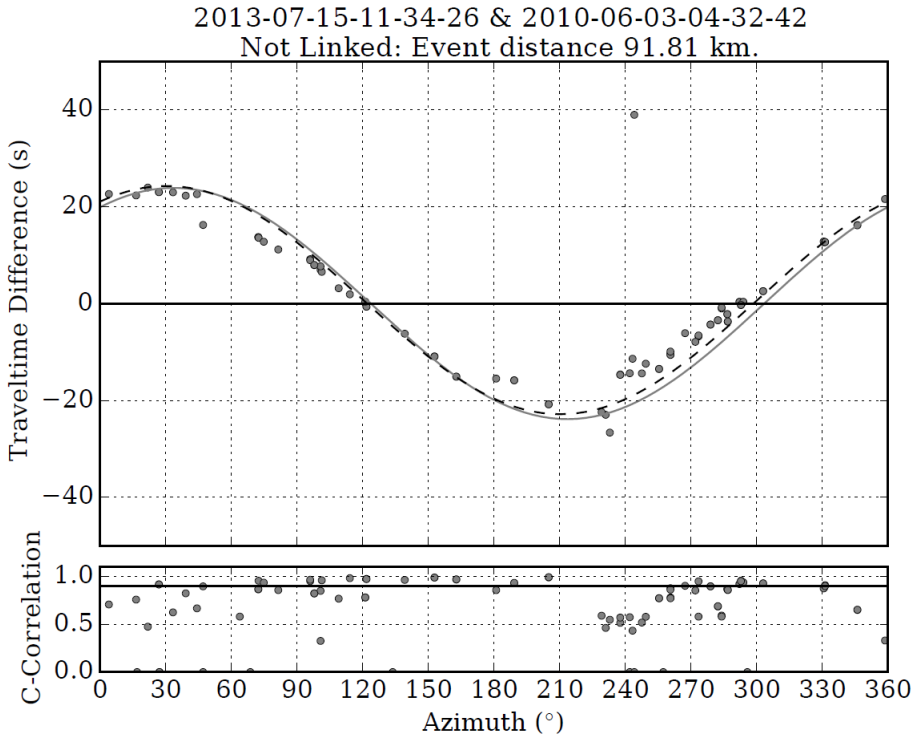

Figure 6.2: The same as figure 6.1 for earthquakes labeled 2013-07-15-11-34-26 and 2010-06-03-04-32-42. They are cross-correlated but show no observations which pass the requirements (gray circles), i.e. the event-distance is above 80 km even though CC-coefficient is above 0.90 for several observations.

One of the earthquakes that are not relocated in the preferred solution, is 1999-07-01 02:06:58 UTC. In figure 6.3 it is cross-correlated with the earthquake 1999-07-01 03:20:42 UTC. It is interesting to see that the CC-coefficients are so low, even though the depth and magnitude are very similar (table A.1). The fact that they are located so close to each other, can suggest that the depths are in reality different or rather that the focal mechanisms are different. However, the focal mechanism map in figure 5.2 indicate that the their focal mechanism is similar. That the earthquakes occur on the same date, only just over an hour a part, makes it difficult to think that they are caused by substantial different mechanisms. Other CC plots for 1999-07-01 02:06:58 UTC gives a similar description. The event-pairs may also not be linked because of too large distances. For the unrelocated event 2008-01-15 06:35:14 UTC the CC plots presents nothing new, though in general the CC-coefficients are higher compared with the CC-coefficients for 1999-07-01 02:06:58 UTC.

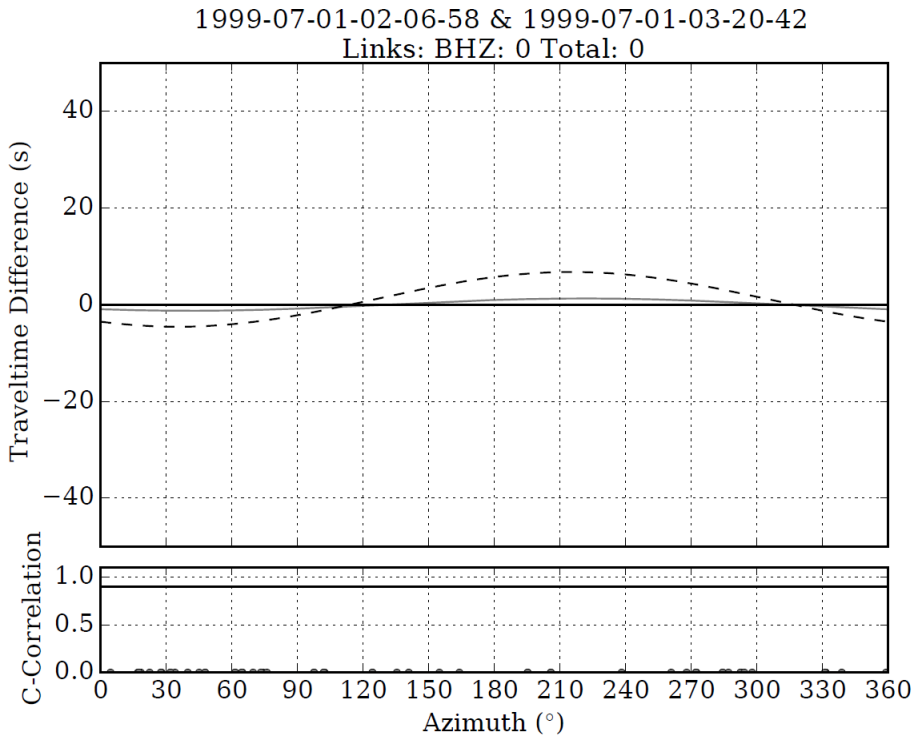

Figure 6.3: The same as figure 6.1 for earthquakes labeled 1999-07-01-02-06-58 and 1999-07-01-03-20-42. They are cross-correlated but show no observations which pass the requirements. The joint sine curve shows that even though 1999-07-01-02-06-58 is not relocated, the earthquake 1999-07-01-03-20-42 is.

6.3.2 Cross-correlation plots for Mohns Ridge

For all 62 events at Mohns Ridge the cross-correlation plots were examined. As stated in subsection 6.3.1 even the unlinked events (5 in total) and those single plots that do not meet the requirement values with maximum linking distance, minimum CC-coefficient and/or minimum number of links are studied. This is to see if the parameters decided on give acceptable results, or perhaps some slight changes should be done to improve the cross-correlations that results in the relocations. Compared with CC plots at Kolbeinsey Ridge and JMFZ, the chosen parameter-values are almost identical. Most focus is therefore put on analyzing the CC plots for the parameter-values that are not the same, i.e. the minimum number of links defined to 8 and the maximum linking distance defined to 120 km. Because these values allow for more CC calculations to be included in the DD inversion procedure, it is essential to control for the systematic coverage of traveltime variation. A few number of CC plots from the total are plotted with exact 8 links like the one in figure 6.4.

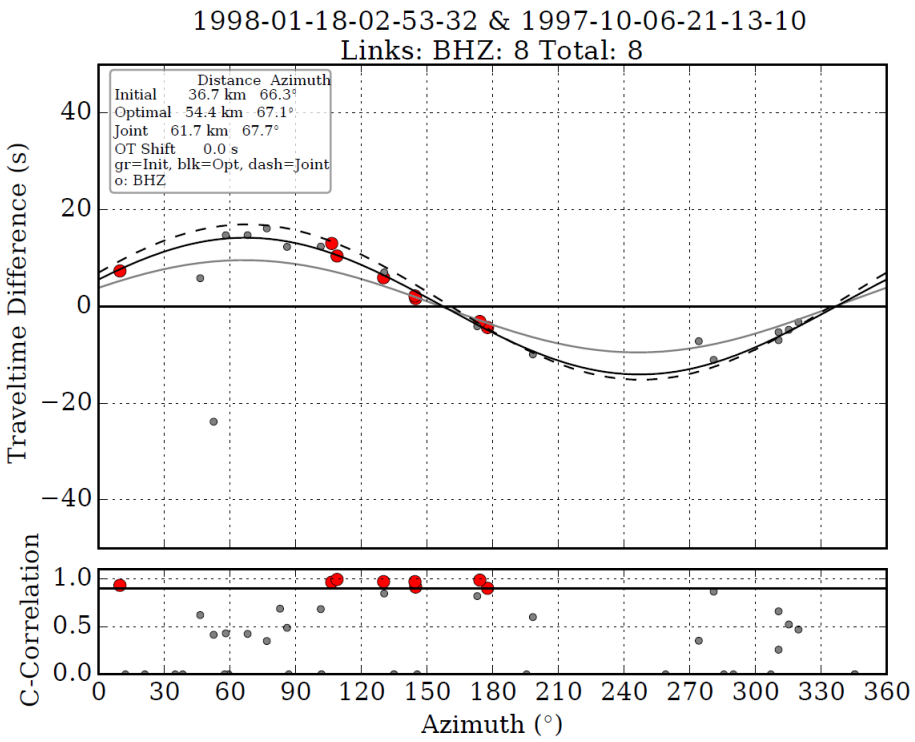

Figure 6.4: The same as figure 6.1 for earthquakes labeled 1998-01-18-02-53-32 and 1997-10-06-21-13-10. They are cross-correlated and show 8 observations at stations which pass the requirements (red circles). Distance between the events are changed from 36.7 km to 54.4 km with the red measurements. The final distance between the events is from the DD inversion estimated to 61.7 km.

Other CC plots with 8 linked observations show both slightly worse azimuthal coverage while other show better coverage, similar to the CC plot in figure 6.1. They do all however cover a span of azimuths of more than 50° as defined in the *surfaceWaveRelocation_v2.6.py* script. This consideration is most likely not a coincidence, even though it may seem as the minimum azimuthal coverage of links have little affect on relocations (at Kolbeinsey Ridge and JMFZ) as discussed in section 6.2, it is clear that the parameter do affect the linked event-pairs. Taking it further the challenge then becomes to decide if 8 as the minimum number of links and if the minimum coverage of links with 50° are good enough and ultimately produce robust results. As recognized in figure 6.5 below increasing the minimum number of links for cross-correlation do not necessarily translate to better azimuthal coverage of traveltime differences. One possibility is to increase the minimum number of links while simultaneously also increasing the minimum azimuthal coverage. Such a change comes with an consequence of fewer relocated earthquakes. A test for Mohns Ridge with 10 links and azimuthal coverage of 80° was performed and resulted in 7 unlinked events which is not a huge increase from the preferred relocation with 5 unlinked events. It resulted also in an identical final misfit and minimal difference in mean and median distance shift. Yet with this setting the number of iterations changed from 4 to over 7 iterations, indicating that there are some problems with settling on final locations.
The measurements in figure 6.6 seem to lie on a line instead of displaying a clear cosine pattern, yet by closer examination a small traveltime variation are plotted within an amplitude of 0 - 1 s. It demonstrates that the events are located very close to each other. Not too many event-pairs are so close as to result in the pattern visible in figure 6.6, though they all display this systematic azimuthal pattern that should arise for events that differ in locations, according to Cleveland & Ammon [14].

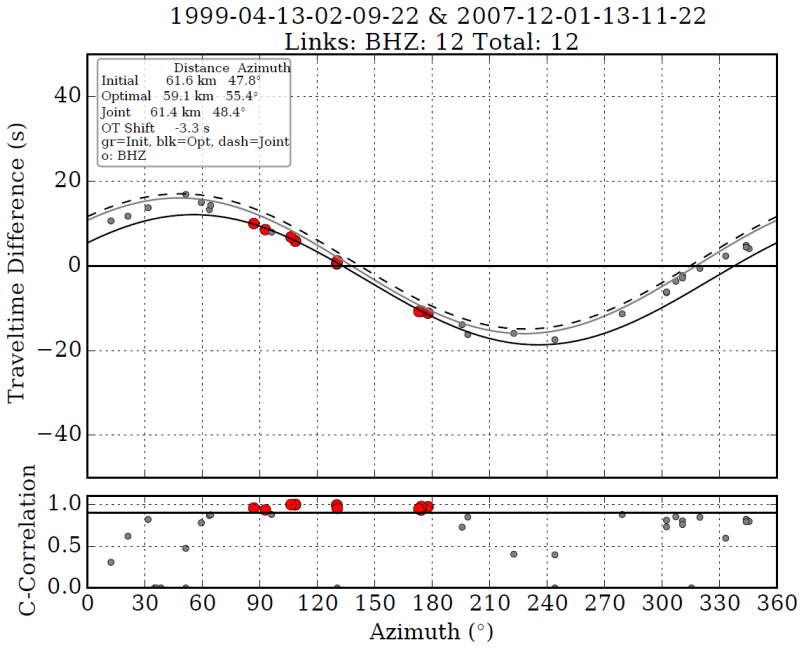

Figure 6.5: The same as figure 6.1 for earthquakes labeled 1999-04-13-02-09-22 and 2007-12-01-13-11-22. They are cross-correlated, showing 12 observations at stations which pass the requirements. Distance between the events are changed from 61.6 km to 59.1 km with the red measurements. The final distance between the events is from the DD inversion estimated to 61.4 km. Both the traveltime difference plot at the top and the CC-coefficient plot at the bottom is a function of azimuth going from 0° - 360°.

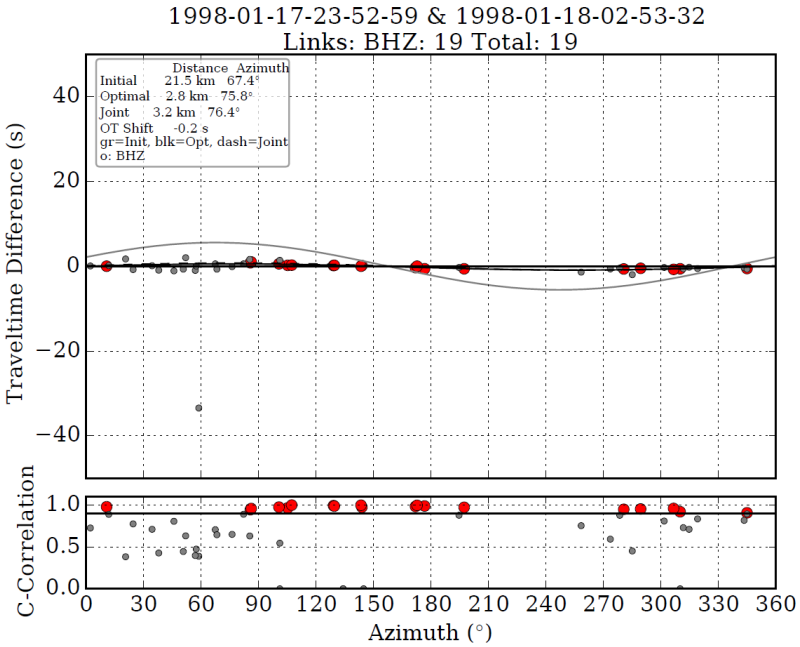

Figure 6.6: The same as figure 6.1 for earthquakes labeled 1999-01-17-23-52-59 and 1998-01-18-02-53-32. They are cross-correlated, showing 19 observations at stations which pass the requirements. Distance between the events are changed from 21.5 km km to 2.8 km km with the red measurements. The final distance between the events is from the DD inversion estimated to 3.2 km. Both the traveltime difference plot at the top and the CC-coefficient plot at the bottom is a function of azimuth going from 0° - 360°.

Figure 6.6 is a good example of how the relocation has improved, since the initial sine curve do not seem to fit particularly well with the measurements. From an initial distance of 21.5 km the distance

for the event pair is reduced to 3.2 km, a substantial difference. Overall there are more varied CC plot for Mohns Ridge compared with Kolbeinsey Ridge/JMFZ, but none shows a splitting phase shift. There are cases of CC plots that look very good despite a large inter-event distance, some close to 200 km. It could be tempting to use these event-pairs , but in general this stretches the limit of assumptions made for the relocation method as described in section 3.2. With only a minimum of 8 links, the validity of the relocations need good, constrained data and azimuthal coverage as seen in figure 6.4. The relocation map is therefore kept with the same parameters as presented in section 5.2.

6.3.3 Cross-correlation plots for Knipovich Ridge and SFZ

Most of the 77 earthquakes at Knipovich Ridge and SFZ were examined by their cross-correlation plots. The total unlinked events of 17 earthquakes were also included, even though they did not pass the requirements demanded by the relocation procedure, they were studied to gain additional understanding of the results. As noted earlier, the only difference between events relocated at Knipovich Ridge and those at SFZ is in the maximum linking distance, being 120 km and 100 km respectively. Both areas have an requirement of a minimum of 10 linked observations, 2 less than the chosen number at Kolbeinsey Ridge and JMFZ. Perhaps the major difference from Knipovich Ridge/SFZ compared with the other parts is the notable lack of clustered earthquakes along with general stretched areas with earthquakes far in between. It does put more strain on the limits of the relocation method because of this. This was particularly in mind when examining the CC plots, as well as the effects of different parameters.
For all cross-correlated events that have been relocated the traveltime difference measurements displays a well-behaved cosine pattern with no signs of splitting phase shift. There are not too many plots that contain exactly the minimum of 10 links but they all show good azimuthal coverage like the one below (figure 6.7). In most cases linked event-pair with 8 observations do also show a systematic cosine pattern. However, for events in the SFZ with a maximum linking distance of 100 km instead of 120 km (that was chosen for events at Knipovich Ridge), there are quite a few event-pairs that have not been linked because of this limit. With approximately an event distance of 110 km, the two events in figure 6.8 have not been linked and therefore the data have been included to the relocation solution.

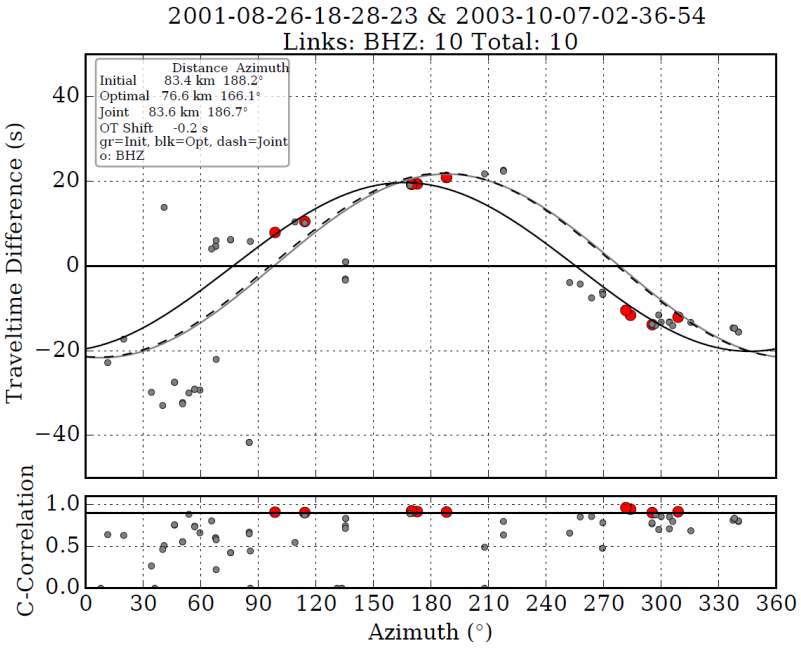

Figure 6.7: The same as figure 6.1 for earthquakes labeled 2001-08-26-18-28-23 and 2003-10-07-02-36-54. They are cross-correlated, showing 10 observations at stations which pass the requirements. Distance between the events are changed from 83.4 km to 76.6 km km with the red measurements. Both the traveltime difference plot at the top and the CC-coefficient plot at the bottom is a function of azimuth going from 0° - 360°.

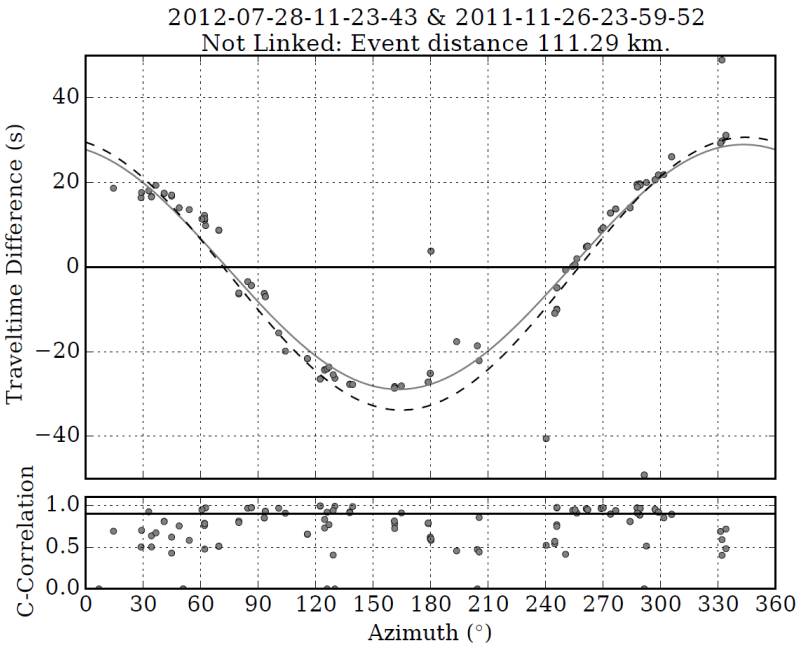

Figure 6.8: The same as figure 6.1 for earthquakes labeled 2012-07-28-11-23-43 and 2011-11-26-23-59-52. They are cross-correlated but show no observations at stations because they are spaced too far a part. Both the traveltime difference plot at the top and the CC-coefficient plot at the bottom is a function of azimuth going from 0° - 360°.

Figure 6.8 displays many CC - coefficients that are at or above the 0.90 mark, in addition to clearly having a cosine variation in traveltime difference as expected for two earthquakes at a distance. Still, even by increasing the maximum distance to 120 km the relocation maps do not change notably. The distance shifts are from the original (mean 7.19 km, median 4.72 km, standard deviation 8.14 km) changed to a mean of 8.40 km, median 5.40 km and standard deviation 8.30 km. The 6 same events at SFZ are still not relocated, keeping their original epicenter position. These events can be; separated from other events with a considerable distance, have too few observations that pass the CC- coefficient mark or only having observations with very low coefficients (or even both). The last two scenarios are presented in figures 6.9 and 6.10.

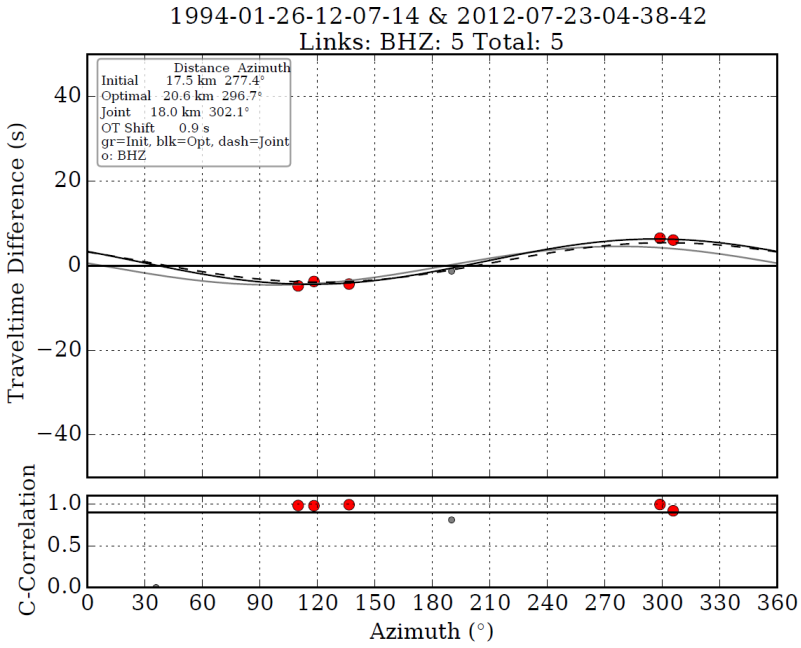

Figure 6.9: The same as figure 6.1 for earthquake labeled 1994-01-26-12-07-14, that has not been relocated. Here linked with the earthquake labeled 2012-07-23-04-38-42 but only having 5 observations that fits the requirements.

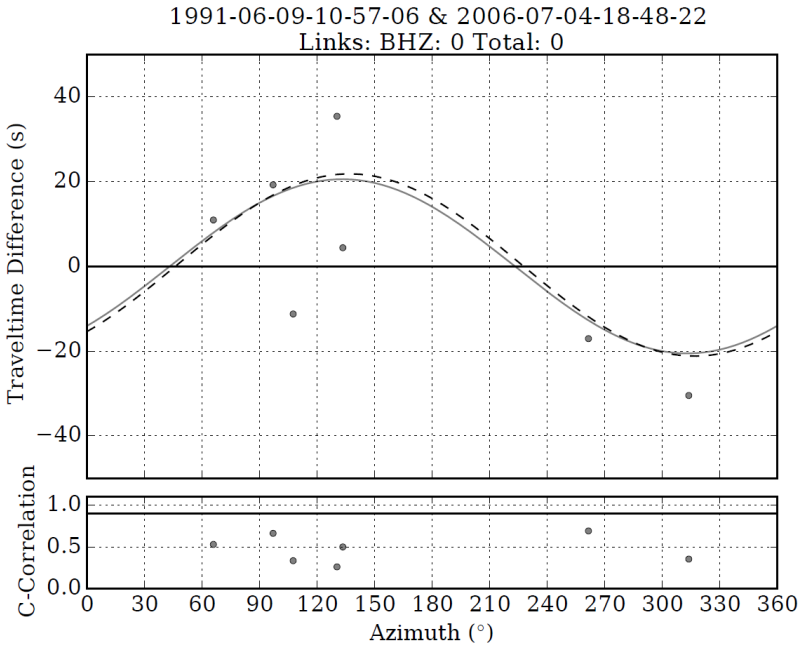

Figure 6.10: The same as figure 6.1 for earthquake labeled 1991-06-09-10-57-06, which has not been relocated. It has very few CC - coefficient observations with the earthquake labeled 2006-07-04-18-48-22 and none that are good enough.

Overall the events that have been relocated at Knipovich Ridge and SFZ give fewer CC plots with data that have been included into the relocation process (compared to events at Kolbeinsey Ridge/JMFZ and Mohns Ridge). This is perhaps to be expected as the earthquakes are not clustered as much together, especially at the Spitsbergen Fracture Zone - map. While at Knipovich Ridge the original epicenter locations show some constrained earthquake pattern, the original epicenter locations at SFZ are more scattered.

6.4 Structures at the northern North Atlantic Ridge

The results show that particularly epicentroids at Kolbeinsey Ridge/JMFZ and Mohns Ridge are more spatially consistent and fluctuate less than the original epicenter location, analogous to the analysis of Cleveland & Ammon [14]. To illuminate the improved linear trends, the original as well as the relocated events at Kolbeinsey Ridge/JMFZ and Mohns Ridge are separated from the maps, see figures 6.11 and 6.12.

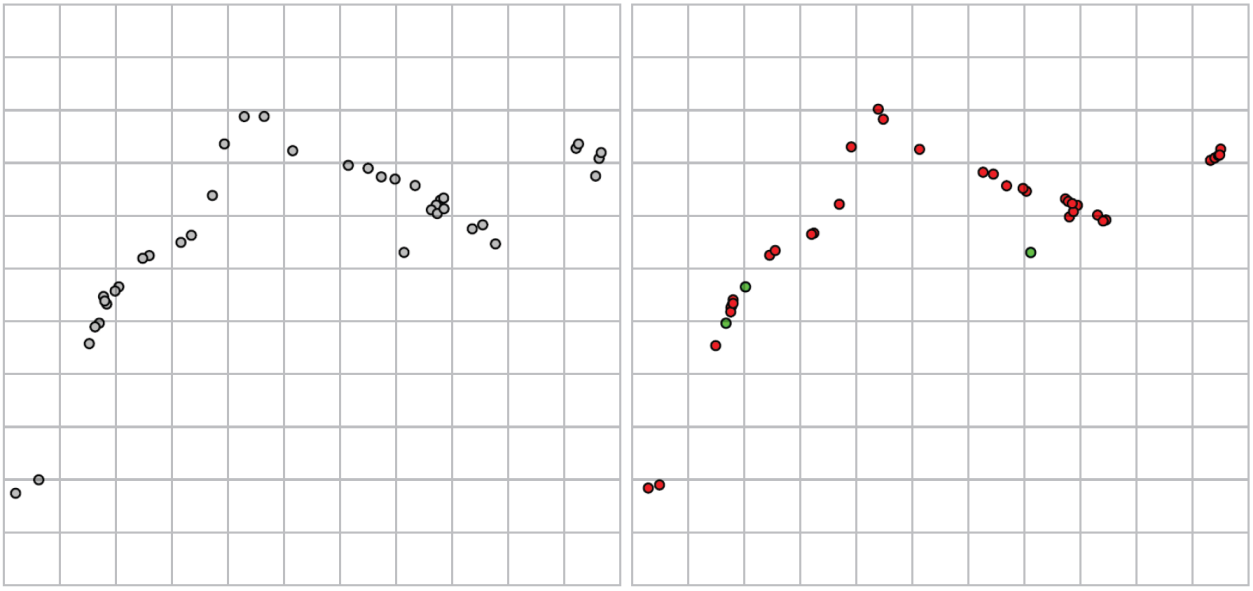

Figure 6.11: Gray circles show the original epicenter locations from the ISC and NEIC PDE catalogs. Red circles represent the earthquakes that have been relocated to the new epicentroid locations.

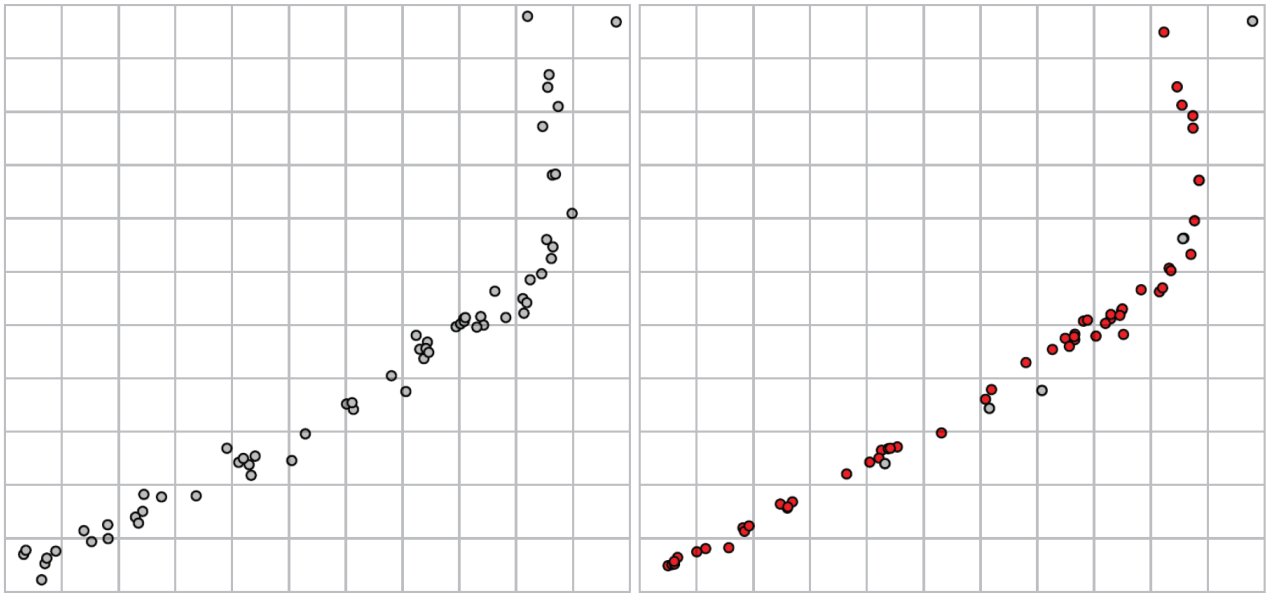

Figure 6.12: Gray circles show the original epicenter locations from the ISC and NEIC PDE catalogs. Red circles represent the earthquakes that have been relocated to the new epicentroid locations.

Both relocations solutions are shown to be more constrained to the ridges/fracture zones, as illustrated in chapter 1. The epicentroids at Mohns Ridge have a gradual curve that appear to follow the bathymetric signature, whereas the epicenter locations are more abrupt. Although this observation is not by itself sufficient to make any clear stand, the figures and works gathered in chapter 1 presents a

stronger case for a more realistic solution. For the earthquakes at Kolbeinsey Ridge/JMFZ there are no definitive bathymetry. Still the epicentroid pattern do seem to be more "fluid" by following the Kolbeinsey Ridge and being in the center of JMFZ, compared to the original epicenter locations. Adding more earthquakes would likely show more of a clear pattern along the active regional structures, as in the case of Mohns Ridge. The epicentroids at SFZ do to an extent follow the bathymetric signature, though it lacks a behaved pattern as the two foregoing parts. At Knipovich Ridge the epicentroids in general also show to go inwards to the deeper parts. Observations like these reveal some of the possibilities, but also limitations of the DD- based relocation method. Where there are few or no earthquakes close to the tectonic structures, the method seem to suffer. On the other hand, if a substantial dataset is available in the catalogs, the method can be valuable to better outline the structural features. The conclusion for SFZ is that the events are located at a less uniform structure. As described in section 1.3, this does makes sense since this area consists of ridge-segments and fracture zones. At the magnitude range from 5.0 to 7.0, Kolbeinsey Ridge, JMFZ and Mohns Ridge are more seismic active than in higher latitudes. The relocations are not sufficient to discuss larger structural trends, by connecting the different ridge-segments and fracture zones to each other. It is possible that could be done if earthquakes with smaller magnitudes are included in the datasets.

Chapter 7

Conclusion and future work

7.1 Conclusion

Earthquakes are studied in many settings, by aiming for a better understanding of tectonic processes, how earthquakes reoccur and interact with each other, and so on. Perhaps the most basic characteristic of earthquakes is their location. Conventionally earthquakes are located using the arrival time of short-period body waves. Being registered on several stations, the different arrival times are taken advantage of in iterative triangulation methods [18]. This procedure limits the location accuracy, affecting how the study of fine structure seismicity [43]. The location solutions are often biased by a heterogeneous velocity structure. Many researchers have therefore developed different techniques for reducing this effect (on earthquake locations), according to Wolfe [46]. Such techniques or methods often require that there is an explicit solution for correcting the velocity heterogeneity [46], a solution that only partly can be achieved. Instead of focusing on finding a method that can solve the velocity heterogeneity -effect, Wolfe [46] describes that using difference operators there is no need for solving for velocity heterogeneity. Got et. al. [20] and Waldhauser & Ellsworth [43] have developed double-difference methods based on the same mathematical efforts, where both rests on the assumption that the distance between an earthquake-pair is small. However, the method by Got et. al. [20] only reduce a constant velocity path bias, in contrast to the method by Waldhauser & Ellsworth [43] that can resolve relative locations through distance-dependent weighting. By using the characteristics of long-period surface waves with low velocity and strength of signals at large distances, relative earthquake locations can be estimated more precise in oceanic regions that are isolated from local stations [7, 14, 18, 39].

In this thesis a relative relocation method developed by Cleveland & Ammon [14] has been applied to moderate-sized earthquakes at the northern North Atlantic Ridge. More specifically, the region between Iceland and Svalbard have been divided into four parts, based on the regional structures. From 68° 00′ N to 72° 30′ N and 18° 00′ W to 5° 00′ W, 36 earthquakes at the Kolbeinsey Ridge and JMFZ are relocated. From 70° 30′ N to 76° 00′ N and 5° 00′ W to 11° 00′ E, 57 earthquakes at Mohns Ridge are relocated. From 74° 00′ N to 79° 30′ N and 1° 00′ E to 11° 00′ E, 30 earthquakes at Knipovich Ridge are relocated. From 78° 50′ N to 83° 30′ N and 9° 00′ W to 6° 00′ E, 30 earthquakes at SFZ are relocated. By the maximum value of the cross-correlation function, Rayleigh wave time shifts were estimated to be applied to the DD- based inversion method. The earthquake datasets for the northern North Atlantic Ridge were collected with the Wilber 3 interface, provided by IRIS. The results show that the initial epicenter locations are substantially improved for most earthquakes, in particular at Kolbeinsey Ridge/JMFZ and Mohns Ridge. Misfit from the DD method are estimated to 0.30 s for Kolbeinsey Ridge/JMFZ and 0.25 s for Mohns Ridge. The mean origin time shift between epicentroids and epicenters is for Kolbeinsey Ridge calculated to 0.89 s whereas for Mohns Ridge it is calculated to 1.47 s. This indicates that the relative epicentroid solutions found with Rayleigh waves provide precisely estimation, as concluded by Cleveland & Ammon [14]. For Knipovich Ridge and SFZ, several events are shown to not be relocated, however, the results still give final misfits of 0.25 s and 0.39 s, respectively. The mean origin shift is for both estimated to 0.93 s. Therefore, the title in Cleveland & Ammon [14] effectively describe that the relative relocation method is indeed precise.

The method has also proven to produce tectonically consistent epicentroid locations, with no consideration of the earthquake's focal mechanisms. Although no comparison with locations from other studies are done, the earthquake pattern in Kolbeinsey Ridge/JMFZ, Mohns Ridge and in parts Knipovich Ridge, seem to be relatively accurate as they show increased linear trending of the structures. In contrast the original epicenter locations (found by body waves), display a more scattered earthquake pattern. The earthquakes at SFZ are too few and the distances between many event-pairs is too large to confidently conclude that the epicentroid locations are accurate or not. It is my experience by working with the relocation method from Cleveland & Ammon [14], that the relocations are robust, provided that enough earthquakes are close together. If not, then the relocation solutions do seem to be fundamentally limited [46].

7.2 Future work

By testing synthetic waveforms, Cleveland & Ammon [14] argues that as long as each event is linked to a multiple of other events, outlier events do not affect the rest of the relocations too much. In some cases at Knipovich Ridge and particularly at SFZ, the large structural areas lack sufficient amount of earthquakes. The specific locations of some of these epicentroids should be questioned and studied in more detail. One approach could be to include earthquakes with smaller magnitudes, for outliers that miss neighboring earthquakes. For earthquakes that have moved larger distances or that not been relocated at all, could be caused by variation in fault geometry. The northern North Atlantic Ridge is shown to consist of earthquakes from strike-slip fault, normal faults as well as some thrust faults. The CC plots play an important role in checking that the measurements have good azimuthal coverage, as well as for studying the CC-coefficients. If they are low, a likely cause is a difference in focal mechanism for the event-pairs. For many events that have not been relocated, a detailed explanation is unresolved. It is recommended that more effort is put on this problem. By variating the parameter -values, different events can be linked. Including more events or removing events also have an effect on the specific epicenter locations, such that there are some uncertainty with the final epicentroid solutions. Cleveland & Ammon [14] propose a $\pm 5km$ uncertainty, based on their strike-slip earthquakes. Having the various focal mechanisms at the northern North Atlantic Ridge, a similar if not higher uncertainty -value is also proposed here.
Even if the relocations seem to be robust and constrained to the ridges and fracture zones, it does not rule out that all the relocated epicentroids (and original epicenters) can have a regional bias, i.e. that the event pattern as a whole is shifted [14]. The double-difference relocation method is based on predetermined earthquake locations and trying to relocate each earthquake relative to others. This means that calculating the difference in traveltime can possibly only improve relative positions of the earthquakes. It can however be partly solved by applying static shifts to the relative locations is done for the newer study by Cleveland et. al. [15]. Along with testing the relocation method with magnitudes perhaps around $3.5 - 4.0$, looking into applying static shifts to the datasets are ideas for future work that will give a better understanding and knowledge of the earthquakes at the northern North Atlantic Ridge.

References

[1] Ahern, T., Barnes, D., Benson, R., Buland, R., Casey, R., Halbert, S., Knight, T., Skjellerup, K., Styles, R., and Trabant, C. (2012). SEED Reference Manual. 1-224. `http://www.fdsn.org/seed_manual/SEEDManual_V2.4.pdf`, accessed 30.03.2017.

[2] Aki, K. and P. G. Richards (1980). Quantitative Seismology : Theory and Methods , Volume 1 & 2. *San Francisco, Freeman.*

[3] Ammon, C. J., et al. (1994). Routine Estimation of Earthquake Source Complexity: the 18 October 1992 Colombian Earthquake. *Bull. Seismol. Soc. Amer. 84(4): 1266-1271.*

[4] Anderson, D. L. and Regan, J. (1983). Uppermantle anisotropy and the oceanic lithosphere. *Geophysical Research Letters 10(9): 841-844.*

[5] Anderson, E., et al. (1999). LAPACK Users' Guide, 3rd Edition. *Philadelphia, Pa., Society for Industrial and Applied Mathematics SIAM, 3600 Market Street, Floor 6, Philadelphia, PA 19104. 9.*

[6] Ekström, G., M. Nettles, and A. M. Dziewonski (2012). The global CMT project 2004-2010: Centroid-moment tensors for 13,017 earthquakes. *Phys. Earth Planet. Inter., 200-201, 1-9, 2012. doi:10.1016/j.pepi.2012.04.002.*

[7] Barmin, M. P., et al. (2011). Epicentral location based on Rayleigh wave Empirical Green's Functions from ambient seismic noise. *Geophysical Journal International 184(2): 869-884.*

[8] Beyreuther, M., Barsch, R., Krischer, L., Megies, T., Behr, Y., and Wassermann, J. (2010). ObsPy: A Python Toolbox for Seismology. *SRL, 81(3), 530-533. DOI: 10.1785/gssrl.81.3.530.*

[9] Byrkjeland, U., Bungum, H., and Eldholm, O. (2000). Seismotectonics of the Norwegian continental margin. *Journal of Geophysical Research: Solid Earth 105(B3): 6221-6236.*

[10] Christensen, D. H., Kimball, J.K., and F.J. Mauk (1980). Rayleigh Wave Group Velocity Dispersion in the North and South Atlantic Oceans. *Bulletin of the Seismological Society of America 70(No 5): 1787-1809.*

[11] Clark, A. (2013). Manuals: Wilber 3. Modified 2016-09-14. `http://ds.iris.edu/ds/nodes/dmc/manuals/wilber-3/`, accessed 05.04.2017.

[12] Clark, A., and Casey, R. (2015). Software Downloads JWEED v. 4.1.3 Manual. urlhttp://ds.iris.edu/ds/nodes/dmc/software/downloads/JWEED/4-1-3/manual/, accessed 05.04. 2017.

[13] Cleveland, K.M. (2016). README.txt. Surface Wave Relocation - surfWaveRelocation_vX.X.py (pp. 1-5).

[14] Cleveland, K.M. and Ammon, C.J. (2013). Precise relative earthquake location using surface waves. *Journal of Geophysical Research: Solid Earth, Vol. 118, 2893-2904, doi:10.1002/jgrb.50146, 2013.*

[15] Cleveland, K. M.,VanDeMark, T.F., and C.J. Ammon (2015). Precise relative locations for earthquakes in the northeast Pacific region. *Journal of Geophysical Research: Solid Earth 120(10): 6960-6976.*

[16] Dauteuil, O., and J.P. Brun (1996). Deformation partitioning in a slow spreading ridge undergoing oblique extension: Mohns Ridge, Norwegian Sea. *Tectonics 15(4): 870-884.*

[17] Dziewonski, A. M., T.-A. Chou and J. H. Woodhouse (1981). Determination of earthquake source parameters from waveform data for studies of global and regional seismicity. *J. Geophys. Res., 86, 2825-2852, 1981. doi:10.1029/JB086iB04p02825.*

[18] Ekström, G. (2006). Global detection and location of seismic sources by using surface waves. *Bulletin of the Seismological Society of America 96(4 A): 1201-1212.*

[19] Engen, ., Eldholm, O., and H. Bungum (2003). The Arctic plate boundary. *Journal of Geophysical Research, Vol. 108, No. B2, 2075.doi: 10.1029/2002JB001809, 2003.*

[20] Got, J.L., Fréchet, J., and F.W. Klein (1994). Deep fault plane geometry inferred from multiplet relative relocation beneath the south flank of Kilauea. *Journal of Geophysical Research: Solid Earth 99(B8): 15375-15386.*

[21] Halbert, S. (2012). Appendix A: Channel Naming. *SEED Reference Manual, 133-140.* `http://www.fdsn.org/seed_manual/SEEDManual_V2.4.pdf`, accessed 30.03.2017.

[22] Havskov, J. and K. Atakan (1991). Seismicity and volcanism of Jan Mayen Island. *Terra Nova 3(5): 517-526.*

[23] Helffrich, G., et al. (2013). The Seismic Analysis Code : A Primer and User's guide. *Seismic Analysis Code, Cambridge University Press.*

[24] Incorporated Research Institutions for Seismology (2014). Seismic Analysis Code Users manual, version 101.6a. November 17, 2014. *1200 New York Avenue NW, Suite 400, Washington, DC 20005, 202-682-2220.* `http://ds.iris.edu/files/sac-manual/sac_manual.pdf`, accessed 31.03.2017.

[25] Incorporated Research Institutions for Seismology (2017). GSN Maps. Figure 2: Map of GSN and FDSN backbone stations. *1200 New York Avenue NW, Suite 400, Washington, DC 20005, 202-682-2220.* `https://www.iris.edu/hq/programs/gsn/maps`, accessed 31.03.2017.

[26] International Seismological Centre (2017). About the International Seismological Centre. `http://www.isc.ac.uk/about/`, accessed 24.03.2017.

[27] International Seismological Centre. Bulletin of the International Seismological Centre. `http://www.isc.ac.uk/iscbulletin/`, accessed 24.03.2017.

[28] Incorporated Research Institutions for Seismology (2017). Data Management Center.*1200 New York Avenue NW, Suite 400, Washington, DC 20005, 202-682-2220.* `http://ds.iris.edu/ds/nodes/dmc/`, accessed 30.03.2017.

[29] Jia, Y.-B. (2016). Singular Value Decomposition. Com S 477/577 Notes. 1-9. *Iowa State University.* `http://web.cs.iastate.edu/~cs577/handouts/svd.pdf`, accessed 29.03.2017.

[30] Jones E., Oliphant E., Peterson P., et al. (2001). SciPy: Open Source Scientific Tools for Python. `http://www.scipy.org/`, accessed 11.04.2017.

[31] Kandilarov, A., et al. (2010). Crustal structure of the ultra-slow spreading Knipovich Ridge, North Atlantic, along a presumed ridge segment center. *Springer - Mar Geophys Res. doi:10.1007/s11001-010-9095-8.*

[32] Morgan, J., Nangoo, T., Shah, N., Umpleby, A., and Warner, M. (2013). Full-waveform inversion of cycle-skipped seismic data by frequency down-shifting. *SEG Technical Program Expanded Abstracts 2013: pp. 903-907.doi: 10.1190/segam2013-1067.1.*

[33] Midzi, V., Singh, D.D., Atakan, K., and Havskov, J. (1999). Transitional continentaloceanic structure beneath the Norwegian Sea from inversion of surface wave group velocity data. *Geophysical Journal International 139(2): 433-446.*

[34] Netlib (2017). LAPACK - Linear Algebra PACKage. *Univ. of Tennessee; Univ. of California, Berkeley; Univ. of Colorado Denver; and NAG Ltd.* `http://www.netlib.org/lapack/`, accessed 30.03.2017.

[35] Netlib (2017). BLAS (Basic Linear Algebra Subprograms). `http://www.netlib.org/blas/`, accessed 30.03.2017.

[36] Paige, C. C. and M. A. Saunders (1982). LSQR: An Algorithm for Sparse Linear Equations and Sparse Least Squares. *ACM Transactions on Mathematical Software (TOMS) 8(1): 43-71.*

[37] Pitman III, W. C. and M. Talwani (1972). Sea-floor spreading in the North Atlantic. *Bulletin of the Geological Society of America 83(3): 619-646.*

[38] Rouland, D., et al. (2003). Overlooked earthquakes on and around the Antarctica plate: identification and location of 1999 shallow depth events. *Tectonophysics 376(1): 1-17.*

[39] Seggern, D. (1972). Relative Location of Seismic Events Using Surface Waves. *Geophysical Journal of the Royal Astronomical Society 26(5): 499-513.*

[40] Shearer, P.M. (1999). Introduction to Seismology. *Cambridge University Press*. 40 West 20th Street, New York, NY 10011-4211, USA.

[41] Sørensen, M. B., Ottem¨ller, L., Havskov, J., Atakan, K., Hellevang, B., and R.B. Pedersen (2007). Tectonic processes in the Jan Mayen Fracture Zone based on earthquake occurrence and bathymetry. *Bulletin of the Seismological Society of America 97(3): 772-779.*

[42] Stein, S. and Wysession, M. (2003). An Introduction to Seismology, Earthquakes and Earth Structure. *Blackwell Publishing*. 350 Main Street, Malden, MA 02148-5020, USA.

[43] Waldhauser, F. and Ellsworth, W.L. (2000). A Double-Difference Earthquake Location Algorithm: Method and Application to the Northern Hayward Fault, California. *Bulletin of the Seismological Society of America, 90, 6, pp. 1353-1368, December 2000.*

[44] Weidner, D. J. (1974). Rayleigh Wave Phase Velocities in the Atlantic Ocean. *Geophysical Journal of the Royal Astronomical Society 36(1): 105-139.*

[45] Wessel, P., Smith, Walter.H.F., Scharroo, R., Joaquim, L., and F. Wobbe (2013). Generic Mapping Tools: Improved Version Released. *Eos, Transactions American Geophysical Union 94(45): 409-410.*

[46] Wolfe, C. J. (2002). On the mathematics of using difference operators to relocate earthquakes.*Bulletin of the Seismological Society of America 92(8): 2879-2892.*

[47] Yeo, I. A., et al. (2016). Segment-scale volcanic episodicity: Evidence from the North Kolbeinsey Ridge, Atlantic. *Earth and Planetary Science Letters 439: 81-87.*

[48] Yilmaz, Ö. and S. M. Doherty (2001). Seismic data analysis : processing, inversion, and interpretation of seismic data : Vol. 1. *Tulsa, Okla, Society of Exploration Geophysicists.*

Appendices

Appendix A

Table of events for Jan Mayen Island region

Latitude	Longitude	Date	Depth	Magnitude	Description	Catalog
71.6938 N	12.1478 W	2005-11-07 01:49:34 UTC	10.0 km	MW5.0	Jan Mayen Island Region	ISC
71.6948 N	11.6894 W	2008-11-07 21:40:57 UTC	10.0 km	MW5.1	Jan Mayen Island Region	ISC
71.4464 N	11.0341 W	2012-08-30 13:43:25 UTC	11.1 km	MW6.7	Jan Mayen Island Region	ISC
71.3389 N	9.7571 W	2012-07-15 13:02:43 UTC	11.1 km	MW5.0	Jan Mayen Island Region	ISC
71.3176 N	9.3023 W	2007-12-06 10:52:33 UTC	10.0 km	MW5.4	Jan Mayen Island Region	ISC
71.2543 N	8.9998 W	2014-03-04 02:59:35 UTC	10.0 km	MW5.0	Jan Mayen Island Region	ISC
71.238 N	8.685 W	2000-05-24 01:10:50 UTC	10.0 km	Mw5.3	Jan Mayen Island Region	ISC
71.191 N	8.222 W	2000-05-21 19:58:47 UTC	10.0 km	Mw6.0	Jan Mayen Island Region	ISC
71.0105 N	7.85 W	2009-09-21 08:30:14 UTC	15.9 km	MW5.6	Jan Mayen Island Region	ISC
71.0461 N	7.7397 W	2004-04-14 23:07:37 UTC	10.5 km	MW5.9	Jan Mayen Island Region	ISC
71.0821 N	7.6434 W	2003-06-19 12:59:23 UTC	0.5 km	MW5.5	Jan Mayen Island Region	ISC
71.0982 N	7.5679 W	2005-07-25 16:02:06 UTC	15.3 km	MW5.5	Jan Mayen Island Region	ISC
70.9823 N	7.7137 W	2015-06-30 07:40:01 UTC	10.0 km	mwb5.3	Jan Mayen Island Region	NEIC PDE
71.0184 N	7.5587 W	2016-09-03 06:55:37 UTC	10.0 km	mb5.0	Jan Mayen Island Region	NEIC PDE
70.8684 N	6.9088 W	2011-01-29 06:55:26 UTC	6.4 km	MW6.2	Jan Mayen Island Region	ISC
70.8982 N	6.6703 W	2010-02-22 16:55:02 UTC	13.4 km	MW5.3	Jan Mayen Island Region	ISC
70.7541 N	6.3766 W	2011-10-25 02:32:17 UTC	6.0 km	MW5.1	Jan Mayen Island Region	ISC
70.6905 N	8.4779 W	2012-08-30 13:51:05 UTC	16.4 km	mb5.2	Jan Mayen Island Region	ISC
71.117 N	12.881 W	2001-08-01 09:20:08 UTC	10.0 km	mb5.0	Jan Mayen Island Region	ISC
71.4959 N	4.4708 W	1998-03-23 20:19:27 UTC	10.0 km	mb5.2	Jan Mayen Island Region	ISC
71.4643 N	4.5261 W	1998-03-23 19:30:13 UTC	10.0 km	mb5.3	Jan Mayen Island Region	ISC
71.433 N	3.9503 W	2008-09-29 19:20:22 UTC	10.0 km	mb5.0	Jan Mayen Island Region	ISC
71.3904 N	3.9965 W	2006-08-13 19:03:08 UTC	13.1 km	MW5.0	Jan Mayen Island Region	ISC

Continued on next page

Latitude	Longitude	Date	Depth	Magnitude	Description	Catalog
71.2615 N	4.0776 W	2008-09-28 22:20:21 UTC	10.0 km	MW5.5	Jan Mayen Island Region	ISC
71.4961 N	12.6052 W	2008-05-06 19:51:11 UTC	10.0 km	MW5.0	Jan Mayen Island Region	ISC
70.819 N	13.363 W	2000-07-17 08:18:48 UTC	10.0 km	Mw5.1	Jan Mayen Island Region	ISC
70.766 N	13.603 W	2000-06-21 14:56:25 UTC	10.0 km	Mw5.2	Jan Mayen Island Region	ISC
70.6663 N	14.3308 W	2010-06-03 04:32:42 UTC	12.4 km	MW5.6	Jan Mayen Island Region	ISC
70.6447 N	14.4793 W	2010-06-03 10:16:14 UTC	9.7 km	MW5.0	Jan Mayen Island Region	ISC
70.428 N	15.029 W	1999-07-01 02:06:58 UTC	10.0 km	Mw5.5	Jan Mayen Island Region	ISC
70.395 N	15.115 W	1999-07-01 03:20:42 UTC	10.0 km	Mw5.2	Jan Mayen Island Region	ISC
70.3529 N	15.3805 W	2010-06-09 16:54:23 UTC	13.4 km	MW5.0	Jan Mayen Island Region	ISC
70.3176 N	15.3517 W	2014-06-16 14:24:31 UTC	10.0 km	mww5.4	Jan Mayen Island Region	NEIC PDE
70.295 N	15.308 W	1999-07-01 02:08:02 UTC	10.0 km	Mw5.7	Jan Mayen Island Region	ISC
70.1469 N	15.4772 W	2008-01-15 06:35:14 UTC	10.0 km	MW5.0	Jan Mayen Island Region	ISC
70.1175 N	15.5761 W	2008-01-15 06:55:27 UTC	10.0 km	MW5.0	Jan Mayen Island Region	ISC
69.9863 N	15.7066 W	2013-07-15 11:34:26 UTC	10.0 km	MW5.2	Jan Mayen Island Region	ISC
68.8897 N	16.8681 W	2005-07-06 08:24:40 UTC	10.0 km	MW5.5	Iceland Region	ISC
68.7786 N	17.4002 W	2005-11-12 17:01:35 UTC	10.0 km	MW5.1	Iceland Region	ISC

Table A.1: A small collection of shallow earthquakes along the Kolbeinsey Ridge and JMFZ between 1998 to 2016.

Appendix B

Table of events for Mohns Ridge

Latitude	Longitude	Date	Depth	Magnitude	Description	Catalog
71.8011 N	1.5598 W	1995-07-15 10:54:18 UTC	10.0 km	mb5.4	Jan Mayen Island Region	ISC
71.756 N	1.7389 W	1995-09-20 06:53:43 UTC	10.0 km	mb4.8	Jan Mayen Island Region	ISC
72.619 N	3.5254 E	1995-12-08 07:41:12 UTC	10.0 km	mb5.2	Norwegian Sea	ISC
73.3874 N	7.9241 E	1997-10-06 21:13:10 UTC	10.0 km	mb5.0	Greenland Sea	ISC
71.65 N	3.0258 W	1997-12-02 00:02:03 UTC	10.0 km	mb5.2	Jan Mayen Island Region	ISC
73.1848 N	6.256 E	1998-01-17 23:52:59 UTC	10.0 km	mb4.8	Greenland Sea	ISC
73.2578 N	6.8716 E	1998-01-18 02:53:32 UTC	10.0 km	mb4.8	Greenland Sea	ISC
71.4643 N	4.5261 W	1998-03-23 19:30:13 UTC	10.0 km	mb5.3	Jan Mayen Island Region	ISC
71.4959 N	4.4708 W	1998-03-23 20:19:27 UTC	10.0 km	mb5.2	Jan Mayen Island Region	ISC
73.197 N	6.945 E	1999-04-13 02:09:22 UTC	10.0 km	Mw5.1	Greenland Sea	ISC
73.074 N	5.541 E	1999-06-07 16:35:46 UTC	10.0 km	Mw5.5	Greenland Sea	ISC
73.022 N	5.351 E	1999-06-07 16:10:33 UTC	10.0 km	Mw5.5	Greenland Sea	ISC
72.286 N	0.541 E	1999-08-03 13:55:41 UTC	10.0 km	Mw5.4	Norwegian Sea	ISC
71.697 N	2.431 W	1999-08-26 05:03:05 UTC	10.0 km	Mw5.2	Jan Mayen Island Region	ISC
75.249 N	10.249 E	2000-02-03 15:53:13 UTC	10.0 km	Mw5.5	Svalbard Region	ISC
72.712 N	5.005 E	2000-02-15 18:37:20 UTC	10.0 km	mb4.9	Norwegian Sea	ISC
72.579 N	3.697 E	2000-09-02 06:58:13 UTC	10.0 km	mb4.8	Norwegian Sea	ISC
72.396 N	2.496 E	2001-11-08 02:00:05 UTC	10.0 km	mb4.9	Norwegian Sea	ISC
74.911 N	8.574 E	2001-11-16 16:19:36 UTC	10.0 km	MW5.1	Greenland Sea	ISC
75.285 N	8.039 E	2002-02-09 21:48:04 UTC	10.0 km	mb4.8	Greenland Sea	ISC
73.67 N	8.632 E	2002-04-08 03:55:37 UTC	10.0 km	mb4.8	Greenland Sea	ISC
73.123 N	5.261 E	2002-07-10 14:13:11 UTC	10.0 km	mb4.9	Greenland Sea	ISC
71.564 N	2.8323 W	2002-10-12 03:46:47 UTC	10.0 km	mb4.8	Jan Mayen Island Region	ISC
74.7032 N	8.8016 E	2003-01-09 19:29:23 UTC	10.0 km	mb4.8	Greenland Sea	ISC
73.244 N	6.4511 E	2003-08-30 01:04:42 UTC	10.0 km	MW5.4	Greenland Sea	ISC

Continued on next page

Latitude	Longitude	Date	Depth	Magnitude	Description	Catalog
71.9131 N	1.0884 W	2005-08-30 20:53:48 UTC	10.0 km	MW5.1	Jan Mayen Island Region	ISC
71.4892 N	3.7252 W	2006-01-29 19:49:46 UTC	10.0 km	mb4.8	Jan Mayen Island Region	ISC
73.984 N	9.1493 E	2006-06-30 02:43:34 UTC	10.0 km	MW5.1	Greenland Sea	ISC
72.1789 N	0.8361 E	2006-07-30 07:16:56 UTC	10.0 km	MW5.3	Norwegian Sea	ISC
71.3904 N	3.9965 W	2006-08-13 19:03:08 UTC	13.1 km	MW5.0	Jan Mayen Island Region	ISC
72.2268 N	1.2469 E	2006-11-02 22:52:39 UTC	10.0 km	MW4.9	Norwegian Sea	ISC
72.1609 N	1.0954 E	2006-11-02 22:48:10 UTC	10.0 km	MW5.0	Norwegian Sea	ISC
73.1832 N	6.7727 E	2007-02-25 21:53:13 UTC	10.0 km	MW5.4	Greenland Sea	ISC
73.2828 N	7.9484 E	2007-02-25 20:13:43 UTC	10.0 km	MW5.1	Greenland Sea	ISC
73.2517 N	7.4974 E	2007-02-25 09:13:53 UTC	3.8 km	MW4.9	Greenland Sea	ISC
74.2462 N	8.6572 E	2007-03-10 17:03:06 UTC	10.0 km	mb4.8	Greenland Sea	ISC
74.2515 N	8.7331 E	2007-03-10 17:03:38 UTC	10.0 km	MW5.7	Greenland Sea	ISC
72.1935 N	2.1578 E	2007-03-20 17:03:40 UTC	10.0 km	MW4.9	Norwegian Sea	ISC
73.5631 N	8.3895 E	2007-12-01 13:11:22 UTC	0.0 km	MW4.8	Greenland Sea	ISC
71.2615 N	4.0776 W	2008-09-28 22:20:21 UTC	10.0 km	MW5.5	Jan Mayen Island Region	ISC
71.433 N	3.9503 W	2008-09-29 19:20:22 UTC	10.0 km	mb5.0	Jan Mayen Island Region	ISC
72.2089 N	0.9513 E	2009-08-20 06:35:05 UTC	9.5 km	MW6.0	Norwegian Sea	ISC
73.8033 N	8.5143 E	2010-04-06 23:50:23 UTC	17.0 km	mb5.3	Greenland Sea	ISC
73.4399 N	7.2253 E	2010-05-16 16:39:33 UTC	12.1 km	MW5.1	Greenland Sea	ISC
71.9329 N	1.5276 W	2010-08-16 19:03:42 UTC	14.6 km	MW5.0	Jan Mayen Island Region	ISC
72.0805 N	1.1476 E	2010-11-18 08:08:42 UTC	10.0 km	MW4.8	Norwegian Sea	ISC
72.6292 N	3.6627 E	2011-08-24 08:08:15 UTC	8.9 km	MW5.4	Norwegian Sea	ISC
71.5877 N	2.4203 W	2012-02-17 16:52:23 UTC	10.0 km	MW5.0	Jan Mayen Island Region	ISC
73.0279 N	5.5053 E	2012-05-24 22:47:46 UTC	8.2 km	MW6.3	Greenland Sea	ISC
73.0003 N	5.5736 E	2012-05-25 04:01:35 UTC	7.6 km	MW5.2	Greenland Sea	ISC
72.9542 N	5.4524 E	2012-05-25 00:25:55 UTC	12.2 km	mb5.0	Norwegian Sea	ISC
73.3582 N	8.0178 E	2012-09-11 10:15:56 UTC	11.0 km	MW4.8	Greenland Sea	ISC
71.9216 N	0.2254 W	2012-11-01 06:33:37 UTC	14.2 km	MW4.8	Jan Mayen Island Region	ISC
74.829 N	8.5415 E	2013-06-03 16:48:29 UTC	10.0 km	MW4.8	Greenland Sea	ISC
73.7515 N	8.6717 E	2014-01-16 08:14:47 UTC	14.6 km	MW5.0	Greenland Sea	ISC

Continued on next page

Latitude	Longitude	Date	Depth	Magnitude	Description	Catalog
73.5211 N	8.1028 E	2014-04-26 03:55:33 UTC	10.0 km	mb5.1	Greenland Sea	NEIC PDE
71.7097 N	1.6632 W	2014-11-04 12:33:49 UTC	10.0 km	mb4.8	Jan Mayen Island Region	NEIC PDE
73.2241 N	6.4608 E	2015-01-19 12:45:12 UTC	10.0 km	mww5.4	Greenland Sea	NEIC PDE
73.2056 N	6.368 E	2015-01-19 12:31:51 UTC	10.0 km	mb5.0	Greenland Sea	NEIC PDE
73.2507 N	6.4866 E	2015-01-22 00:39:16 UTC	10.0 km	mb5.1	Greenland Sea	NEIC PDE
74.5705 N	8.4145 E	2015-06-09 19:23:55 UTC	7.33 km	mb5.0	Greenland Sea	NEIC PDE
72.8284 N	4.6453 E	2017-03-10 16:41:12 UTC	10.0 km	mb5.0	Norwegian Sea	NEIC PDE

Table B.1: Event information from 62 earthquakes around Mohns Ridge between 1995 and 2017.

Appendix C

Table of events for Knipovich Ridge and Spitsbergen Fracture Zone

Latitude	Longitude	Date	Depth	Magnitude	Description	Catalog
74.2207 N	8.7535 E	1990-05-27 21:49:35 UTC	29.1 km	mb5.5	Greenland Sea	ISC
74.6444 N	8.71 E	1990-11-11 07:06:29 UTC	10.0 km	mb4.9	Greenland Sea	ISC
77.7413 N	7.9659 E	1991-03-18 14:26:02 UTC	10.0 km	mb4.8	Svalbard Region	ISC
77.6459 N	5.3883 E	1992-05-07 08:24:27 UTC	10.0 km	mb5.0	Svalbard Region	ISC
78.6289 N	5.4946 E	1992-07-20 07:46:47 UTC	10.0 km	mw6.6	Svalbard Region	ISC
76.1953 N	7.2566 E	1992-09-09 13:08:54 UTC	24.0 km	mb5.7	Svalbard Region	ISC
76.2468 N	7.7292 E	1992-09-10 14:54:38 UTC	27.8 km	mb5.3	Svalbard Region	ISC
78.4994 N	6.9775 E	1993-09-23 20:04:01 UTC	10.0 km	mb4.9	Svalbard Region	ISC
78.2927 N	2.206 E	1995-03-09 07:04:22 UTC	10.0 km	mb5.1	Greenland Sea	ISC
76.8258 N	7.7482 E	1995-05-13 22:38:47 UTC	10.0 km	mb4.8	Svalbard Region	ISC
77.1413 N	8.7305 E	1995-06-05 04:40:21 UTC	33.0 km	mb5.2	Svalbard Region	ISC
75.978 N	6.9999 E	1995-10-04 09:17:30 UTC	10.0 km	mb5.1	Greenland Sea	ISC
77.8722 N	7.6345 E	1996-08-20 00:11:00 UTC	10.0 km	mw5.1	Svalbard Region	ISC
77.7866 N	9.1059 E	1997-02-06 14:41:51 UTC	10.0 km	mb5.3	Svalbard Region	ISC
75.249 N	10.249 E	2000-02-03 15:53:13 UTC	10.0 km	Mw5.5	Svalbard Region	ISC
76.341 N	7.612 E	2001-02-04 06:55:53 UTC	10.0 km	mb4.8	Svalbard Region	ISC
74.911 N	8.574 E	2001-11-16 16:19:36 UTC	10.0 km	MW5.1	Greenland Sea	ISC
75.285 N	8.039 E	2002-02-09 21:48:04 UTC	10.0 km	mb4.8	Greenland Sea	ISC
78.391 N	8.005 E	2002-05-27 06:58:48 UTC	12.0 km	mb4.8	Svalbard Region	ISC
74.7032 N	8.8016 E	2003-01-09 19:29:23 UTC	10.0 km	mb4.8	Greenland Sea	ISC
78.4769 N	7.1849 E	2004-07-21 11:25:42 UTC	10.0 km	mb4.8	Svalbard Region	ISC
76.1734 N	7.5683 E	2004-11-27 06:38:27 UTC	10.0 km	MW5.1	Svalbard Region	ISC
78.621 N	6.2164 E	2005-04-02 12:52:34 UTC	10.0 km	MW6.2	Svalbard Region	ISC

Continued on next page

Latitude	Longitude	Date	Depth	Magnitude	Description	Catalog
76.1682 N	5.7614 E	2006-01-11 15:13:42 UTC	10.0 km	MW4.8	Svalbard Region	ISC
78.3009 N	8.324 E	2006-08-09 22:31:13 UTC	10.0 km	MW5.1	Svalbard Region	ISC
76.3627 N	7.0735 E	2009-06-21 12:27:06 UTC	13.0 km	MW5.4	Svalbard Region	ISC
76.3002 N	6.8595 E	2009-06-22 19:05:17 UTC	15.2 km	MW5.1	Svalbard Region	ISC
76.3311 N	6.8091 E	2009-06-22 18:15:40 UTC	13.1 km	MW5.4	Svalbard Region	ISC
76.41 N	6.4005 E	2009-09-19 20:21:55 UTC	3.2 km	MW4.9	Svalbard Region	ISC
76.4559 N	7.6725 E	2010-07-30 09:58:36 UTC	9.9 km	MW5.0	Svalbard Region	ISC
76.4418 N	7.7804 E	2010-10-02 21:26:02 UTC	16.2 km	mb4.9	Svalbard Region	ISC
75.6874 N	8.0968 E	2011-10-05 04:13:35 UTC	10.0 km	MW4.9	Greenland Sea	ISC
76.917 N	7.2679 E	2012-02-07 23:37:05 UTC	12.2 km	MW5.1	Svalbard Region	ISC
78.4683 N	6.9988 E	2012-09-02 12:44:03 UTC	8.5 km	MW5.4	Svalbard Region	ISC
76.0656 N	7.7765 E	2012-10-06 01:19:34 UTC	9.6 km	MW4.9	Svalbard Region	ISC
74.829 N	8.5415 E	2013-06-03 16:48:29 UTC	10.0 km	MW4.8	Greenland Sea	ISC
76.4688 N	7.0662 E	2013-10-28 14:54:28 UTC	6.5 km	MW5.3	Svalbard Region	ISC
75.9596 N	7.0942 E	2013-12-17 13:49:35 UTC	5.1 km	MW5.3	Greenland Sea	ISC
75.924 N	7.5276 E	2013-12-18 08:22:39 UTC	10.0 km	MW5.3	Greenland Sea	ISC
75.8825 N	7.3009 E	2013-12-23 00:28:58 UTC	9.0 km	MW4.8	Greenland Sea	ISC
77.326 N	7.9156 E	2015-01-11 20:34:32 UTC	10.0 km	mb5.4	Svalbard Region	NEIC PDE
80.1209 N	0.7949 E	1991-06-09 10:57:06 UTC	10.0 km	mb4.9	North Of Svalbard	ISC
78.9617 N	3.4538 E	1991-09-01 06:51:04 UTC	10.0 km	mb5.2	Greenland Sea	ISC
78.6289 N	5.4946 E	1992-07-20 07:46:47 UTC	10.0 km	mw6.6	Svalbard Region	ISC
80.2077 N	1.0475 W	1992-08-11 04:03:45 UTC	17.7 km	mb5.1	North Of Svalbard	ISC
81.547 N	3.3789 W	1993-04-24 10:38:30 UTC	10.0 km	mb4.9	North Of Svalbard	ISC
79.4992 N	4.0538 E	1994-01-26 12:07:14 UTC	10.0 km	mb5.1	Greenland Sea	ISC
81.097 N	4.8697 W	1994-11-10 08:45:57 UTC	10.0 km	mb5.3	North Of Svalbard	ISC
80.2989 N	2.8522 W	1995-08-03 01:16:40 UTC	10.0 km	mb4.9	North Of Svalbard	ISC
80.5716 N	2.578 W	1996-05-11 04:38:37 UTC	10.0 km	mw5.6	North Of Svalbard	ISC
80.1089 N	2.5307 E	1998-03-21 16:33:12 UTC	10.0 km	mw6.1	North Of Svalbard	ISC
80.0 N	0.557 E	2000-02-12 09:05:07 UTC	10.0 km	Mw5.1	North Of Svalbard	ISC
79.499 N	4.209 E	2001-07-16 14:09:29 UTC	10.0 km	MW5.2	Greenland Sea	ISC

Continued on next page

Latitude	Longitude	Date	Depth	Magnitude	Description	Catalog
79.848 N	2.739 E	2001-08-26 18:28:23 UTC	10.0 km	MW5.4	Greenland Sea	ISC
80.839 N	0.786 E	2001-12-08 06:44:22 UTC	10.0 km	MW5.3	North Of Svalbard	ISC
81.6331 N	3.5842 W	2003-02-13 02:21:08 UTC	10.0 km	MW5.1	North Of Svalbard	ISC
80.3238 N	1.6877 W	2003-09-22 20:45:15 UTC	3.5 km	MW5.2	North Of Svalbard	ISC
79.1084 N	2.1762 E	2003-10-07 02:36:54 UTC	10.0 km	MW5.0	Greenland Sea	ISC
81.538 N	3.6769 W	2004-12-15 06:47:03 UTC	10.0 km	MW4.9	North Of Svalbard	ISC
81.7125 N	4.6104 W	2005-06-16 10:17:59 UTC	10.0 km	MW5.0	North Of Svalbard	ISC
79.5515 N	4.3074 E	2005-08-13 23:23:19 UTC	10.0 km	MW5.0	Greenland Sea	ISC
82.7551 N	6.132 W	2006-06-21 01:33:25 UTC	10.0 km	MW4.8	North Of Svalbard	ISC
79.624 N	3.6624 E	2006-07-04 18:48:22 UTC	10.0 km	MW4.8	Greenland Sea	ISC
81.969 N	5.1867 W	2008-01-10 22:50:40 UTC	10.0 km	MW5.1	North Of Svalbard	ISC
79.5538 N	2.849 E	2008-06-01 06:24:38 UTC	10.0 km	MW4.8	Greenland Sea	ISC
80.8532 N	2.5942 W	2009-01-01 02:54:06 UTC	16.8 km	mb4.8	North Of Svalbard	ISC
80.1869 N	0.9221 W	2009-03-05 12:17:26 UTC	14.4 km	MW5.4	North Of Svalbard	ISC
80.2067 N	1.4032 W	2009-03-05 19:41:41 UTC	14.4 km	MW5.5	North Of Svalbard	ISC
80.3143 N	1.9637 W	2009-03-06 10:50:30 UTC	14.2 km	MW6.5	North Of Svalbard	ISC
82.5186 N	8.7914 W	2009-05-17 19:24:21 UTC	16.0 km	MW5.5	North Of Svalbard	ISC
82.2287 N	6.2379 W	2011-11-26 23:59:52 UTC	12.3 km	MW5.1	North Of Svalbard	ISC
79.8963 N	0.9097 E	2012-03-30 11:19:19 UTC	9.6 km	MW5.1	Greenland Sea	ISC
79.5184 N	3.1976 E	2012-07-23 04:38:42 UTC	4.3 km	MW4.8	Greenland Sea	ISC
79.4768 N	3.8101 E	2012-07-28 10:14:44 UTC	5.9 km	MW4.8	Greenland Sea	ISC
81.2787 N	4.1343 W	2012-07-28 11:23:43 UTC	10.8 km	MW5.0	North Of Svalbard	ISC
80.7343 N	3.3747 W	2012-10-29 14:54:53 UTC	10.0 km	mb4.9	North Of Svalbard	ISC
79.9203 N	0.0374 W	2014-02-20 13:26:20 UTC	14.2 km	MW5.0	Greenland Sea	ISC
80.6283 N	2.5068 W	2014-10-08 10:29:58 UTC	10.0 km	mb4.9	North Of Svalbard	NEIC PDE

Table C.1: Event information from 77 earthquakes around Knipovich Ridge and SFZ between 1990 and 2015.

Appendix D

Station list for earthquake 2009-08-20 06:35:05 UTC

Station	Latitude	Longitude	Distance	Azimuth	Elevation	Name
FURI	8.90°	38.68°	67.29°	139.05°	2570 m	Mt. Furi, Ethiopia
BBGH	13.14°	-59.56°	68.72°	-114.54°	180 m	Gun Hill, Barbados
SACV	14.97°	-23.61°	59.04°	-152.08°	387 m	Santiago Island, Cape Verde
ANWB	17.67°	-61.79°	65.02°	-110.87°	39 m	Willy Bob, Antigua and Barbuda
SJG	18.11°	-66.15°	65.86°	-106.37°	420 m	San Juan, Puerto Rico
MTDJ	18.23°	-77.53°	69.16°	-95.22°	925 m	Mount Denham, Jamaica
SDDR	18.98°	-71.29°	66.56°	-101.01°	589 m	Presa de Sabenta, Dominican Republic
GTBY	19.93°	-75.11°	66.81°	-96.97°	79 m	Guantanamo Bay, Cuba
GRTK	21.51°	-71.13°	64.11°	-100.27°	12 m	Grand Turk, Turks and Caicos Islands
RAYN	23.52°	45.50°	54.57°	127.87°	631 m	Ar Rayn, Saudi Arabia
UOSS	24.95°	56.20°	55.98°	115.99°	284.4 m	Univ. of Sharjah, Sharjah, United Arab Emirates
KMI	25.12°	102.74°	69.65°	70.96°	1975 m	Kunming, Yunnan Province, China
DWPF	28.11°	-81.43°	61.03°	-87.86°	30 m	Disney Wilderness Preserve, Floria, USA
MACI	28.25°	-16.51°	44.97°	-158.04°	1674	Morro de la Arena, Canary Islands
TX32	29.33°	-103.67°	66.47°	-66.94°	1013	TXAR Array, Lajitas, TX, USA
TX31	29.33°	-103.67°	66.47°	-66.94°	1025 m	TXAR Array, Lajitas, TX, USA
LSA	29.70°	91.13°	61.90°	79.95°	3660 m	Tibet, China
HKT	29.96°	-95.84°	63.63°	-73.79°	-413	Hockley, Texas
ENH	30.28°	109.49°	66.66°	63.09°	500 m	Enshi, Hubei Province, China
SSE	31.09°	121.19°	68.90°	52.46°	40 m	Shanghai, China
TUC	32.31°	-110.78°	65.59°	-59.56°	910 m	Tucson, Arizona
BBSR	32.37°	-64.70°	51.96°	-102.32°	30 m	Bermuda Institute of Ocean Sciences, St. George's Bermuda
PFO	33.61°	-116.46°	65.80°	-54.15°	1280 m	Pinon Flat, California, USA
NI	33.65°	73.27°	52.78°	95.15°	629 m	Nilore, Pakistan
XAN	34.03°	108.92°	62.95°	62.26°	630 m	Xi'an, China
PASC	34.17°	-118.19°	65.69°	-52.47°	341 m	Art Center College of Design (GSN-affiliate)
KBL	34.54°	69.04°	50.67°	98.88°	1920	Kabul, Afghanistan
ANMO	34.95°	-106.46°	61.93°	-62.42°	1820 m	Albuquerque, New Mexico, USA
WVT	36.13°	-87.83°	55.48°	-78.53°	170 m	Waverly, Tennessee, USA
MAJO	36.55°	138.20°	67.25°	36.25°	405 m	Matsushiro, Japan
INCN	37.48°	126.62°	64.03°	45.82°	80 m	Inchon, Republic of Korea
CMLA	37.76°	-25.52°	36.93°	-144.09°	429 m	Cha de Macela, Sao Miguel Island, Azores
ABKT	37.93°	58.12°	44.28°	108.31°	678 m	Alibek, Turkmenistan
CMB	38.03°	-120.39°	62.52°	-49.32°	697 m	Columbia College, Columbia, CA, USA
CCM	38.06°	-91.24°	54.71°	-74.58°	222 m	Cathedral Cave, Missouri, USA

Continued on next page

Station	Latitude	Longitude	Distance	Azimuth	Elevation	Name
WCI	38.23°	-86.29°	53.08°	-78.96°	210 m	Wyandotte Cave, Indiana, USA
NV31	38.43°	-118.16°	61.61°	-51.07°	1509 m	NVAR Array Site 31, Mina, NV, USA
PAB	39.54°	-4.35°	32.77°	-172.44°	950 m	San Pablo, Spain
ANTO	39.87°	32.79°	35.94°	136.38°	1090 m	Ankara, Turkey
BJT	40.02°	116.17°	59.16°	53.80°	197 m	Baijiatuan, Beijing, China
GNI	40.15°	44.74°	38.51°	121.83°	1609 m	Garni, Armenia
SSPA	40.64°	-77.89°	48.32°	-85.46°	270 m	Standing Stone, Pennsylvania
ERM	42.02°	143.16°	62.75°	30.81°	40 m	Erimo, Hokkaido Island, Japan
HRV	42.51°	-71.56°	44.68°	-90.37°	200 m	Adam Dziewonski Observatory (Oak Ridge), Massachusetts, USA
AAK	42.64°	74.49°	44.88°	89.31°	1633.1 m	Ala Archa, Kyrgyzstan
PD31	42.77°	-109.56°	55.39°	-56.66°	2219 m	PDAR Array, Pinedale, WY, USA
WMQ	43.81°	87.70°	47.80°	76.53°	850 m	Urumqi, Xinjiang Province, China
KIV	43.96°	42.69°	34.41°	122.00°	1054 m	Kislovodsk, Russia
RSSD	44.12°	-104.04°	52.69°	-60.68°	2090 m	Black Hills, South Dakota, USA
COR	44.59°	-123.30°	56.91°	-44.64°	110 m	Corvallis, Oregon, USA
MDJ	44.62°	129.59°	57.79°	41.08°	270 m	Mudanjiang, Heilongjiang Province, China
YSS	46.96°	142.76°	57.86°	29.89°	150 m	Yuzhno Sakhalinsk, Russia
ULN	47.87°	107.05°	49.51°	57.94°	1610 m	Ulaanbaatar, Mongolia
BFO	48.33°	8.33°	24.12°	167.94°	589 m	Black Forest Observatory, Schiltach, Germany
HIA	49.27°	119.74°	51.28°	47.13°	620 m	Hailar, Neimenggu Autonomous Region, China
GRFO	49.69°	11.22°	22.99°	162.82°	384 m	Grafenberg, Germany
KIEV	50.70°	29.22°	24.87°	134.49°	180 m	Kiev, Ukraine
KURK	50.72°	78.62°	38.89°	80.12°	184 m	Kurchatov, Kazakhstan
TLY	51.68°	103.64°	45.14 °	58.59°	579 m	Talaya, Russia
ADK	51.88°	-176.68°	55.90°	-1.76°	130 m	Adak, Aleutian Islands, Alaska
ATTUB	52.88°	173.16°	54.79 °	5.74°	250 m	Attu Island, AK, USA
PET	53.02°	158.65°	53.80°	16.43°	110 m	Petropavlovsk, Russia
BRVK	53.06°	70.28°	34.33°	85.71°	330 m	Borovoye, Kazakhstan
FFC	54.73°	-101.98°	42.45°	-56.50°	338 m	Flin Flon, Canada
OBN	55.11°	36.57°	22.61°	119.97°	160 m	Obninsk, Russia
ESK	55.32°	-3.21°	16.98°	.171.88°	242 m	Eskdalemuir, Scotland, UK
ARU	56.43°	58.56°	27.89°	93.36°	250 m	Arti, Russia
KDAK	57.78°	-152.58°	48.72°	-18.43°	152 m	Kodiak Island, Alaska, USA
KONO	59.65°	9.60°	13.01°	160.28°	216 m	Kongsberg, Norway
YAK	62.03°	129.68°	41.30°	33.67°	110 m	Yakutsk, Russia
BORG	64.75°	-21.33°	10.95°	-121.61°	110 m	Borgarfjordur, Asbjarnarstadir, Iceland
IL31	64.77°	-146.89°	41.31°	-20.10°	419 m	ILAR Array, Eilson, AK, USA
COLA	64.87°	-147.86°	41.32°	-19.45°	200 m	College Outpost, Alaska, USA
SFJD	67.00°	-50.62°	18.07°	-80.73°	330 m	Sondre Stromfjord, Greenland
LVZ	67.90°	34.65°	12.08°	94.10°	630 m	Lovozero, Russia
BILL	68.07°	166.45°	39.40°	8.47°	320 m	Bilibino, Russia
KEV	69.76°	27.00°	8.76°	93.51°	100 m	Kevo, Finland
TIXI	71.63°	128.8°	32.38°	27.66°	40 m	Tiksi, Russia
KBS	78.92°	11.94°	7.22°	16.96°	90 m	Ny-Alesund, Spitzbergen, Norway
ALE	82.50°	-62.35°	15.86°	-25.25°	60 m	Alert, N.W.T., Canada

Table D.1: The earthquake 2009-08-20 06:35:05 UTC in the Norwegian Sea is observed at 80 stations.

Appendix E

Additional documentation

E.1 Kolbeinsey Ridge and JMFZ

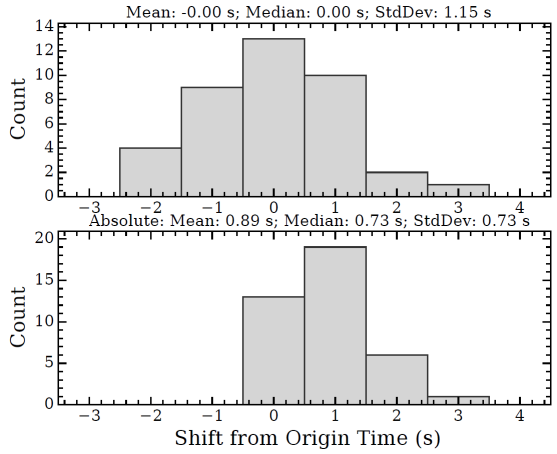

Figure E.1: Distribution of origin time shift between relocated epicentroids and the original epicenter locations, in both overall and absolute calculations.

E.2 Mohns Ridge

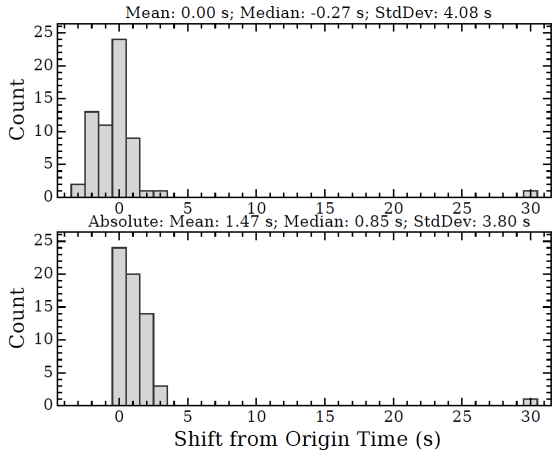

Figure E.2: Distribution of origin time shift between relocated epicentroids and the original epicenter locations, in both overall and absolute calculations.

E.3 Knipovich Ridge and SFZ

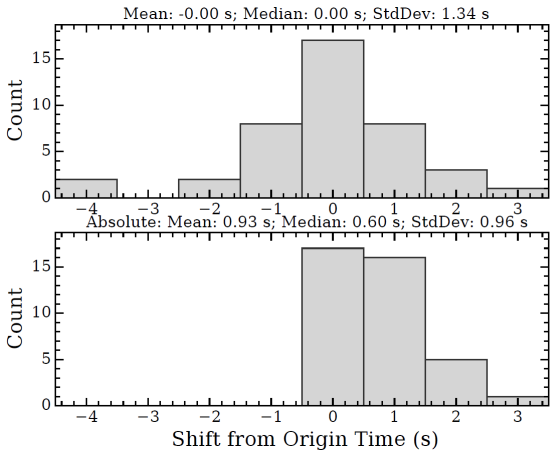

Figure E.3: Distribution of origin time shift between relocated epicentroids and the original epicenter locations at Knipovich Ridge, in both overall and absolute calculations.

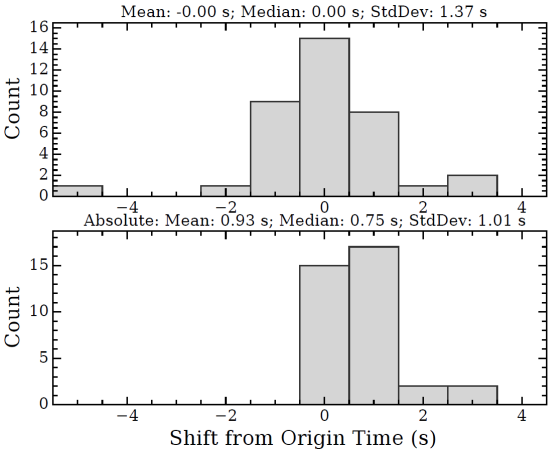

Figure E.4: Distribution of origin time shift between relocated epicentroids and the original epicenter locations at SFZ, in both overall and absolute calculations.